Three dimensional viscoelastic instabilities in a four-roll mill geometry at the Stokes limit.

Paloma Gutierrez-Castillo,* Adam Kagel,† and Becca Thomases‡

Department of Mathematics,

University of California,

Davis, California 95616, USA

(Dated: January 9, 2020)

Abstract

Three-dimensional numerical simulations of viscoelastic fluids in the Stokes limit with a four-roll mill background force (extended to the third dimension) were performed. Both the Oldroyd-B model and FENE-P model of viscoelastic fluids were used. Different temporal behaviors were observed depending on the Weissenberg number (non-dimensional relaxation time), model, and initial conditions. Temporal dynamics evolve on long time scales and simulations were accelerated by using a Graphics Processing Unit (GPU). Previously, parameter explorations and long-time simulations in 3D were prohibitively expensive. For small Weissenberg number, all the solutions are constant in the third dimension, displaying strictly two-dimensional temporal evolutions. However, for sufficiently large Weissenberg number, three-dimensional instabilities were observed, creating complex temporal behaviors. For certain Weissenberg values and model, the instability that first emerges is two-dimensional (in the x, y plane), and then the solution develops an instability in the $z-$direction whereas for others the z instability comes first. Using a linear perturbation from a steady two-dimensional background solution, extended to three dimensions as constant in the third dimension, it is demonstrated that there is a linear instability for sufficiently large Weissenberg number, and possible mechanisms for this instability are discussed.

* pgutierrez@math.ucdavis.edu

† ackagel@ucdavis.edu

‡ thomases@math.ucdavis.edu

Keywords: Viscoelastic Fluid instabilities, Oldroyd-B, FENE-P

I. INTRODUCTION

It is well known that viscoelastic fluids can develop instabilities and time-dependent flows even in the creeping flow regime (very low Reynolds number). It is thought that these instabilities can be used to enhance mixing at micro-scales which is difficult in Newtonian fluids.

While the mixing properties and dynamics of viscoelastic fluids have been studied experimentally, theoretically, and numerically, a complete picture of the purely elastic instabilities in the low Reynolds number regime has not emerged. Numerical simulations in two spatial dimensions are the most well-studied, and there are far fewer numerical studies in three dimensions. Analysis of instabilities of 3D flows at extensional points are nearly absent in the literature.

Note that even in experiments of fluids that exhibit three-dimensional flows it is difficult to measure all three dimensions simultaneously. Only some of the newest techniques have been able to analyze the fully three-dimensional flows [1]. See [2] for a recent review of the state of the art of the three-dimensional viscoelastic instabilities in micro-channels which is one of the main applications where low Reynolds number instabilities are studied.

Numerical studies have shown the importance of varying the height of the third dimension in different kinds of micro-fluidic channels. In [3] the authors perform three-dimensional simulations of viscoelastic fluids in a contraction channel. They showed that varying the aspect ratio of the channel has similar effects to varying other parameters, such as fluid properties, which influence the elasticity number. Specifically, they simulate a three-dimensional flow ($\mathrm{Re} = 0.465$) passing through a planar contraction micro-channel. They observe a transition in the vortex mechanism from a salient-corner to a lip vortex mechanism as the aspect ratio is varied from ideal 2- D flow to strongly 3-D flow.

One of the most significant applications of micro-scale instabilities in non-Newtonian fluids is mixing enhancement. Some recent three-dimensional simulations have been instrumental in understanding this effect. For example, the first three-dimensional DNS (Direct Numerical Simulation) study of a viscoelastic flow in a curvilinear channel driven by a constant pressure gradient was performed by [4] obtaining a good agreement with experimental

data (even though they introduced an artificial dissipation effect). Then, they explore the relationship between the purely elastic instability and the effect of obtaining a mixing enhancement. They have seen how above a critical Weissenberg number, (Wi non-dimensional relaxation time), there exists a strong unstable secondary flow in the cross section perpendicular to the streamwise direction, resulting in a strong mixing enhancement.

Furthermore, evidence of the importance of the third dimension in another application of viscoelastic flows can be found in [5], where simulations for polymer extrudate swell out of slit dies from low to high aspect ratios were performed. It was shown that increasing the aspect ratio of the die geometry (width/height ratio variation from 1 to 20) contributes to a significant change in the 3D extrudate deformation (relative changes of 10% in several directions; absolute changes up to 30%) and delays the equilibrium axial position (up to a factor 10).

Experimentally, even though the devices are three-dimensional, measuring the whole three-dimensional field is not possible, and only some planes are generally accessible. There exists a very recent study, [1], in which they used a three-dimensional holographic particle velocimetry to study the three-dimensional flow field in the case of flow past a cylinder allowing to reproduce the three-dimensional velocity fields. Besides being a benchmark for Non-Newtonian fluids, flow around a cylinder mechanisms are not well understood. With the three-dimensional velocity fields, they have seen more complex flow transitions than could previously be inferred from two-dimensional measurements. They reported three main discoveries of the elastic instability upstream of a single cylinder, including the demonstration of the propagation of an elastic wave, which provides a mechanism by which perturbations can travel upstream. The elastic wave is found to increase in speed and penetrate farther upstream with Wi, indicating an absolute instability emanating from the cylinder. Note that the discoveries of the mechanisms of instabilities in one geometry, such as planar contractions, can help the understanding of the study of the instabilities of the flow around the cylinder and vice-versa. However, there are differences between the flow around a cylinder and contraction type flows since the cylinder separates the flow into two separate streams.

It has been known for a while that there is an influence of the third dimension on instabilities in flows around cylinders. A recent experimental study focuses on the case of flow around high-aspect-ratio, low-blockage-ratio microfluidic cylinders [6]. They studied the configurations of one and two cylinders and how the influence on each other depends on

Wi. Knowing how the instabilities depend on the number of cylinders is especially relevant since a large array of cylinders are often used as a model for porous media. Experimentally, it was shown [7] that a long micro-channel with an array of obstacles shows instabilities in the case of Non-Newtonian fluids. More recently, an array of staggered cylinders, similar to a model for porous media, were studied experimentally, see for example [8]. Numerically, when increasing the number of cylinders in the array, the computational cost increases significantly and thus, most of the numerical studies with a multitude of cylinders are restricted to two dimensions.

Another geometry where there exist pure-elastic instabilities is the three-dimensional cross-slot geometry (and its variants such as the "T" geometry). Low Reynolds number instabilities at extensional points have been observed both experimentally and numerically [9–11] but the role of the third dimension in these instabilities is not well understood. In [12], the authors numerically study the three-dimensional flow behavior for $\mathrm{Re} \leq 0.01$. Later the same group, studied experimentally the difference on having two different aspect ratios in the cross-slot geometry [13].

We have seen that there is significant evidence showing the importance of the third dimension in the viscoelastic creeping flow instabilities. Similar to the cross-slot geometry, i.e. showing pure elastic instabilities at extensional points in two dimensions, is the four-roll mill geometry. This geometry has been shown to present instabilities but also mixing enhancement [14–16] and is a somewhat simple geometry to do some analysis on the flow dynamics [17, 18]. In this configuration, four-rollers create an extensional flow at the center of the domain which will drive elastic instabilities. Here we extend this geometry to a third dimension to understand the effect of the third dimension on instabilities in the flow. In this case, the domain is still periodic but now in three dimensions and the background force is formed by cylinders instead of circles. An examination of this extended geometry was previously discouraged by long-computation times, but our spectral model allows for significant computational speed ups via GPU acceleration of Fast Fourier Transforms (FFTs), described in the Appendix. We focus our study on the creation of an instability in the direction parallel to the cylinders, which is novel with respect to the two-dimensional cases previously studied.

II. FLUID MODELS AND NUMERICAL DETAILS

A. Stokes-Oldroyd-B model

For some of our simulations we use the Oldroyd-B model of a viscoelastic fluid at zero Reynolds number, with explicit polymer stress diffusion, given in dimensionless form by

$$\Delta \mathbf{u} - \nabla p + \beta \nabla \cdot \mathbf{S} = \mathbf{f}, \tag{1}$$

$$\nabla \cdot \mathbf{u} = 0 \tag{2}$$

$$\partial_t \mathbf{S} + \mathbf{u} \cdot \nabla \mathbf{S} - \left(\nabla \mathbf{u} \mathbf{S} + \mathbf{S} \nabla \mathbf{u}^T\right) + \mathrm{Wi}^{-1}(\mathbf{I} - \mathbf{S}) = \nu_p \Delta \mathbf{S}, \tag{3}$$

for $\mathbf{u}$ the fluid velocity, p the fluid pressure, and $\mathbf{S}$, the (symmetric) conformation tensor, a macroscopic average of the polymer orientation and stretching that is related to the polymer stress tensor by $\boldsymbol{\tau}_p = \beta(\mathbf{S} - \mathbf{I})$. The parameters, β, the non-dimensional polymer stiffness, and Wi, the Weissenberg number, or non-dimensional relaxation time, are defined by

$$\beta = \frac{GL}{\mu U}, \quad \mathrm{Wi} = \frac{\lambda U}{L}, \tag{4}$$

for μ the solvent viscosity, λ the fluid relaxation time, G the polymer elastic modulus, $L = 2\pi$ the system size, and U a characteristic velocity scale. Note that the Oldroyd-B model has $\nu_p = 0$ in Eq. (3). The polymer stress diffusion term, $\nu_p \Delta \mathbf{S}$, for $\nu_p = 0.001$, is included in the right-hand side of Eq. (3) as a numerical regularization. We will make some comments on the applicability of these results to the case without diffusion and varying resolution in the end of Sec. V B.

The background force is given by:

$$\mathbf{f} = \begin{pmatrix} 2 \sin x \cos y \\ -2 \cos x \sin y \\ 0 \end{pmatrix}, \tag{5}$$

which in a Newtonian Stokes flow ($\beta = 0$) corresponds to a four-roll velocity field $\mathbf{u} = -\frac{1}{2}\mathbf{f}$. The Stokes solution sets the characteristic (inverse) time scale $U/L = 1$. The quantity $\beta \cdot \mathrm{Wi}$ is the ratio of the polymer viscosity to solvent viscosity, so that given a particular working fluid the ratio is fixed independently of experimental conditions. In our simulations $\beta \cdot \mathrm{Wi} = 0.5$ is fixed. This value is consistent with the fluids used in experiments of dilute polymer solutions with highly viscous solvents, Boger fluids, (see, for example, [9]).

B. FENE-P model

To test the robustness of the instabilities we found in the Oldroyd-B model, we also use the FENE-P model [19] and in this case the advection is performed with the square root method. For the square-root method [20], the model is reformulated in terms of the (unique) positive symmetric square root $\mathbf{b}(x,t)$ of the conformation tensor $\mathbf{S}(x,t)$, and the evolution of $\mathbf{S}$ given by Eq. (3) is replaced with

$$(\frac{\partial}{\partial t} + \mathbf{u}\cdot\nabla)\mathbf{b} = \mathbf{b}\nabla\mathbf{u} + \mathbf{a}\mathbf{b} + \frac{1}{2\mathrm{Wi}}((b^T)^{-1} + \frac{\mathbf{b}}{1-||\mathbf{b}||^2/\ell^2}) + \nu_f\Delta\mathbf{b}. \tag{6}$$

The time evolution produces the unique positive symmetric square root of $\mathbf{S}$ when $\mathbf{a}(x,t)$ is any antisymmetric matrix and $\mathbf{b}^T(x,0)\mathbf{b}(x,0) = \mathbf{S}(x,0)$. The key observation is that by choosing $\mathbf{a}(x,t)$ properly it is possible to tune the evolution Eq (6) (and similarly in other models with an upper convective derivative) to preserve the symmetry of $\mathbf{b}$. Specifically by choosing a symmetric initial data $\mathbf{b}^T(x,0) = \mathbf{b}(x,0)$, the subsequent evolution will preserve the symmetry. We fix the length-scale cut off to be $\ell^2 = 400$. We have also added diffusion to the model, $\nu_f \approx 0.024$. The size of this diffusion coefficient is comparable to the size of the square root of the diffusion coefficient in the Oldroyd-B model.

C. Numerical details

The system Eqs. (1)–(3) (or Eq. (6) for the FENE-P simulations) are solved in a 3D spatially periodic domain, $[0, 2\pi)^3$. Figure 1 shows a schematic of the domain with the background force.

We use a pseudo-spectral method and alternate solving the Stokes equations for a given polymer stress tensor and time-stepping the advection equation for the conformation tensor in Fourier space using a second order Adams-Bashforth-Crank-Nicholson method. This is the same numerical set-up used in [15, 16] where $2D$ solutions were studied and the instabilities in the four-roll mill problem were first observed and more recently in [21] where the $2D$ instabilities were described using proper orthogonal decomposition (POD) for both the Oldroyd-B and FENE-P models. We have used $N^3 = 128^3$ grid points, this gives uniform grid spacing $\Delta x = 2\pi/N \approx 0.05$ and time step $\Delta t = 0.005$. To demonstrate the accuracy of the spacial resolution a refinement study is shown in figure 2. This figure shows the relative

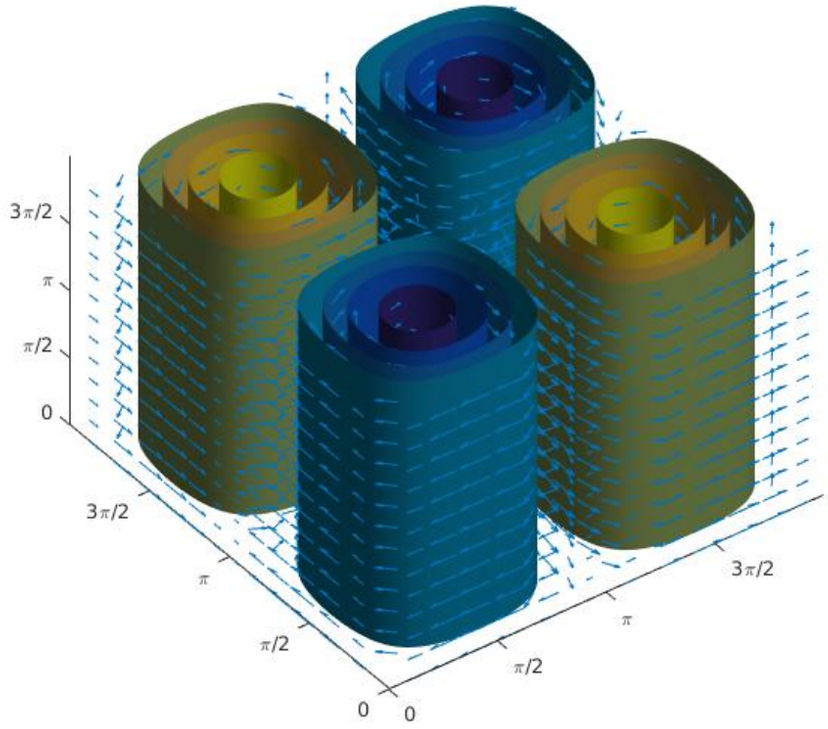

FIG. 1. Schematic of the setup showing the background force. Periodic boundary conditions are assumed in x, y, z.

error in L^2 norm of the velocity and L^2 norm of the conformation tensor, relative to the $N = 192$ solution of a typical case of $\mathrm{Wi} = 12$. We see that the error decays with increasing refinement and the error is on the 10^{-5} for the two finest reported grids. Note also that the time step was chosen sufficiently small to obtain stability in the method but the dynamics of the problem are very slow with periods on the order of $T = 100$ or longer. Therefore there are over $20,000$ time steps in a period.

To compute the solutions for Oldroyd-B we start from a random perturbation of the low Fourier modes from isotropic initial polymer stress $\mathbf{S} = \mathbf{I}$. Specifically, we randomly perturb 25 of the modes with frequencies smaller than 8 in all the directions. Therefore, the polymer stress with the perturbation $\tilde{\mathbf{S}}$ can be written as:

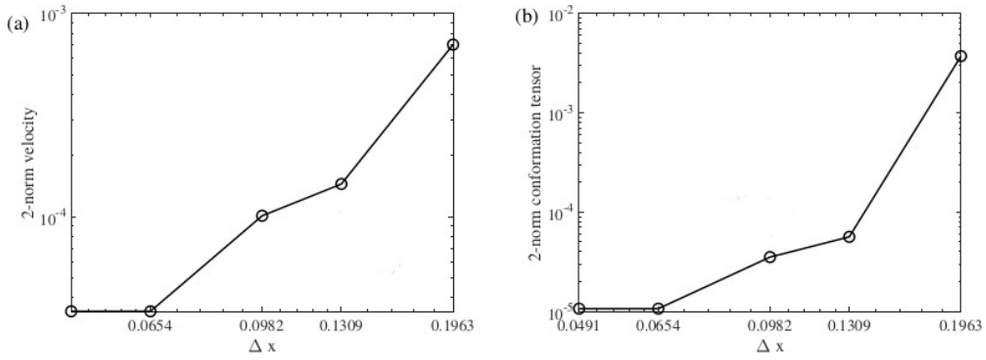

FIG. 2. Grid refinement study. Errors computed by comparing with the finest resolution $N = 192$, (a) L^2 norm of the velocity, (b) L^2 norm of the conformation tensor.

$\mathbf{S} = \mathbf{I} + \tilde{\mathbf{S}}$. where the diagonal terms of the perturbation are computed by

$$\tilde{S}_{ii} = \sum_{k=1}^{25} C_k \sin(\omega_{k_x} x) \sin(\omega_{k_y} y) \sin(\omega_{k_z} z)$$

where x, y, and z are spatial coordinates,ω_{k_x}, ω_{k_y}, and ω_{k_z} are randomly selected from 1 to 8 and C_k is randomly selected in Fourier space to be $0 < C_k < 10^3$ equivalent to a small perturbation in the physical space. Similarly, the off diagonal terms are defined in the same way but with a different constant $0 < \bar{C}_k < 10^2$. That is

$$\tilde{S}_{ij} = \sum_{k=1}^{25} \bar{C}_k \sin(\omega_{k_x} x) \sin(\omega_{k_y} y) \sin(\omega_{k_z} z)$$

Adding all these perturbations lead to a perturbation of order 0.01 of the identity in the physical space.

For FENE-P, we perform these simulations with initial data for the conformation tensor taken from the Oldroyd-B solutions both with and without instability in the z direction (with the intermediate step of computing the symmetric square root to the stress tensor).

The dynamics in this problem occur on very long time-scales and to capture the slow dynamics we run our simulations up to at least $t = 4000$, and in some cases longer. The wide parameter searches and long time evolutions made this exploration prohibitively expensive in the past. Here we use GPU acceleration of Fast Fourier Transforms (FFTs) which in our spectral model allows for significant computational speed ups. The details are described in the Appendix.

III. RESULTS FOR OLDROYD-B

In this section, we report on the results obtained using the Oldroyd-B model when varying $\mathrm{Wi} \leq 12$. In particular, we want to analyze in detail the cases which develop an instability in the $z-$direction. This instability is new with respect to the 2D cases analyzed previously in the literature [15, 16, 21].

Wi range	# Flow transitions	x, y dynamics	$z-$dynamics
$\mathrm{Wi} \leq 5$	0	Steady 2 symmetries	Steady and constant
$\mathrm{Wi} = 6$	1	Steady 1 symmetry	Steady and constant
$\mathrm{Wi} = 7$	2	Quasi-steady 1 symmetry then unstable	Steady and constant
$8 \leq \mathrm{Wi} < 10$	2	Unstable in 2D	Temporal $z-$dependence after 2D instability
$10 \leq \mathrm{Wi} \leq 12$	2	Unstable in 2D	Temporal $z-$dependence before 2D instability

TABLE I. Categorization of flow states found with simulations of the Oldroyd-B model in 3D. Flow is forced with 2D four-roll mill that is constant in z.

A. Cases with no $z-$instability (Wi < 8)

For $\mathrm{Wi} < 8$ there is no instability in the third dimension. Note that since the same 4-roll mill geometry is prescribed in the x, y plane for all z, any flow dependence in the $z-$direction is what we refer to as the fully three dimensional solution. The results for $\mathrm{Wi} < 8$ remain constant in z, which we refer to as purely 2D. These results are similar to the 2D results presented in previous papers [15, 16, 21]. As in the 2D simulations, here it was found that for $\mathrm{Wi} \leq 5$ the flows remains in a steady symmetric state formed by 4-roll cylinders, the arrangement of the flow is similar to that shown in Fig. 3 (a). Again as in the 2D simulations for $\mathrm{Wi} = 6$, the flow becomes unstable in the x, y plane and, in the long term, produces a flow that is steady but asymmetric and remains constant in z. For $7 \leq \mathrm{Wi} < 8$, the flow

is still two dimensional but it has 2D instabilities that persist in time and are temporally quasi- periodic with a dominant vortex changing its position in the x, y plane. A summary of the different flow states observed is given in Table I.

B. Three-dimensional instabilities

1. 2D instability followed by a 3D instability ($8 \leq Wi < 10$)

The first three-dimensional instability was observed for Wi = 8. At early times, the flow remains in a quasi-steady state with a symmetric 4-roll pattern. See Fig. 3(a) for a solution at $t = 500$ before the onset of any time-dependent behavior. The first row shows contours of the azimuthal vorticity at $z = \pi$, where the 4-roll symmetric structure is clear. The second row shows tr$\mathbf{S}$ at the same time, and the typical regions of concentrated stress, large tr$\mathbf{S}$, can be observed. Note here that using horizontal cuts at the center of the domain, it is useful to compare with the 2D simulations. However, this is not sufficient to describe the three-dimensional solution. Therefore, vertical cuts and 3D isosurfaces are presented here to better describe the solution structure. Specifically, the third row of Fig. 3 shows tr$\mathbf{S}$ in a vertical plane, and the last row shows isosurfaces of vorticity. With the vertical cuts and the isosurfaces, at $t = 500$, we see that there is no three-dimensional behavior in the flow (i.e. the solution is constant in z).

At later times, the flow undergoes a 2D instability where it loses the 4-roll symmetric pattern at around $t = 550$ and one of the vortices becomes dominant. See for example Fig. 3(b) for a solution at $t = 675$ where the top-right vortex is dominant. The dominant vortex starts rotating to different positions (similar to the instability found in the 2D simulations of Wi = 7 described in [21]). Then, around $t = 1200$, the flow becomes three-dimensional perturbing the cylindrical isosurfaces. See for example Fig. 3(c) for a solution at $t = 1370$. In this case, this 3D motion is occurring simultaneously with the rotation of the dominant vortex making the flow pattern difficult to describe. See Fig. 3(d) for a solution at $t = 1590$ where the dominant vortex is now in a different quadrant and the vortex tube pinching is at different heights from that in Fig. 3(c). For details of the temporal dependence see the movies (Multimedia view).

An interesting way to visualize the evolution of the z instability is to look at the time

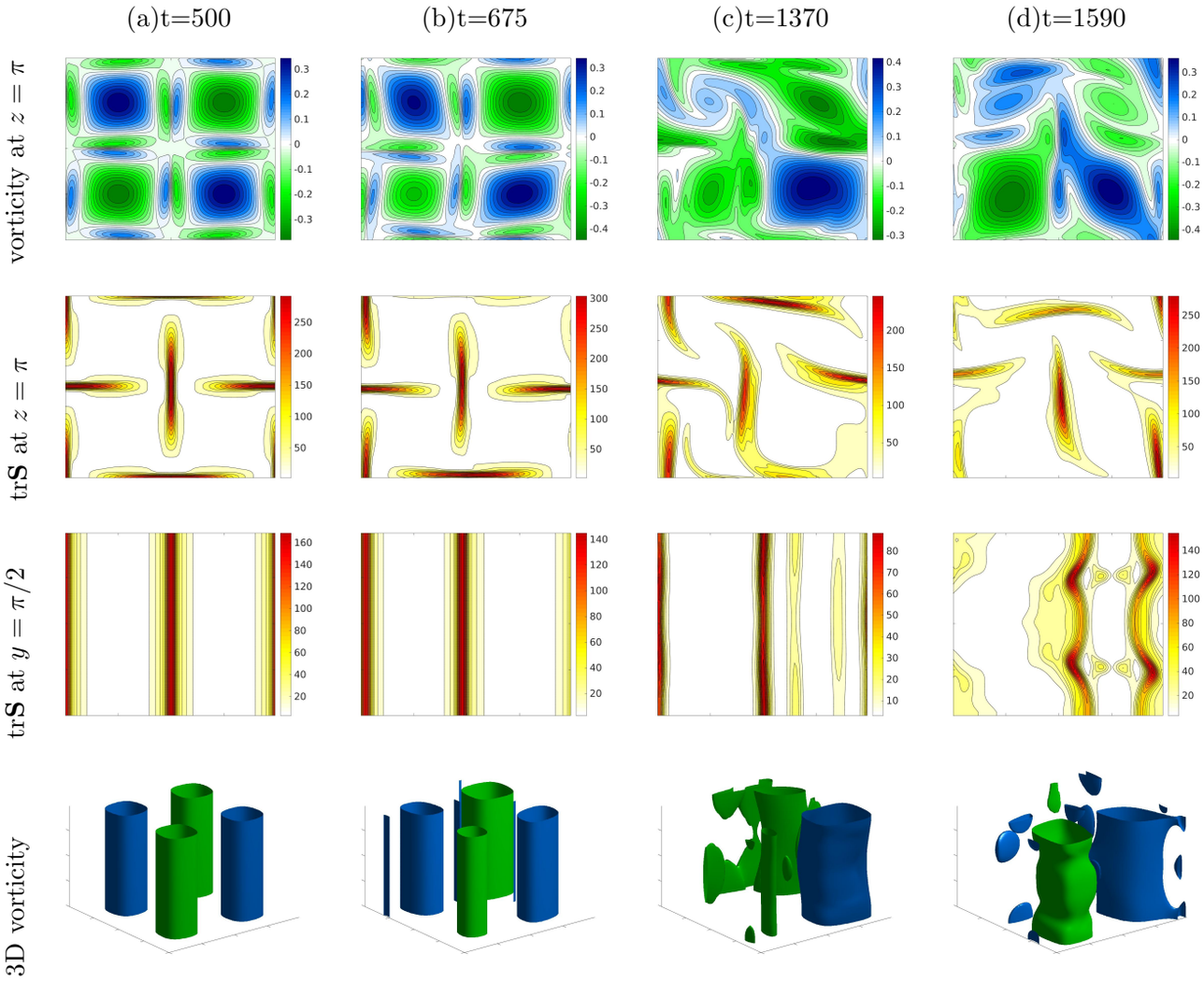

FIG. 3. Solution for Wi = 8 at (a) t=500, (b) t=675, (c) t=1370 and (d) t=1590. First row: Contours of azimuthal vorticity at $z = \pi$. Second row: contours of tr$\mathbf{S}$ at $z = \pi$. Third row: contours of tr$\mathbf{S}$ at $y = \pi/2$. Fourth row: iso-surfaces of azimuthal vorticity for the values of ± 0.20. (Multimedia view)

evolution of tr$\mathbf{S}$ along the $z-$axis for a fixed x, y location. While we have reviewed the evolution of the $z-$axis in the whole x, y domain, we display only a few of these time evolutions, see Fig. 4. We choose some singular points such as the one at the center of a roll $(x, y) = (\pi/2, \pi/2)$, as well as at the extensional point in center of the domain $(x, y) = (\pi, \pi)$ along with three more generic points at $(x, y) = (1.18, 3.53)$, $(x, y) = (1.18, 2.36)$ and $(x, y) = (1.57, 0.39)$ respectively. The rest of the z, t slices show a consistent pattern

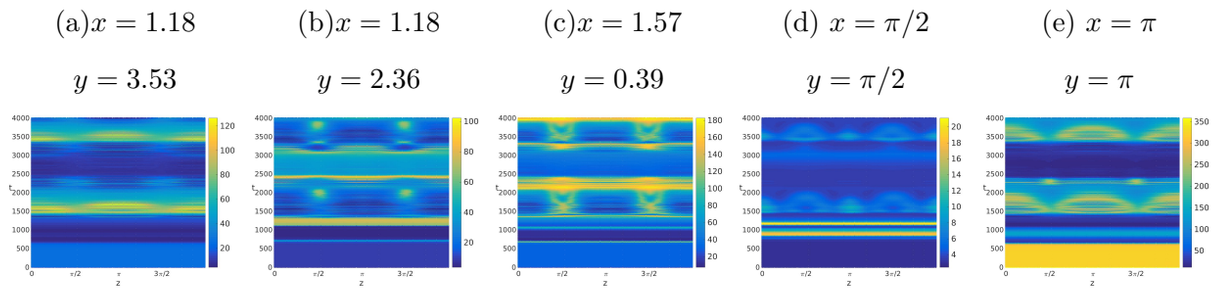

FIG. 4. Time evolution of $z-$axis for tr$\mathbf{S}$ at different x, y locations for Wi = 8: (a) $x = 1.18$ $y = 3.53$, (b) $x = 1.18$ $y = 2.36$, (c) $x = 1.57$ $y = 0.39$, (d) $x = \pi/2$ $y = \pi/2$, (e) $x = \pi$ $y = \pi$.

with the ones presented here. It is evident that for early times ($t < 550$) tr$\mathbf{S}$ is constant in time for each x, y position since at that stage the behavior of the flow is quasi-steady. Later for $550 \leq t \leq 1200$, the value of the tr$\mathbf{S}$ change in time but it is constant along the z axis, corresponding with times where we have a two-dimensional instability with a rotating dominant vortex. For the latest times ($t > 1200$), it is clear how the flow is evolving in time, and it also presents a non-uniform pattern along the z direction. In that range of times, both instabilities are acting simultaneously. Note here that for all the studied cases, the instability in the z-direction was always found to be a low frequency instability, i.e the created pattern in that area is periodic in the $z-$ direction with period $2\pi/n$, where n is the frequency number.

2. 3D instability first (Wi $\geq$ 10)

For cases with Wi ≥ 10, the flow develops first the z instability before it becomes unstable in the x, y plane. Contour plots of the vorticity, tr$\mathbf{S}$, vertical slices as well as isosurfaces for Wi = 12 are shown in Fig. 5. Initially, the flow remains a quasi-steady symmetric flow, Fig. 5(a). Then, around $t = 205$, a three-dimensional flow instability appears. This instability is most clear in the representations of 3D isosurfaces of vorticity where the original cylinder appears to be bending, Fig. 5(b). This bending is even more evident later, e.g. Fig. 5(c). When looking at details of the solutions, we can appreciate both bending and pinching affects the cylinders, see Fig. 5(d) t=445. It is important to remark here that at these times, still, the four vortices have similar magnitude as is most clear in the 2D representations at the

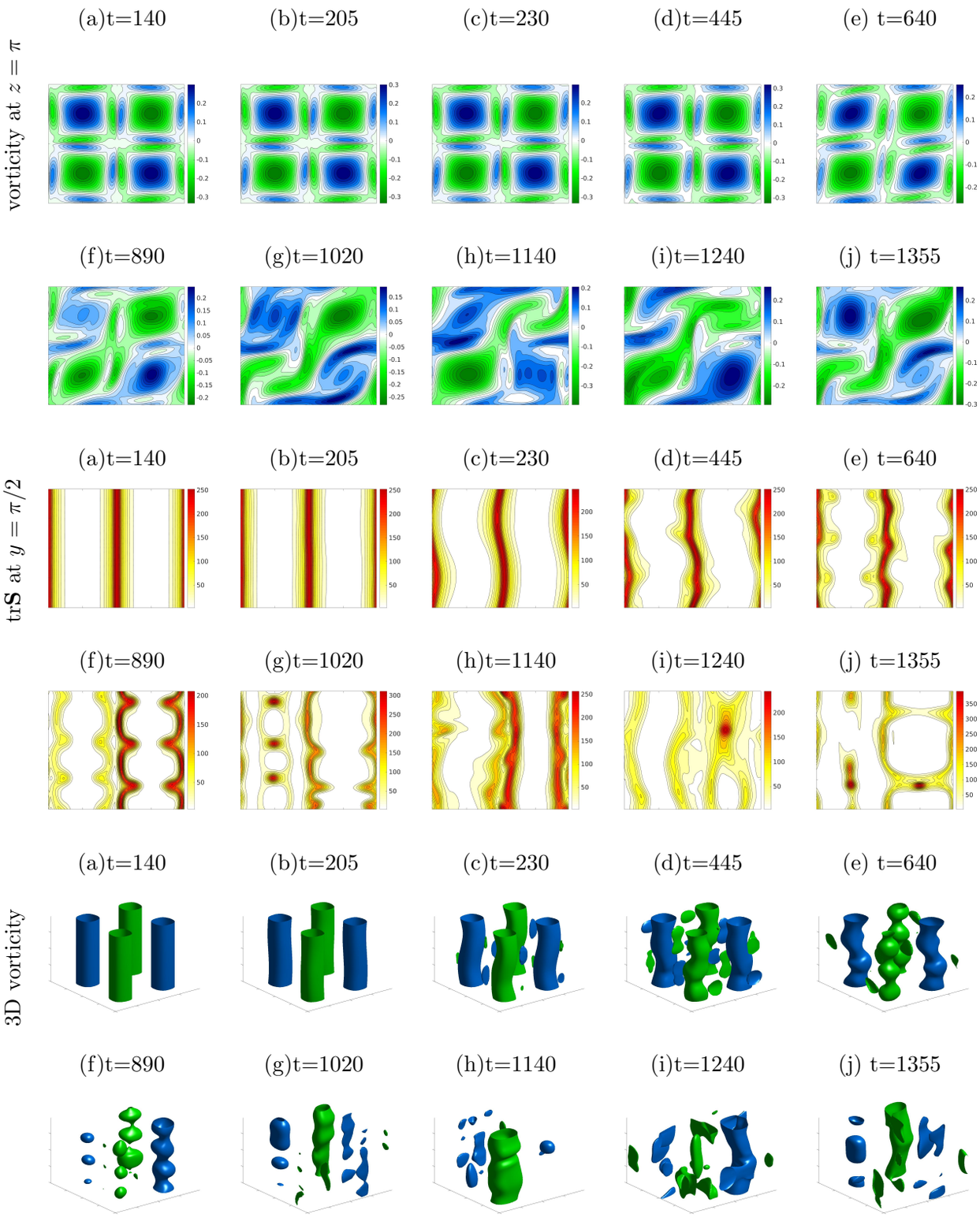

FIG. 5. Solution for Wi = 12 at (a)t=140, (b)t=205, (c)t=230, (d)t=445, (e) t=640, (f)t=890, (g)t=1020, (h)t=1140, (i)t=1240 and (j) t=1355. First and second row: Contours of azimuthal vorticity at $z = \pi$. Third and fourth row: vertical contours of tr$\mathbf{S}$ at $y = \pi/2$. Fifth and sixth row: 3D iso-surfaces of azimuthal voticity for the values ± 0.20. (Multimedia view)

central z plane. For further times, around $t = 775$, one of the vortex starts being weaker and another one stronger, as was typically found in the 2-dimensional time evolutions. This effect leads to complex evolutions for further times where both the z and the x, y temporal evolutions are simultaneously creating a flow where there is bending in the vortex tubes, pinching, and some vortex dominates the others. See sequence of Figs. 5(f), 5(g), 5(h), and 5(i).

The vertical cuts for Fig. 5 are also very useful to see how the $z-$ dependence evolves in time. For some cases, for example Fig. 5(f), an instability with frequency 3 is appreciable as cells in tr$\mathbf{S}$. At this instant, each of the cells (corresponding to strong pinching) has roughly the same size. This instability is also observable in the vortex tube where the isosurfaces structure has similarly sized "beads" of constant vorticity. Subsequently, these "beads" periodically increase and decrease in size, see Fig. 5 (g). For further times (Fig. 5(h)), the pinching is not so strong in the dominant vortex creating a pattern that looks more like tubes than cells, see the 3D vorticity plot. Later the tubes evolve to more asymmetric solutions in the z direction Fig. 5 (i), and they recover a two-mode cell pattern, Fig. 5 (j). This process of creating and destroying cells with spatial frequencies 2 or 3 continues in time (our simulations ran to t=4000) creating complicated flow patterns. See also the movies (Multimedia view).

Figure 6 shows the time evolution of tr$\mathbf{S}$ as a function of z for fixed x, y with Wi = 12 for different x, y locations. We see the flow becoming unstable in the z direction around $t = 205$, developing three-dimensional time-dependent behavior. Note that since there is no significant displacement in the x and y directions at early times, there are no large changes in tr$\mathbf{S}$ values from one time to the next (see the bottom section of Fig. 6 advancing in the vertical direction). At about $t = 775$, when the dominant vortex starts rotating, the displacement visible in the time evolution of tr$\mathbf{S}$ shows additional features now. We can see variations in tr$\mathbf{S}$ when comparing values at the same time and different z, but also when comparing different times and keeping the same z. Together with Figs. 5 this paints the picture that the regions of large stress are rotating along with the dominant vortex around the four cylinders, but there is also variation along the $z-$axis of this rotation and the stress concentration. When the dominant vortex is passing through a particular x, y position, the value of tr$\mathbf{S}$ is larger along the $z-$ axis compared with those times when a weak vortex is passing that x, y position. This behavior persists in time.

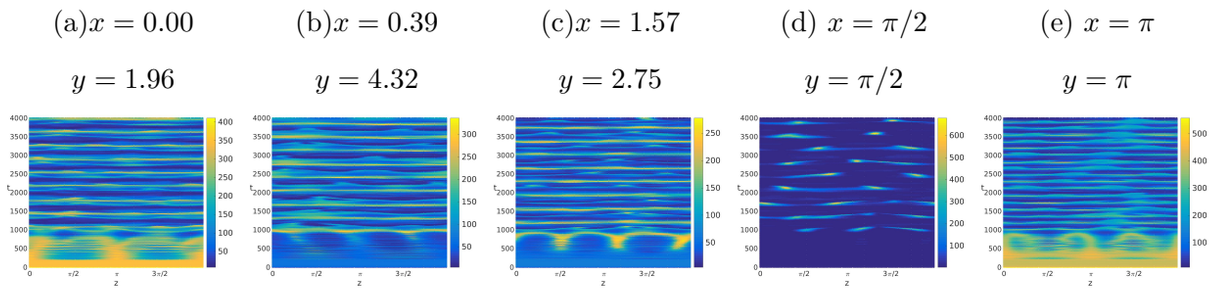

FIG. 6. Time evolution of $z-$axis for tr$\mathbf{S}$ at different x, y locations for Wi = 12: (a) $x = 0.00$ $y = 1.96$, (b) $x = 0.39$ $y = 4.32$, (c) $x = 1.57$ $y = 2.75$, (d) $x = \pi/2$ $y = \pi/2$, (e) $x = \pi$ $y = \pi$.

IV. FENE-P RESULTS

We found that there is no $z-$instability for Wi < 12 for the FENE-P model, but we find the $z-$instability for Wi = 12. In simulations with Wi = 12, the $z-$instability persists in time, but now we find periodic temporal behavior. Different initial conditions were used, all arriving at different final states that are periodic. In these states, the $z-$instability is persistent, and there is no sign of the dominant vortex rotating around the four cylinders as in some of the Oldroyd-B solutions. Figure 7 shows snapshots of the fully developed periodic flow for two solutions obtained for Wi = 12 using the FENE-P model. These two different results come from using two different initial conditions. The first initial condition, hereafter IC1, uses an initial conformation tensor taken from solutions to the Oldroyd-B model with Wi = 8 at $t = 4000$, at this point the 2D flow asymmetry and $z-$spatio-temporal behavior has already begun. The second initial condition, hereafter IC2, comes from an early solution with Wi = 10 and $t = 200$, where the 2D symmetry break and $z-$dependence have not yet happened. In Fig. 7 the first row of each group shows the vorticity at $z = \pi$, over nearly a period where it is appreciable that there is no rotation of the main vortex for any solution. The following rows display a vertical plane of tr$\mathbf{S}$ passing through $y = \pi/2$. The $z-$dependence shows 2 modes in the right-hand side of the IC1 solution. Last, the 3D representations of the vorticity are shown where the $z-$instability and periodicity of the solutions can be seen by the eye. Note here that the solutions are displayed in a time interval of $\Delta t = 5$, which is not necessarily a fraction of the period of the solution, therefore the first and last figures of each row are not exactly equal. See also

the movies (Multimedia view).

Figure 8 shows the time evolution of the $z-$axis for fixed x, y, Wi $= 12$ and different initial conditions, demonstrating the periodic temporal behavior. Note that the z positions were picked arbitrarily, and other locations show similar behavior. When comparing the FENE-P temporal behavior shown in Fig. 8 with the Oldroyd-B simulation in Fig. 6 we note that the FENE-P solutions show traveling waves in the $z-$axis and no evidence of the rotating vortices that were seen in Oldroyd-B.

V. CHARACTERIZING THE INSTABILITY IN THE $z-$DIRECTION

In order to characterize the instability in the $z-$direction we focus on an extensional point in the flow. Here we focus on $(x, y) = (\pi, \pi)$, and examine the behavior of the stress and velocity at the onset of the $z-$dependence. We will first examine the nonlinear simulations presented in Secs.III B 1 and III B 2 for Wi $= 8, 12$, and then we will consider a linearized problem that is related to the transition we see for Wi $= 12$.

A. Onset of instability in nonlinear simulations

In Fig. 9 (a) we plot the S_{11}, S_{12}, S_{22} components of the stress tensor at the central stagnation point $(x, y) = (\pi, \pi)$ at $z = 0.88$ (an arbitrarily chosen z value) over time for the Wi $= 8$, Oldroyd-B simulation. At $t \approx 1300$ we note that these components of the stress tensor begin to depend on z. This is correlated with the growth of the $|S_{13}|, |S_{23}|, |S_{33} - 1|$ components of the stress tensor deviating away from the 2D solution which has $S_{13} = S_{23} = 0$ and $S_{33} = 1$. We note that all of the components of the stress tensor were initially perturbed, but these three components go to zero rapidly and remain zero as long at the flow remains quasi-2D. The onset of the $z-$instability corresponds with the growth of these stress components. This is seen as well for Wi $= 12$, shown in Fig. 10. We plot the separate components of S_{11}, S_{12}, S_{22} due to their different scales. In this case the flow is initially symmetric (in 2D and constant in z) as is seen in Fig. 5 (a), (after some transient due to the initial perturbation) and the flow is steady until the S_{13}, S_{23}, S_{33} components become sufficiently large and begin to effect the constant $z-$flow state. In Fig. 11 we plot the temporal behavior of $\partial_z u, \partial_z v, \partial_x w, \partial_y w$ at $(x, y) = \pi, \pi$ for $z = 0.88$. These are

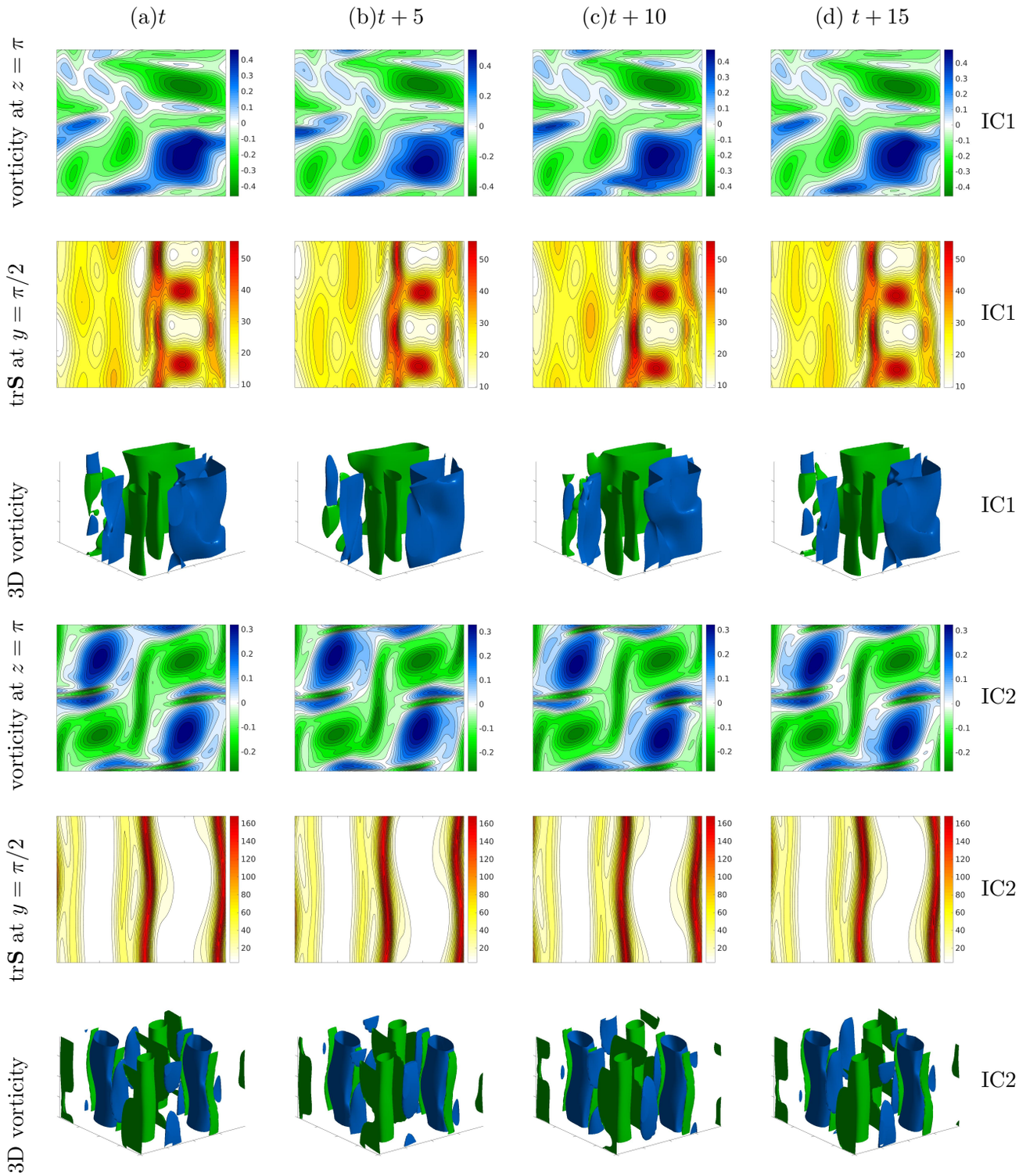

FIG. 7. Time evolution azimuthal vorticity at $z = \pi$, tr$\mathbf{S}$ at a vertical plane $y = \pi/2$ and 3D iso-surfaces of azimuthal vorticity for the values ± 0.20 with FENE-P Wi = 12. First group starting from initial condition of Oldroyd-B solution for Wi = 8 at $t = 4000$. Second group starting from initial condition of Oldroyd-B solution for Wi = 10 at $t = 100$. (a) t, (b) t+5, (c) t+10, (d) t+15 (Multimedia view)

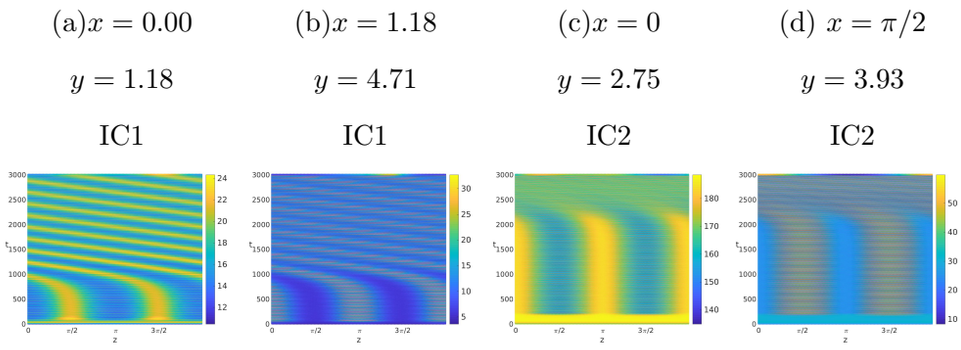

FIG. 8. Time evolution of $z-$axis for tr$\mathbf{S}$ at different x, y locations for Wi = 12, FENE-P. (a) $x = 0.00$ $y = 1.18$ IC1, (b) $x = 1.18$ $y = 4.71$ IC1, (c) $x = 0.00$ $y = 2.75$ IC2, (d) $x = \pi/2$ $y = 3.93$ IC2.

the components of the velocity gradient that are zero when the flow is quasi-2D, and their growth corresponds to the onset of the $z-$instability. We note that in these simulations we have sampled the data to plot with $\Delta t = 5$ which is rather coarse and hence after the onset of the $z-$dependence the time series is not well resolved in the figure.

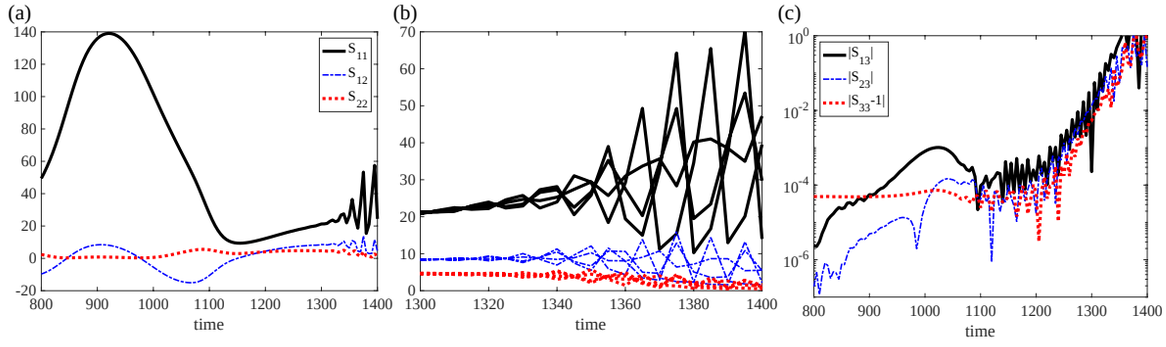

FIG. 9. Data from Oldroyd-B simulation described in Sec. III B 1 for Wi = 8. (a) Temporal behavior of S_{11}, S_{12}, S_{22} components of the conformation tensor at $(x, y) = (\pi, \pi)$ for $z = 0.88$. (b) Temporal zoom of data from (a) but plotted at 4 different z values between 0.88-3.14. (d) Temporal behavior of $|S_{13}|, |S_{23}|, |S_{33} - 1|$ components of the conformation tensor at $(x, y) = (\pi, \pi)$ for $z = 0.88$, note the log scale on the $y-$axis.

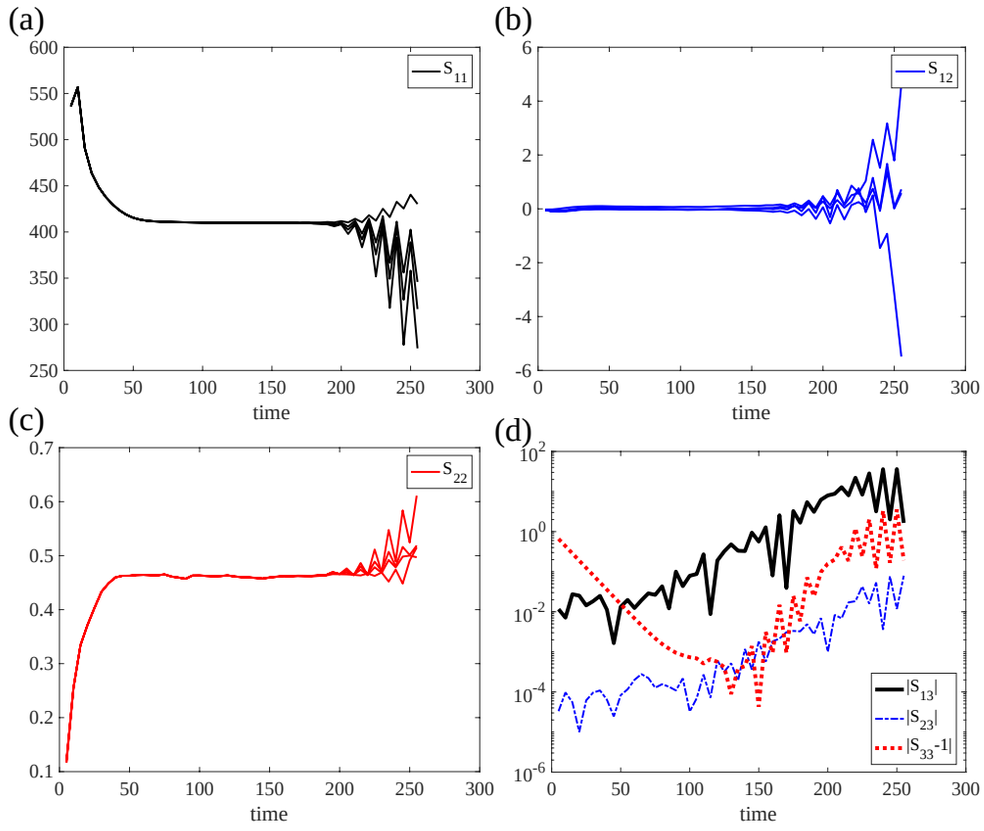

FIG. 10. Data from Oldroyd-B simulation described in Sec. III B 2 for Wi = 12. Temporal behavior of (a) S_{11}, (b) S_{12}, and (c) S_{22} components of the conformation tensor at $(x, y) = (\pi, \pi)$ plotted at 4 different z values between 0.88-3.14. (c) Temporal behavior of $|S_{13}|, |S_{23}|, |S_{33} - 1|$ components of the conformation tensor at $(x, y) = (\pi, \pi)$ for $z = 0.88$, note the log scale on the $y-$axis.

B. Linear perturbations

We have observed that an instability develops in the $z-$direction for a range of sufficiently large Wi, and we noted that the onset of $z-$dependence occurs both when the flow in x, y has already transitioned to a quasi-periodic asymmetric state (the example above was for Wi = 8) and when the x, y flow is steady (Wi = 12). The simpler case to analyze is when the x, y flow is steady. Here we examine a numerical linearized flow where the background state is symmetric in x, y and steady. To obtain the 3D background solution we first evolve the Stokes-Oldroyd-B system (i.e. Eq. (1)-(3)) in two space dimensions to a symmetric steady state with a four-roll mill background force. The arrangement of the flow is similar to that shown in Fig. 3 at $t = 500$ (in 2D). We extend the 2D solutions to 3D by making them

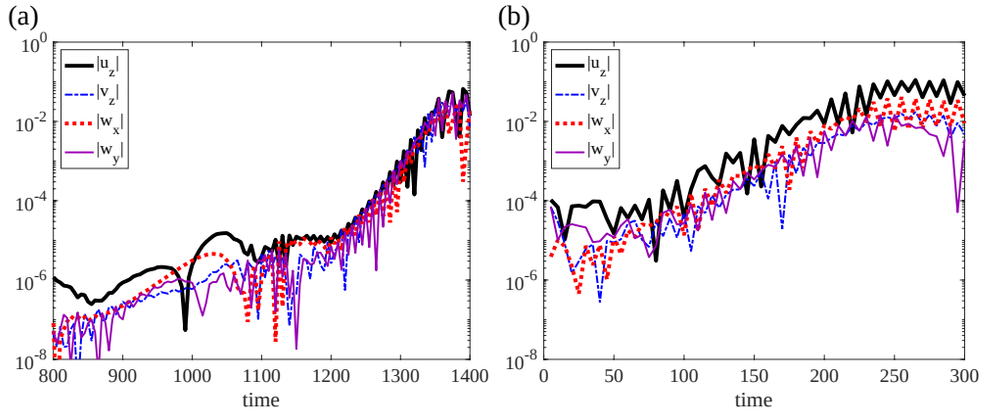

FIG. 11. Data from Oldroyd-B simulation described in Secs.III B 1 and III B 2 for (a) $\mathrm{Wi} = 8$ and (b) $\mathrm{Wi} = 12$. Temporal behavior of $\partial_z u, \partial_z v, \partial_x w, \partial_y w$ at $(x, y) = (\pi, \pi)$ for $z = 0.88$, note the log scale on the $y-$axis.These are components of the velocity gradient that are zero when there is no $z-$dependence in the flow.

constant in z, (and rename $\bar{S}_{ij}(x, y)$ to $\bar{S}^0_{ij}(x, y, z)$, and similarly for the velocity). Then we define the 3D conformation tensor as

$$\mathbf{S}^0 = \begin{bmatrix} \bar{S}^0_{11} & \bar{S}^0_{12} & 0 \\ \bar{S}^0_{12} & \bar{S}^0_{22} & 0 \\ 0 & 0 & 1 \end{bmatrix} \tag{7}$$

with corresponding velocity

$$\mathbf{u}^0 = \begin{bmatrix} \bar{u}^0 \\ \bar{v}^0 \\ 0 \end{bmatrix}. \tag{8}$$

It is easy to see that $(\mathbf{u}^0, \mathbf{S}^0)$ will solve Eq. (1)-(3) in 3D given the 2D solution. Now we consider perturbations around this background (numerical) solution, i.e. let

$$\mathbf{S} = \mathbf{S}^0 + \widetilde{\mathbf{S}}, \quad \text{and} \quad \mathbf{u} = \mathbf{u}^0 + \widetilde{\mathbf{u}}, \tag{9}$$

then the perturbation $(\widetilde{\mathbf{u}}, \widetilde{\mathbf{S}})$, satisfies:

$$\Delta\widetilde{\mathbf{u}} - \nabla\tilde{p} + \beta\nabla\cdot\widetilde{\mathbf{S}} = 0 \tag{10}$$

$$\nabla\cdot\widetilde{\mathbf{u}} = 0 \tag{11}$$

$$\partial_t\widetilde{\mathbf{S}} + \mathrm{Wi}^{-1}\widetilde{\mathbf{S}} - \nu\Delta\widetilde{\mathbf{S}} = -\mathcal{N}(\mathbf{u}^0, \widetilde{\mathbf{S}}) - \mathcal{N}(\widetilde{\mathbf{u}}, \mathbf{S}^0) - \mathcal{N}(\widetilde{\mathbf{u}}, \widetilde{\mathbf{S}}) \tag{12}$$

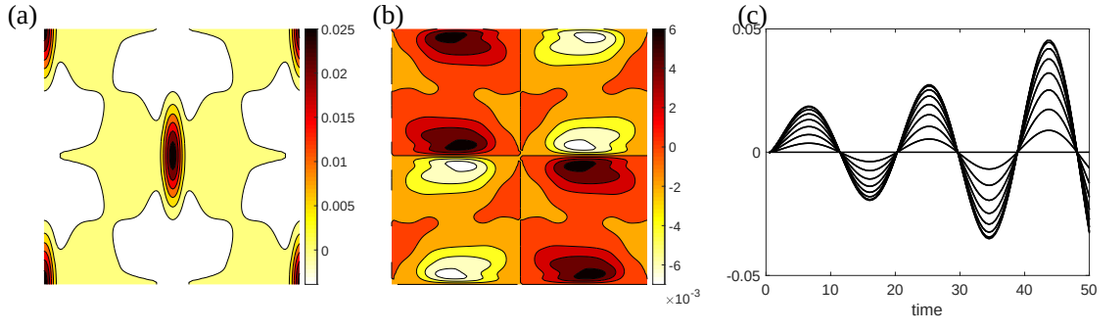

FIG. 12. Solutions from linear evolution of Oldroyd-B system with Wi = 12. (a) Contours of $\tilde{S}_{13}(x, y, \pi/2, t_e)$ for $t_e = 24.5$ (b) Contours of $\tilde{S}_{23}(x, y, \pi/2, t_e)$ for $t_e = 24.5$ (c)$\tilde{S}_{13}(\pi, \pi, z, t)$, for several locations $0 < z < \pi$ and Wi = 12.

where $\mathcal{N}(\mathbf{u}, \mathbf{S}) = \mathbf{u} \cdot \nabla \mathbf{S} - \left(\nabla \mathbf{u} \mathbf{S} + \mathbf{S} \nabla \mathbf{u}^T\right)$ are all the quadratic terms, and the nonlinear terms are given by $\mathcal{N}(\widetilde{\mathbf{u}}, \widetilde{\mathbf{S}})$. We do not have a closed form solution for $(\mathbf{u}^0, \mathbf{S}^0)$ necessitating a numerical study of the system. We numerically solve the linear system (i.e. Eqs. (10)-(12) but dropping the terms $\mathcal{N}(\tilde{u}, \tilde{S})$) from different initial conditions, and for different Wi, to see if small perturbations grow or decay. Here we demonstrate, by an example where we perturb a single $z-$mode, that there is a linear instability in this system beyond a critical Wi. We show that with an initial perturbation only to a single mode in z of the 13-component of $\widetilde{\mathbf{S}}$, that we have growth of the perturbation for Wi = 12 and decay of the perturbation for Wi = 8. This is not meant to be exhaustive but rather to indicate that there is a linear instability in this system and also to describe the behavior of the instability. A full analysis of the numerical eigenvalues-eigenfunctions is beyond the scope of this work.

We start with an initial perturbation of the form $\tilde{S}_{13}(x, y, z, 0) = \varepsilon \sin z$, with $\varepsilon = 0.001$. Solving the Stokes equation with this initial perturbation of the conformation tensor gives an initial perturbation to the velocity of the form $\tilde{u}(x, y, z, 0) = -\varepsilon\beta \cos z$, with $\tilde{v}, \tilde{w} \equiv 0$. When we examine the solutions with this initial data we find that due to the structure of the equations a "partition" of the $z-$axis is created where initially some of the stress components grow where $\sin z \approx 1$ and some terms grow where $\cos z \approx 1$. This particular initial condition seems to accentuates this phenomena. We examine the structure of the equations that creates/accentuates this partition next.

The terms that grow where $\sin z \approx 1$ are $\tilde{S}_{13}$ and $\tilde{S}_{23}$, along with $\tilde{w}$, and $\partial_z \tilde{u}, \partial_z \tilde{v}, \partial_x \tilde{w}, \partial_y \tilde{w}$. We show contours of the (x, y) spatial dependence of these terms in Figs. 12 and 13. For

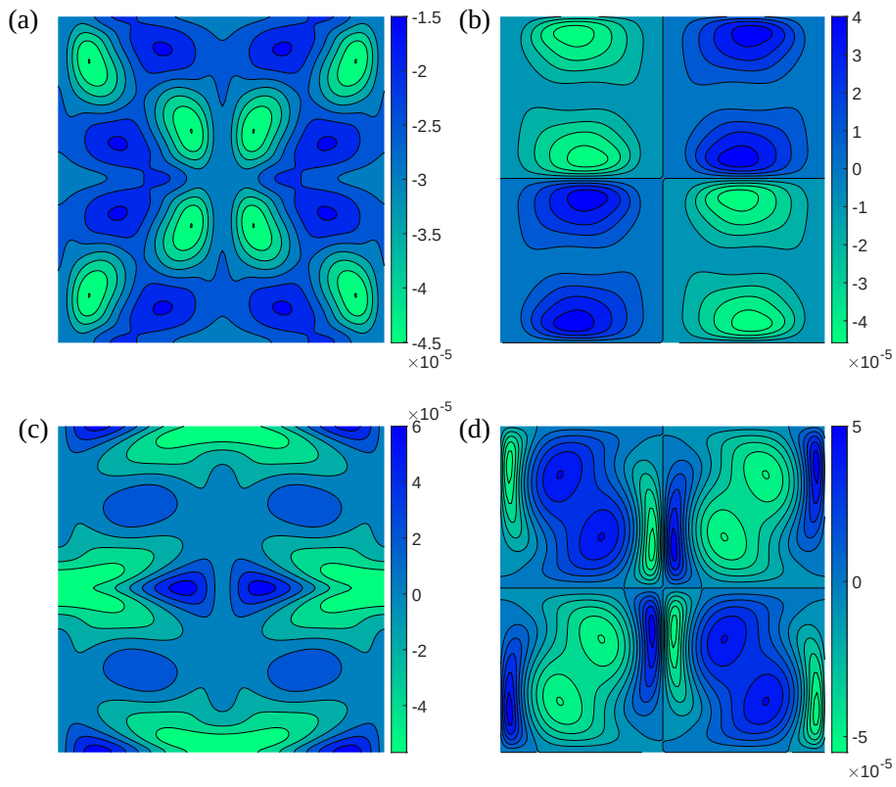

FIG. 13. Components of the velocity gradient at $t_e = 24.5$, Wi $= 12$. (a) $\partial_z \tilde{u}(x, y, \pi/2, t_e)$ (b) $\partial_z \tilde{v}(x, y, \pi/2, t_e)$ (c) $\partial_x \tilde{w}(x, y, \pi/2, t_e)$ (d) $\partial_y \tilde{w}(x, y, \pi/2, t_e)$

Wi $= 12$ the perturbation grows and contours of $\tilde{S}_{13}(x, y, z^*, t_e)$ and $\tilde{S}_{23}(x, y, z^*, t_e)$ are shown in Fig. 12 (a),(b) where we choose $t_e = 24.5$ as a sample early time point and $z^* = \pi/2$. We note that the x, y structure of the $\tilde{S}_{13}$ term, Fig. 12(a), is largest at the extensional point at (π, π) and extended along the $y-$axis, similar to the $\bar{S}^0_{11}$ component of the background solution. However the x, y structure of the $\tilde{S}_{23}$ term, Fig. 12(b) shows concentration along the axis of compression. As we see in Fig. 12(c) the instability has begun to grow but it is early in the evolution of the instability. All other components of the conformation tensor are zero at z^* to machine precision at this time.

We also show components of the perturbation to the velocity gradients at this early time in Fig. 13. These four components, $\partial_z \tilde{u}, \partial_z \tilde{v}, \partial_x \tilde{w}, \partial_y \tilde{w}$ as well as $\tilde{w}$ (not shown) are the only non-zero components of the velocity gradient at z^*, t_e. We write the evolution of $\tilde{S}_{13}$ and $\tilde{S}_{23}$ out explicitly below as there is some simplification due to the structure of the background

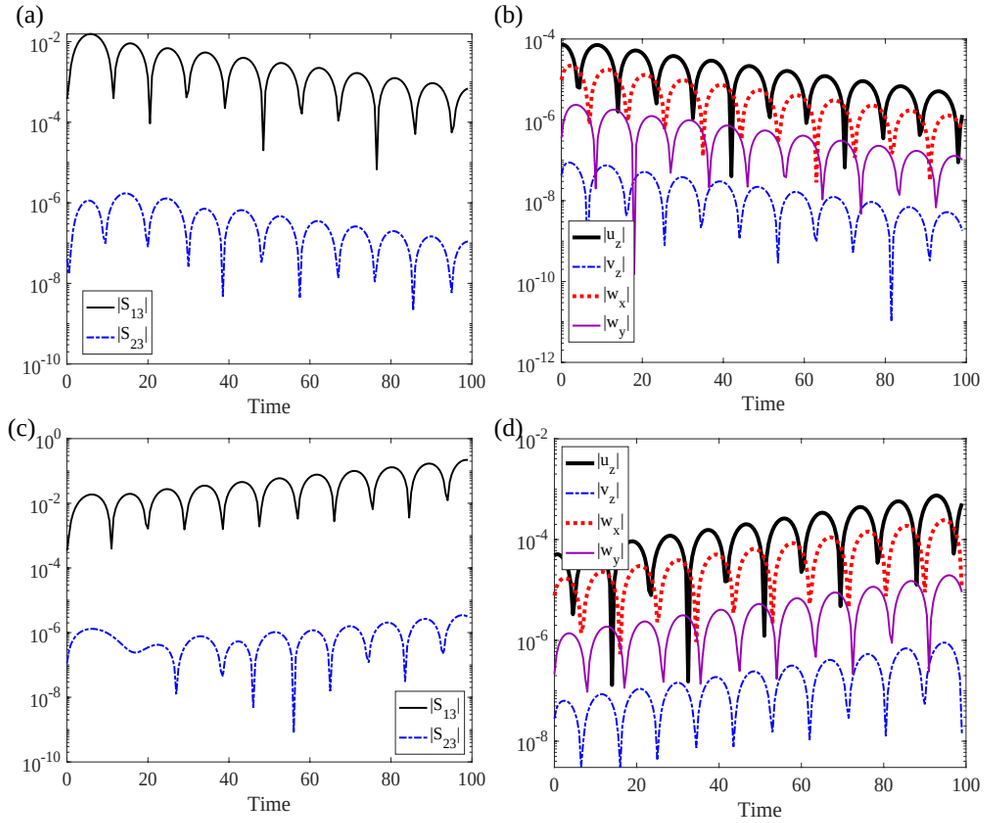

FIG. 14. (a)-(b) Wi = 8, (c)-(d) Wi = 12. Temporal evolution of linear perturbation for $|\tilde{S}_{13}|, |\tilde{S}_{23}, |\partial_z \tilde{u}|, |\partial_z \tilde{v}|, |\partial_x \tilde{w}|, |\partial_y \tilde{w}|$ at $(\pi, \pi, \pi/2)$.

solution. In other words we expand Eq. (12) as

$$\partial_t \tilde{S}_{13} + \frac{1}{\mathrm{Wi}} \tilde{S}_{13} - \eta \Delta \tilde{S}_{13} = -(\bar{u}^0 \partial_x + \bar{v}^0 \partial_y) \tilde{S}_{13} + \partial_x \tilde{w} \bar{S}^0_{11} + \partial_y \tilde{w} \bar{S}^0_{12} + \partial_z \tilde{u} + \partial_x \bar{u}^0 \tilde{S}_{13} + \partial_y \bar{u}^0 \tilde{S}_{23} \tag{13}$$

$$\partial_t \tilde{S}_{23} + \frac{1}{\mathrm{Wi}} \tilde{S}_{23} - \eta \Delta \tilde{S}_{23} = -(\bar{u}^0 \partial_x + \bar{v}^0 \partial_y) \tilde{S}_{23} + \partial_x \tilde{w} \bar{S}^0_{12} + \partial_y \tilde{w} \bar{S}^0_{22} + \partial_z \tilde{v} + \partial_x \bar{v}^0 \tilde{S}_{13} + \partial_y \bar{v}^0 \tilde{S}_{23} \tag{14}$$

Examining equations (13)-(14) we note that it is exactly the above listed components of the velocity that are involved in the evolution of $\tilde{S}_{13}, \tilde{S}_{23}$ at z^*. This implies a linear evolution of the components that has the form $e^{\alpha t} f(x, y) \sin z$ for short times. The real part of α is positive for Wi = 12 and the imaginary part is nonzero. However the Stokes equations couples all of the stress components in a non-local manner and deriving exactly how α depends on the background solution is beyond the scope of this work. It is clear from

the x, y spatial dependence of the components shown in Figs. 12 and 13 that the spatial structure of these terms is non-trivial and also relevant in the dynamics. In particular in Eq. (13) we see that the background $\bar{S}^0_{11}$ solution is driving the growth of $\tilde{S}_{13}$ via the term $\partial_x \tilde{w} \bar{S}^0_{11}$.

The spatial structure of these stress components are very similar (not shown) for $\mathrm{Wi} = 8$ at early times, but the initial perturbation shows decaying oscillations indicating that $\mathrm{Wi} = 8$ is linearly stable with respect to this initial condition. This is shown in Fig. 14 where we display the evolution of the components above at $(\pi, \pi, \pi/2)$ indicating that this perturbation decays for $\mathrm{Wi} = 8$, Fig. 14 (a,b), and grows for $\mathrm{Wi} = 12$, Fig. 14 (c,d).

We have simulated a range of Wi and find that $\mathrm{Wi} \approx 9.7$ is where the flow becomes linearly unstable to this perturbation, but we do not have a precise explanation for this value. Examining Eq. (13) we can see a cartoon of a possible instability criteria where the decay terms $-\frac{1}{\mathrm{Wi}}\tilde{S}_{13} + \eta\Delta\tilde{S}_{13}$ must be overcome by the other terms (for example) $\partial_x \tilde{w}\bar{S}^0_{11} + \partial_z \tilde{u} + \partial_x \bar{u}^0 \tilde{S}_{13}$ but again the coupling via Stokes equation and how $\tilde{w}, \tilde{u}$ depend on $\tilde{S}$ must be understood more fully before this argument can be made precise and predictive of the instability.

The evolution of the terms $\tilde{S}_{11}, \tilde{S}_{12}, \tilde{S}_{22}$ in the conformation tensor are given below in Eq. (15)-(17):

$$\begin{aligned}\partial_t \tilde{S}_{11} + \frac{1}{\mathrm{Wi}}\tilde{S}_{11} - \eta\Delta\tilde{S}_{11} &= -(\tilde{u}\partial_x + \tilde{v}\partial_y)\bar{S}^0_{11} - (\bar{u}^0\partial_x + \bar{v}^0\partial_y)\tilde{S}_{11} \\ &+ 2(\partial_x\tilde{u}\bar{S}^0_{11} + \partial_y\tilde{u}\bar{S}^0_{12}) + 2(\partial_x\bar{u}^0\tilde{S}_{11} + \partial_y\bar{u}^0\tilde{S}_{12})\end{aligned} \tag{15}$$

$$\begin{aligned}\partial_t \tilde{S}_{12} + \frac{1}{\mathrm{Wi}}\tilde{S}_{12} - \eta\Delta\tilde{S}_{12} &= -(\tilde{u}\partial_x + \tilde{v}\partial_y)\bar{S}^0_{12} - (\bar{u}^0\partial_x + \bar{v}^0\partial_y)\tilde{S}_{12} \\ &+ (\partial_x\tilde{u} + \partial_y\tilde{v})\bar{S}^0_{12} + \partial_x\tilde{v}\bar{S}^0_{11} + \partial_y\tilde{u}\bar{S}^0_{22} + \partial_x\bar{v}^0\tilde{S}_{11} + \partial_y\bar{u}^0\tilde{S}_{22}\end{aligned} \tag{16}$$

$$\begin{aligned}\partial_t \tilde{S}_{22} + \frac{1}{\mathrm{Wi}}\tilde{S}_{22} - \eta\Delta\tilde{S}_{22} &= -(\tilde{u}\partial_x + \tilde{v}\partial_y)\bar{S}^0_{22} - (\bar{u}^0\partial_x + \bar{v}^0\partial_y)\tilde{S}_{22} \\ &+ 2(\partial_x\tilde{v}\bar{S}^0_{12} + \partial_y\tilde{v}\bar{S}^0_{22}) + 2(\partial_x\bar{v}^0\tilde{S}_{12} + \partial_y\bar{v}^0\tilde{S}_{22}).\end{aligned} \tag{17}$$

These terms

all have $z-$dependence like $\cos z$ on short times, and this is due to the fact that at $t = 0$, $\tilde{u}(x, y, z, 0) = -\varepsilon\beta\cos z$, which introduces the $z-$dependence into all of these terms. However, the growth of the instability does not appear to be tied to these terms because these terms are effectively acting only in the x, y plane.

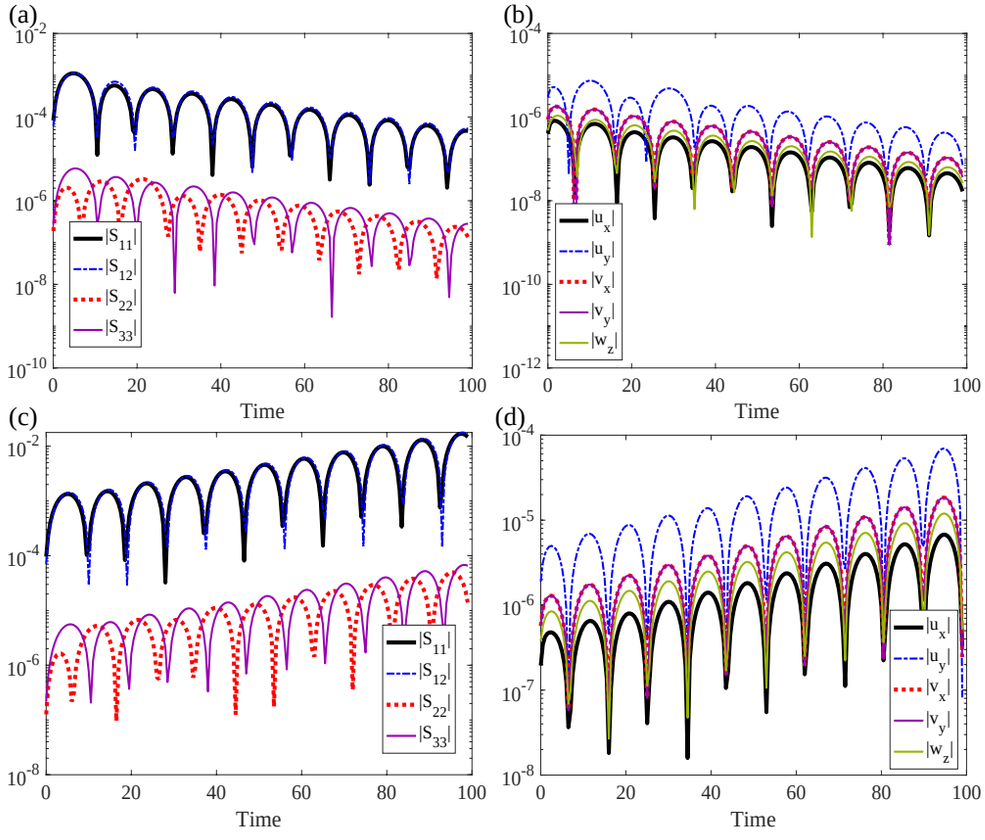

FIG. 15. (a)-(b) Wi = 8, (c)-(d) Wi = 12. Temporal evolution of linear perturbation for $|\tilde{S}_{11}|, |\tilde{S}_{12}|, |\tilde{S}_{22}|, |\tilde{S}_{33}|, |\partial_x\tilde{u}|, |\partial_y\tilde{u}|, |\partial_x\tilde{v}|, |\partial_y\tilde{v}|, |\partial_z\tilde{w}|$ at $(\pi, \pi, 0)$.

Finally the $\tilde{S}_{33}$ component evolves according to Eq. (18) below,

$$\partial_t\tilde{S}_{33} + \frac{1}{\mathrm{Wi}}\tilde{S}_{33} - \eta\Delta\tilde{S}_{33} = -(\bar{u}^0\partial_x + \bar{v}^0\partial_y)\tilde{S}_{33} + 2\partial_z\tilde{w}. \tag{18}$$

As $\tilde{S}_{13}$ becomes spatially dependent, the $z-$dependence enters $\tilde{w}$ via Stokes equation, and hence (matching derivatives) $\tilde{w}$ will depend on z as $\tilde{S}_{13}$ via $\sin z$ and hence $\partial_z\tilde{w} \sim \cos z$. The growth of $\tilde{S}_{33}$ is essential to the linear instability and this is where a criteria for instability is most likely to be found. If we can analytically understand the relationship between $\partial_z\tilde{w}$ and $\tilde{S}_{33}$ then a criteria related to Wi seems likely to follow.

The perturbative terms in Eq. (15)-(18) are all largest (in absolute value) at $z = 0$, consistent with $z-$ structure $\sim \cos z$ and this is precisely where the previous terms $(\tilde{S}_{13}, \tilde{S}_{23}, \tilde{w}, \partial_z\tilde{u}, \partial_z\tilde{v}, \partial_x\tilde{w}, \partial_y\tilde{w})$ are zero (to machine precision). In Fig. 15 we show the evolution of these components at $(\pi, \pi, 0)$ for Wi = 8 and Wi = 12. Again we find that the perturbation decays for Wi = 8 (a,b) and grows for Wi = 12 (c,d).

We find that the linear equations can be run on a coarse mesh, i.e. $N = 32$ grid points in each dimension, with results consistent with high resolution simulations, i.e. predicting that the flow is linearly stable for $\mathrm{Wi} = 8$ and unstable for $\mathrm{Wi} = 12$. The stress diffusion is also not necessary in these calculations and the linear simulations with zero stress diffusion still show stability for $\mathrm{Wi} = 8$ and instability for $\mathrm{Wi} = 12$.

VI. CONCLUSION

We have analyzed the dynamics for a viscoelastic fluid at zero Reynolds number in a 3D periodic geometry with a 3D 4-roll mill background force. For small Wi, the flow is steady or has a temporal behavior confined to the x, y directions. However, for sufficiently large Wi, three-dimensional instabilities (instabilities in the z direction) occur. This three-dimensional instability is maintained in time and robust in the sense that it was found with both Oldroyd-B and FENE-P models, using different initial conditions and using different simulation techniques (i.e. both usual formulation and the square root formulation).

For the solutions analyzed using the Oldroyd-B model with $8 \leq \mathrm{Wi} < 10$, the flow develops x, y temporal behavior first, with a dominant vortex rotating around the four quarters, and then the z instability emerges creating three-dimensional behavior where both instabilities are acting simultaneously. However, for $\mathrm{Wi} > 10$, the $z-$instability comes first, with an x, y instability occurring later. For solutions using the FENE-P model, we see the z instability but a simpler periodic state evolves with no significant x, y instability, nor any single dominant vortex.

Finally, we analyzed a particular initial condition that leads to a linear instability in the z direction beyond a critical Wi. This linear instability arises when the background flow is constant in z but highly concentrated along the axis of extension, indicating that it is an instability for the extensional flow geometry. This is a complicated system to analyze for the 4-roll mill solution at zero Reynolds number because the Stokes equation instantly couples all components of the velocity gradient with the stress tensor. The demonstration of a linear instability from the extensional background flow is a first step in understanding this three dimensional instability.

ACKNOWLEDGEMENTS

This work was partially supported by NSF Grant No. DMS-1664679.

[1] Boyand Qin, Paul F. Salipante, Steven D. Hudson, and Paulo E. Arratia. Three-dimensional viscoelastic instabilities in microchannel. *JFM Rapids*, 864 R2:1–11, 2019.

[2] R.J. Poole. Three-dimensional viscoelastic instabilities in microchannel. *JFM*, 870:1–4, 2019.

[3] S. C. Omowunmi and X. F. Yuan. Modelling the three-dimensional flow of a semi-dilute polymer solution in microfluidics-on the effect of aspect ratio. *Rheol Acta*, 49:585–595, 2010.

[4] Feng-Chen Li, Hong-Na Zhang, Yan Cao, Tomoaki Kunugi, Haruyuki Kinoshita, and Marie Oshima. A purely elastic instability and mixing enhancement in a 3d curvilinear channel flow. *Chinese Physical Society*, 29:094704, 2012.

[5] Dahang Tang, Flavio H. Marchsini, Ludwig Cardon, and Dagmar R. D'hooge. Three-dimensional flow simulations for polymer extrudate swell out of slit dies from low to high aspect ratios. *PoF*, 31:093103, 2019.

[6] Simon J Haward, Kazumi Toda-Peters, and Amy Q Shen. Steady viscoelastic flow around high-aspect-ratio, low-blockage-ratio microfluidic cylinders. *Journal of Non-Newtonian Fluid Mechanics*, 254:23–35, 2018.

[7] L Pan, A Morozov, C Wagner, and PE Arratia. Nonlinear elastic instability in channel flows at low reynolds numbers. *Physical review letters*, 110(17):174502, 2013.

[8] S De, JAM Kuipers, EAJF Peters, and JT Padding. Viscoelastic flow simulations in model porous media. *Physical Review Fluids*, 2(5):053303, 2017.

[9] Paulo E Arratia, CC Thomas, J Diorio, and Jerry P Gollub. Elastic instabilities of polymer solutions in cross-channel flow. *Physical review letters*, 96(14):144502, 2006.

[10] RJ Poole, MA Alves, and PJ Oliveira. Purely elastic flow asymmetries. *Physical review letters*, 99(16):164503, 2007.

[11] Li Xi and Michael D Graham. A mechanism for oscillatory instability in viscoelastic cross-slot flow. *Journal of Fluid Mechanics*, 622:145–165, 2009.

[12] A.M. Alfonso, M.A. Alves, and F.T. Pinho. Purely elastic instabilities in three-dimensional cross-slot geometries. *JNNFM*, 165:743–751, 2010.

[13] PC Sousa, FT Pinho, and MA Alves. Purely-elastic flow instabilities and elastic turbulence in microfluidic cross-slot devices. *Soft matter*, 14(8):1344–1354, 2018.

[14] Becca Thomases and Michael Shelley. Emergence of singular structures in Oldroyd-B fluids. *Physics of fluids*, 19(10):103103, 2007.

[15] Becca Thomases and Michael Shelley. Transition to mixing and oscillations in a Stokesian viscoelastic flow. *Physical review letters*, 103(9):094501, 2009.

[16] Becca Thomases, Michael Shelley, and Jean-Luc Thiffeault. A Stokesian viscoelastic flow: transition to oscillations and mixing. *Physica D: Nonlinear Phenomena*, 240(20):1602–1614, 2011.

[17] Becca Thomases. An analysis of the effect of stress diffusion on the dynamics of creeping viscoelastic flow. *Journal of Non-Newtonian Fluid Mechanics*, 166(21):1221–1228, 2011.

[18] Joseph A Biello and Becca Thomases. Equilibrium circulation and stress distribution in viscoelastic creeping flow. *Journal of Non-Newtonian Fluid Mechanics*, 229:101–111, 2016.

[19] RB Bird, PJ Dotson, and NL Johnson. Polymer solution rheology based on a finitely extensible bead–spring chain model. *Journal of Non-Newtonian Fluid Mechanics*, 7(2-3):213–235, 1980.

[20] Nusret Balci, Becca Thomases, Michael Renardy, and Charles R Doering. Symmetric factorization of the conformation tensor in viscoelastic fluid models. *Journal of Non-Newtonian Fluid Mechanics*, 166(11):546–553, 2011.

[21] Paloma Gutierrez-Castillo and Becca Thomases. Proper Orthogonal Decomposition (POD) of the flow dynamics for a viscoelastic fluid in a four-roll mill geometry at the Stokes limit. *Journal of Non-Newtonian Fluid Mechanics*, 264:48–61, 2019.

APPENDIX

Implementation details using GPU

Our simulations require several Fast Fourier Transforms (FFT) and inverses (IFFT) in each iteration. This is because our model evolves entirely in Fourier space, which requires that all nonlinear terms in the upper-convected derivative are handled by performing the multiplications in real space and subsequently inverting the product to advect in Fourier space, with appropriate filtering. In previous, non-parallel implementations, it was found

that computing FFTs (from now on, used as a generalization of FFT and IFFT) in long data sets was the largest bottleneck with regards to the runtime. For this reason, it was decided to parallelize the code so it could run on a Graphics Processing Unit (GPU). While a Central Processing Unit (CPU) can perform each specific addition/multiplication several times faster than a GPU, a GPU can perform between hundreds and thousands of these operations at the same time. In particular, GPUs are specialized for divide-and-conquer algorithms, such as FFT, allowing speeds ups beyond those available from CPUs or even multi-core CPUs.

GPU aided computation is already a well known and well-documented tool, and many programming languages/platforms geared towards computational endeavors have built-in Application Programming Interfaces (APIs) which directly interact with GPUs. In particular, recent versions of MATLAB have built-in support for GPU computing, in a form resembling the typical MATLAB language/design philosophy. MATLAB's GPU computing API automatically calibrates several of MATLAB's native functions to most optimally run on the GPU (e.g. FFT and IFFT). Furthermore, MATLAB's language natively has N-D matrix data-structures with their corresponding operations, and its GPU computing API smoothly accommodates these structures with minimal alterations from the user. For these reasons, we developed a GPU implementation of our spectral code using MATLAB.

We provide a few more details for the interested reader. To speed up the calculations, repetitively calculated or defined variables were initialized at the start and stored on the GPU preemptively. Any quantities to be computed on the GPU were computed from quantities/variables already stored on the GPU. Even simple matrices, such as the identity, were stored on the GPU at the start of the program. This was done for two reasons. Firstly, CPU to GPU data transfer rates are slow relative to normal internal CPU data transfer rates. Secondly, GPU memory allocation is considerably slower than CPU memory allocation. Further stressing awareness of the previous issue, GPUs have a small amount of onboard memory compared to a CPU. For example, the specific GPUs used in the implementation for this paper has only about 8 GB of available memory, meaning that only that much data can be initialized on the GPU. Lastly, GPUs have a smaller memory bandwidth. In other words, performing operations on larger datasets perform slower than trends established on smaller datasets would suggest. In other words, there are diminishing returns in performance beyond a certain threshold amount of data. The significance of this issue varies significantly

between different models of GPUs.

Overall, the GPU implementation of our simulations significantly outperformed the CPU implementation, as illustrated in Table II. We performed our speed up tests on the 2D problem so that we could use fine grids. This was also to test the accuracy of the code by comparing with the CPU version. The finest grid $512^2 = 64^3$ showed a $45\times$ speed up for the simulation. These types of speed ups allowed us to run our long-time simulations on grids 128^3.

TABLE II. 2D simulation speed ups on a run for $0 \leq t \leq 5$.

Resolution	CPU(s)	GPU(s)	Speed-Up
128× 128	11.2275	3.55122	× 3.166
256× 256	98.8118	10.0157	× 9.866
512× 512	1904.8	42.1485	× 45.193

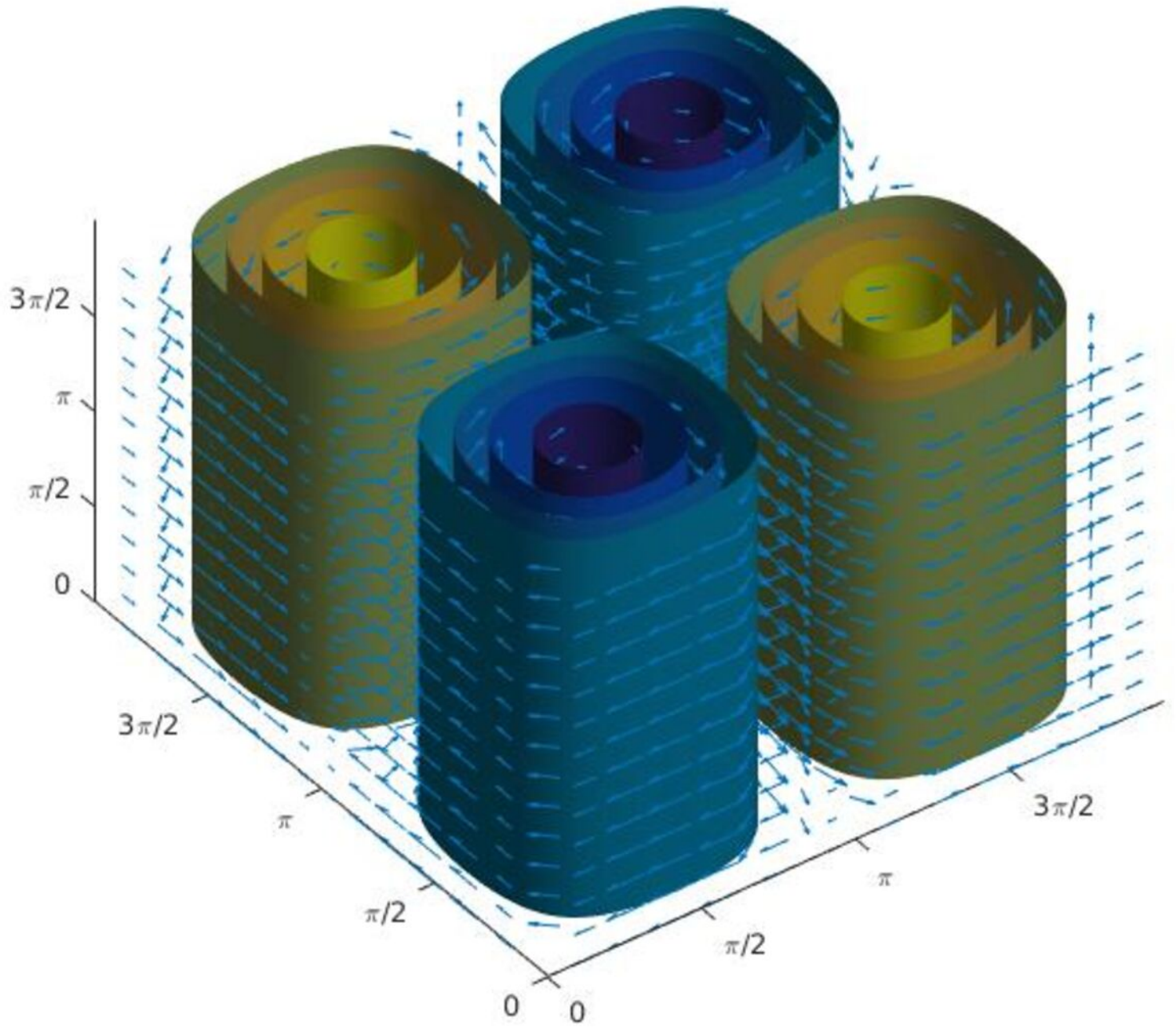

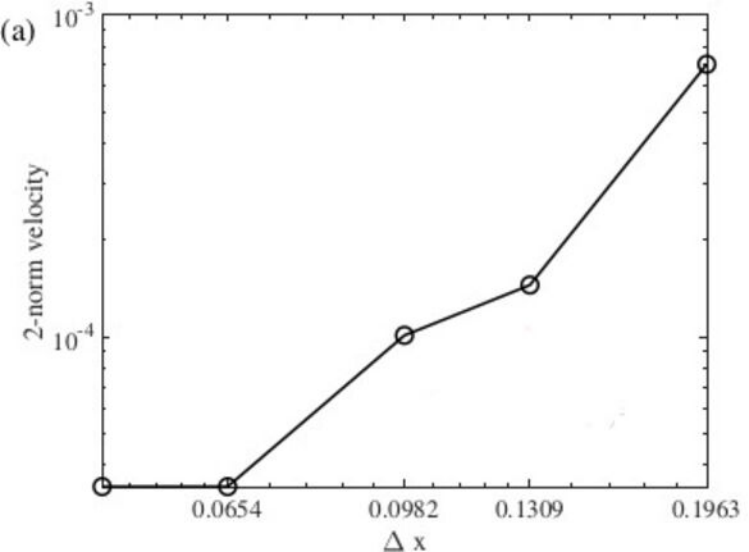

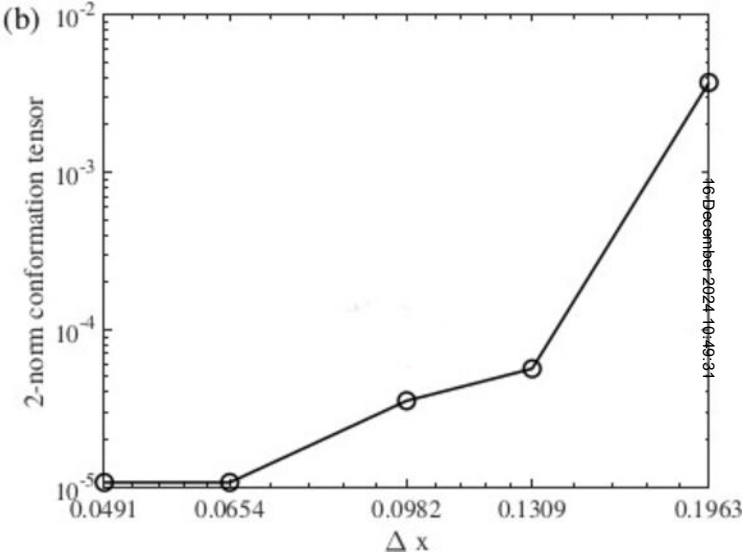

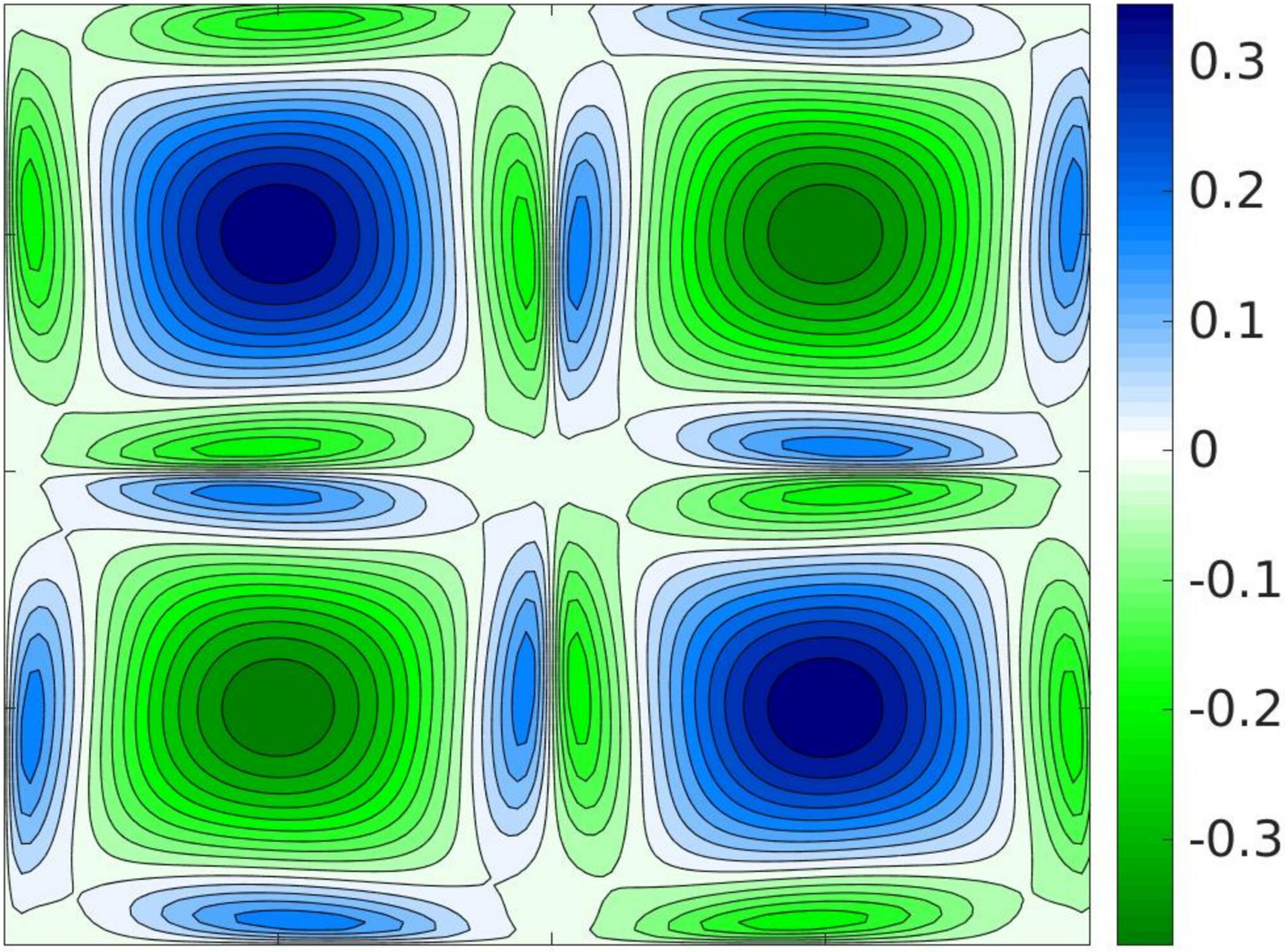

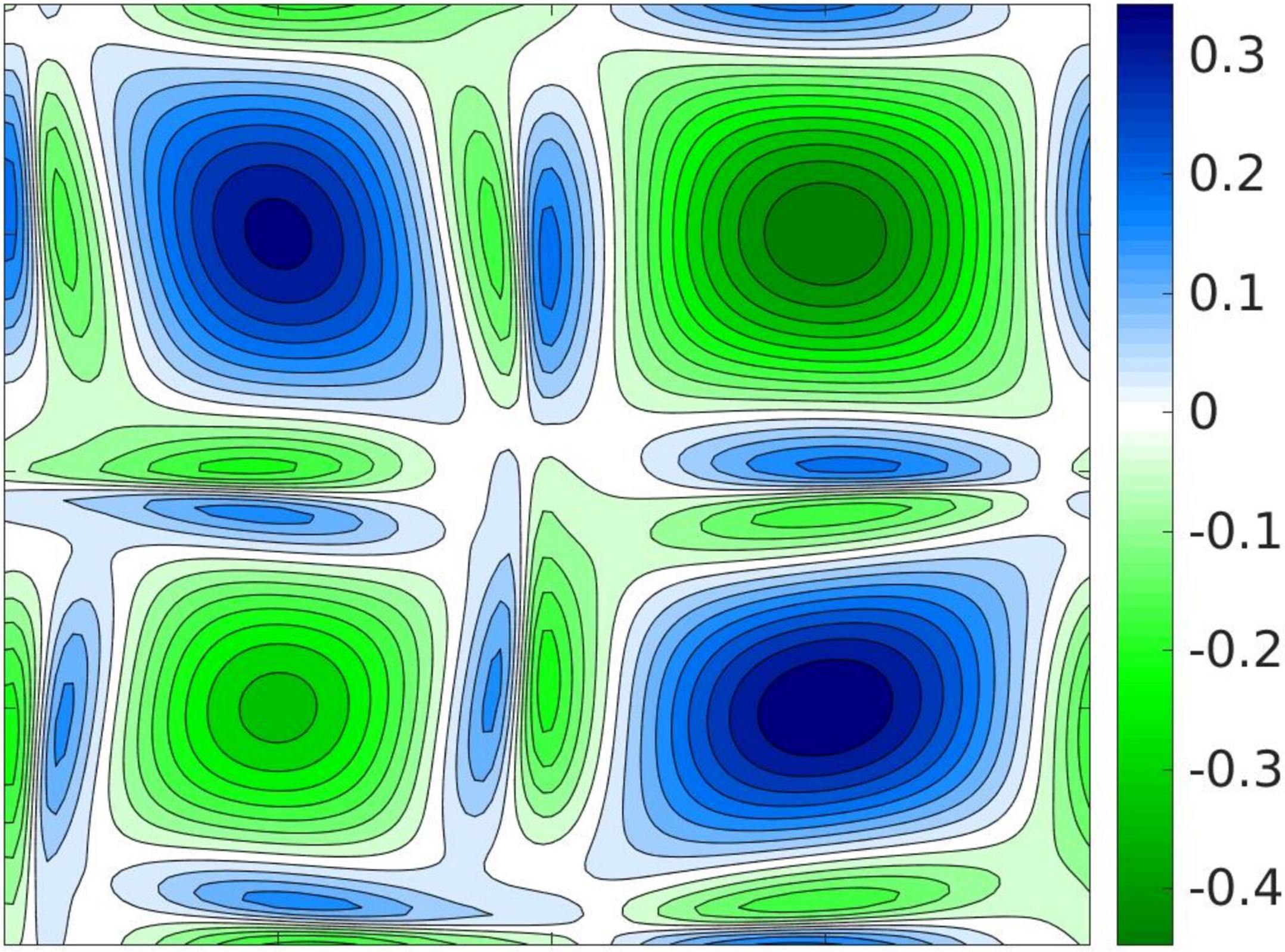

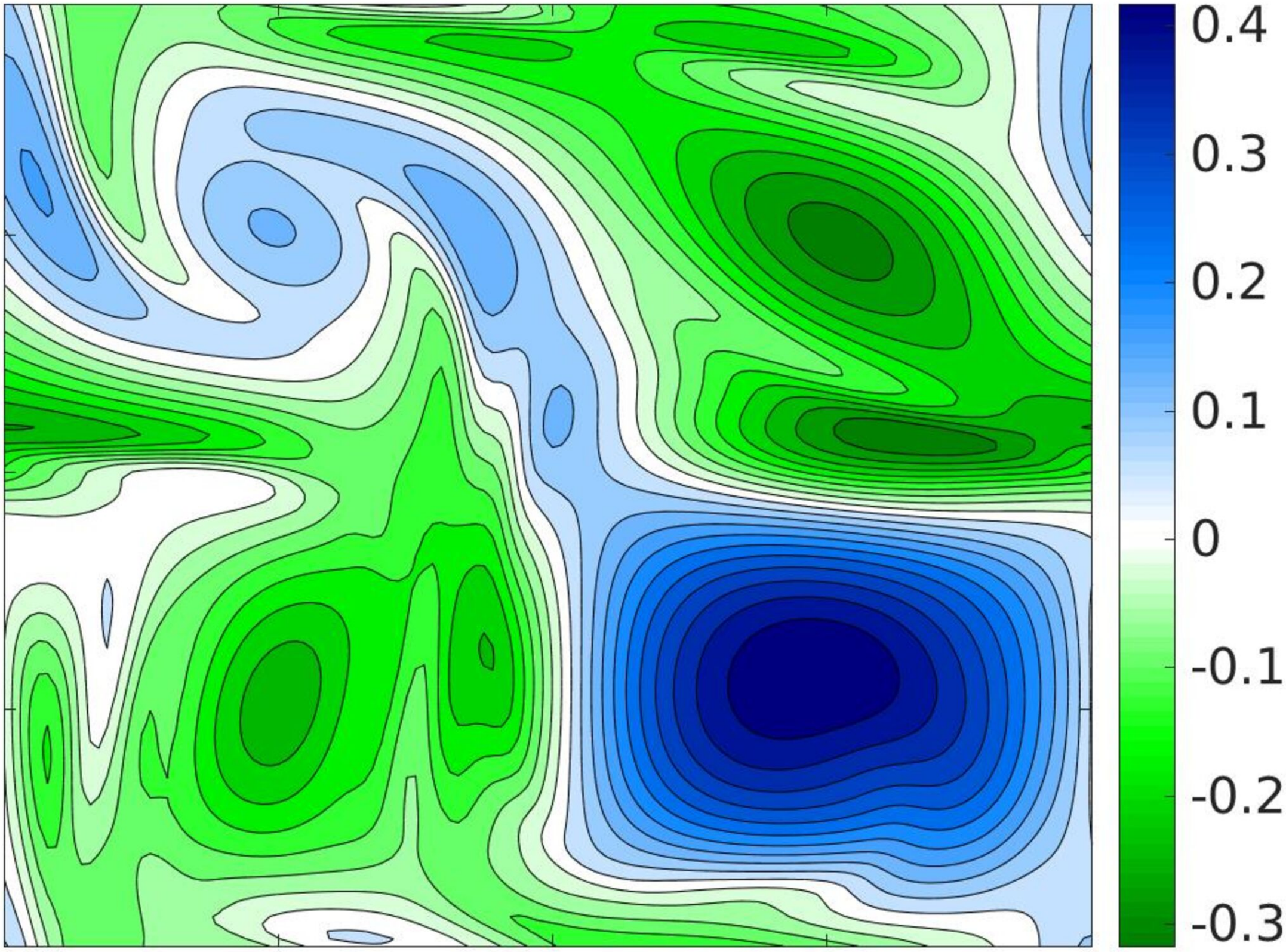

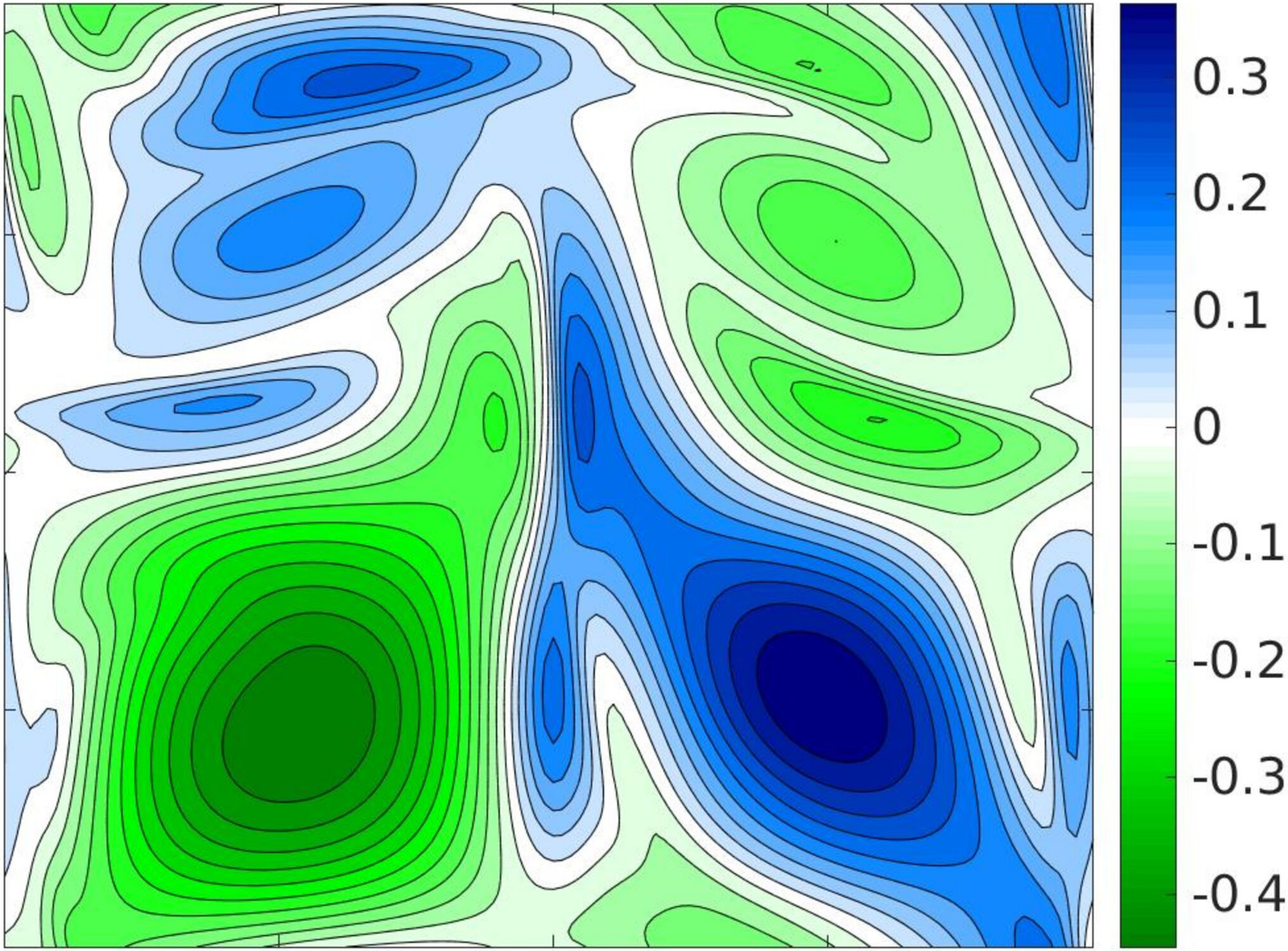

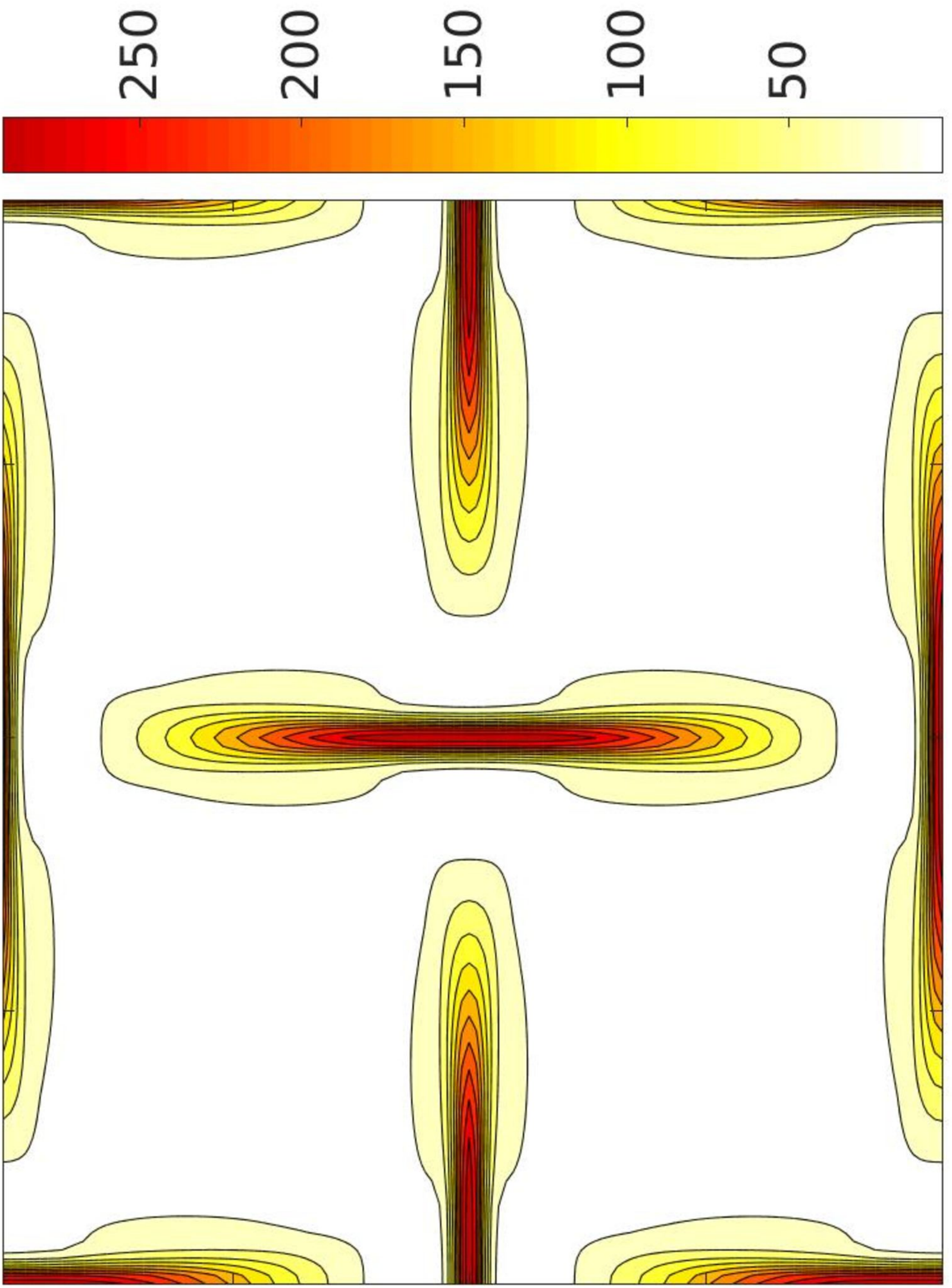
250
200
150
100
50

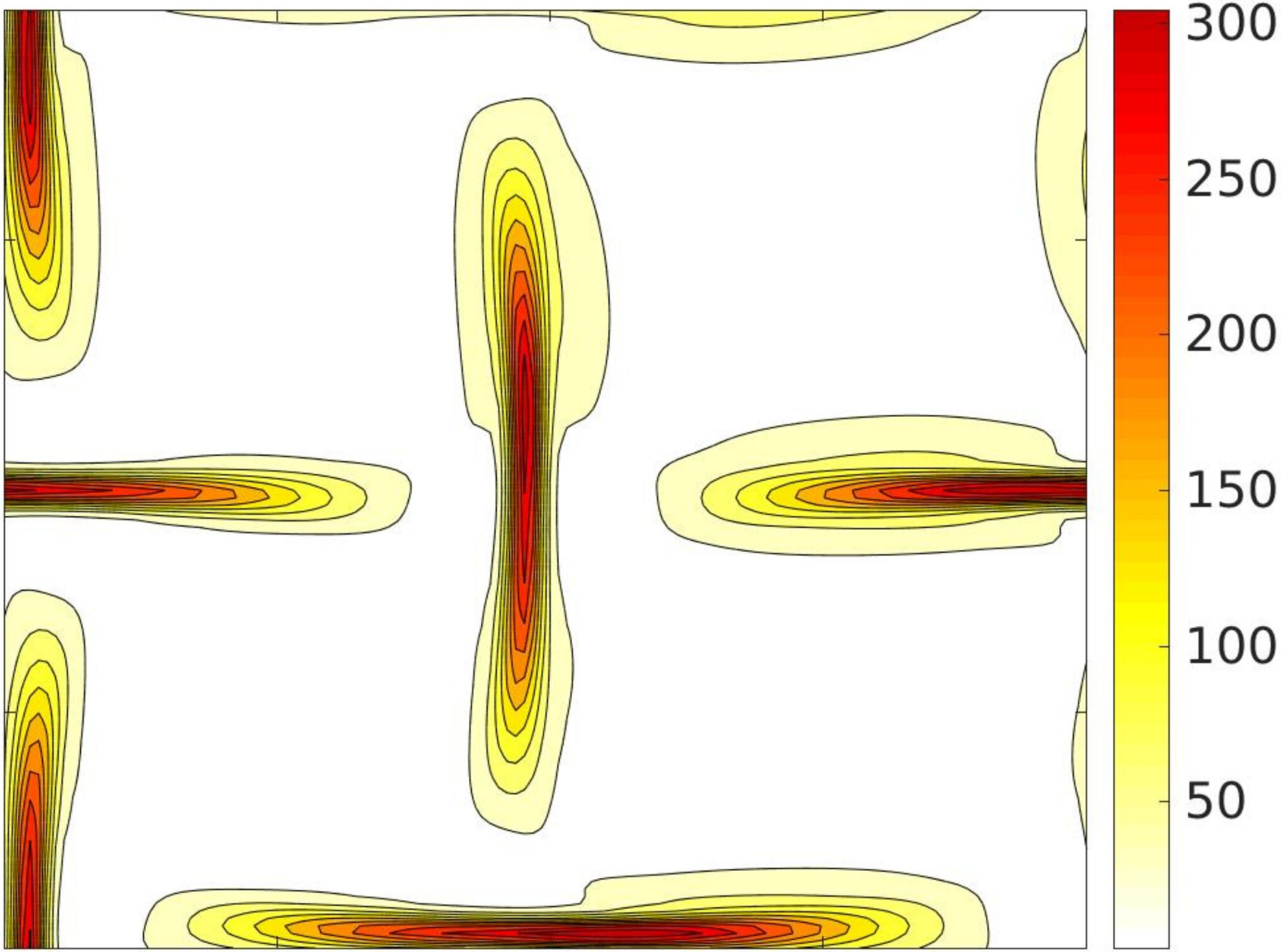

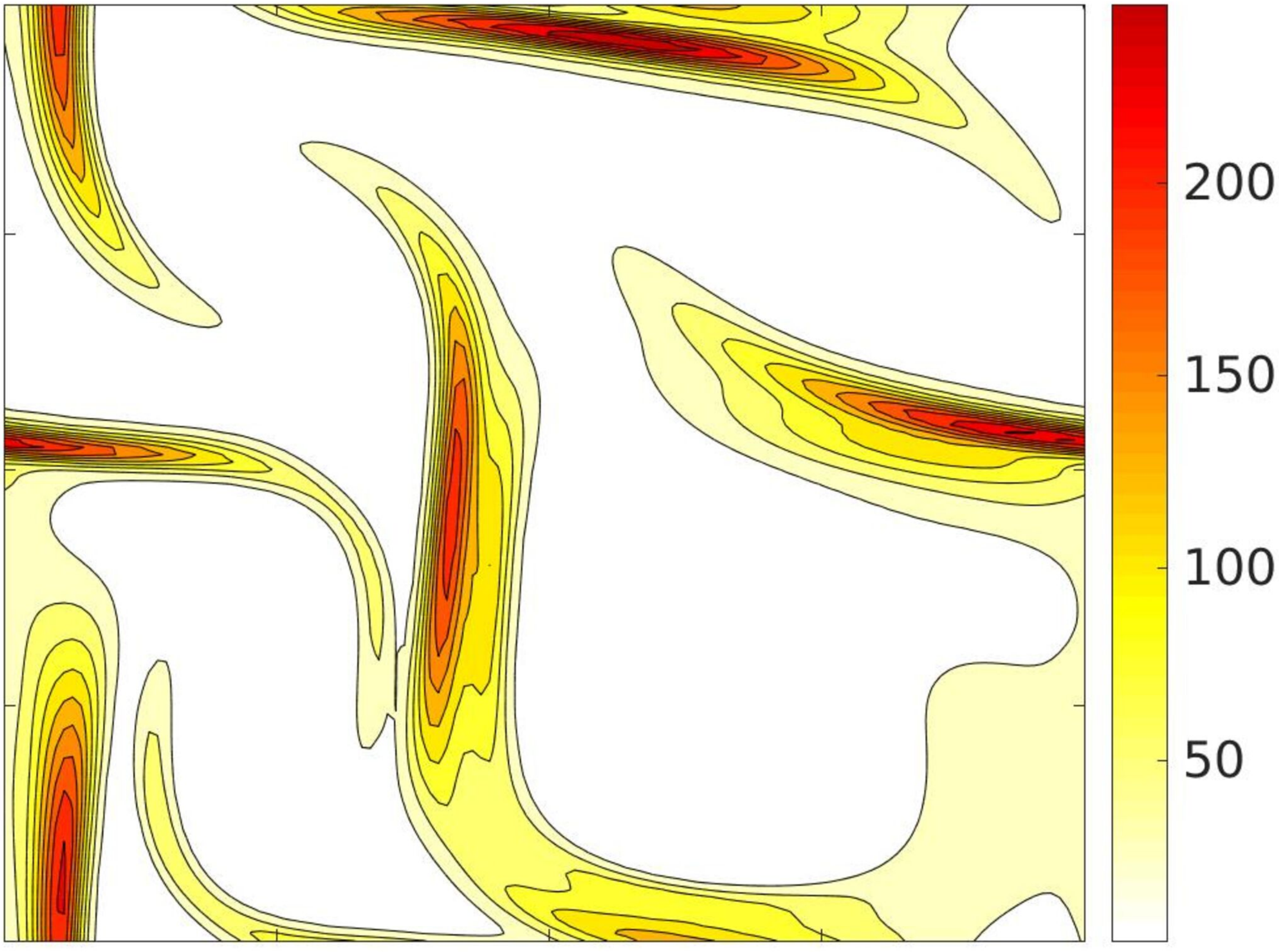

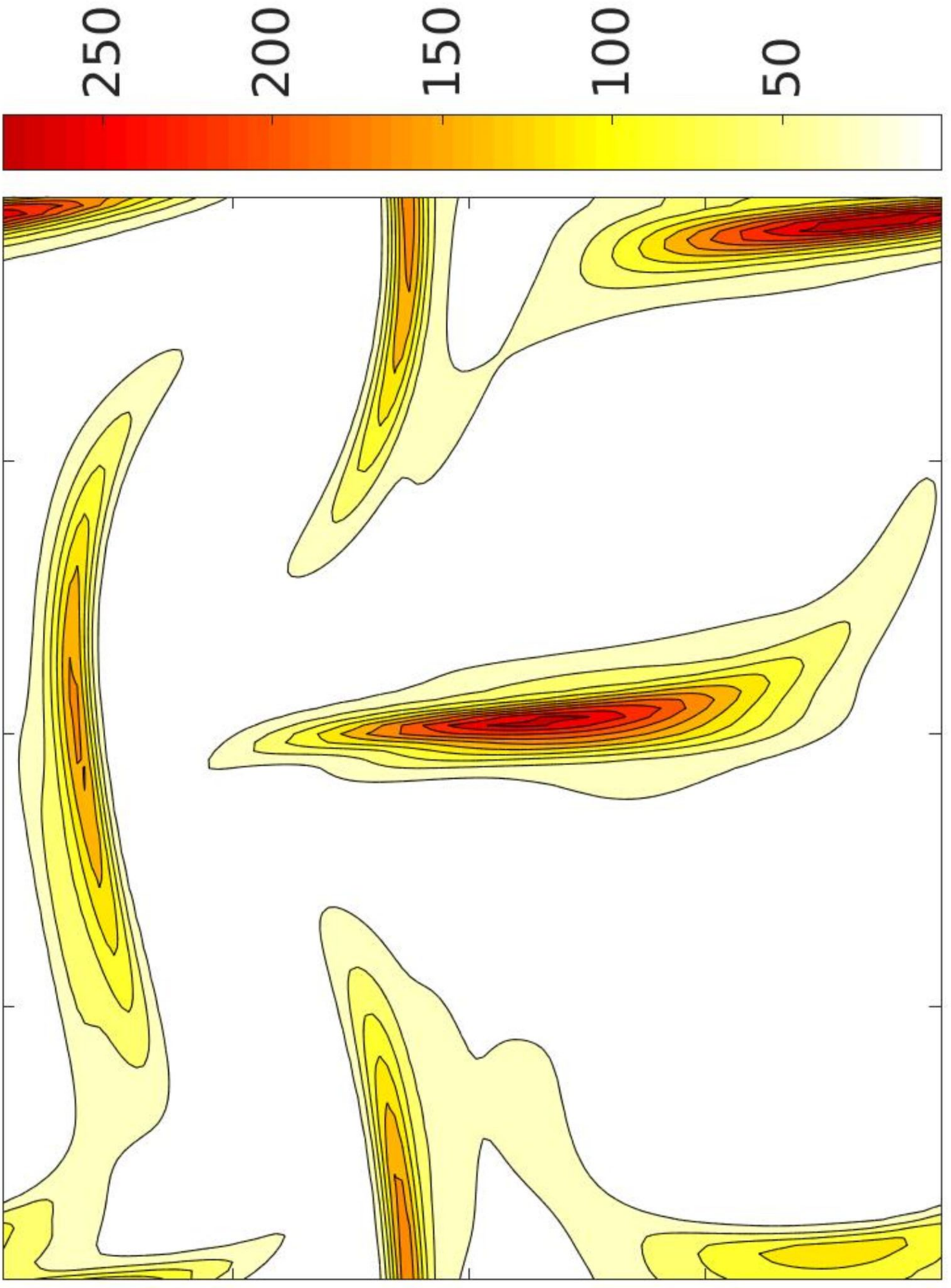
250
200
150
100
50

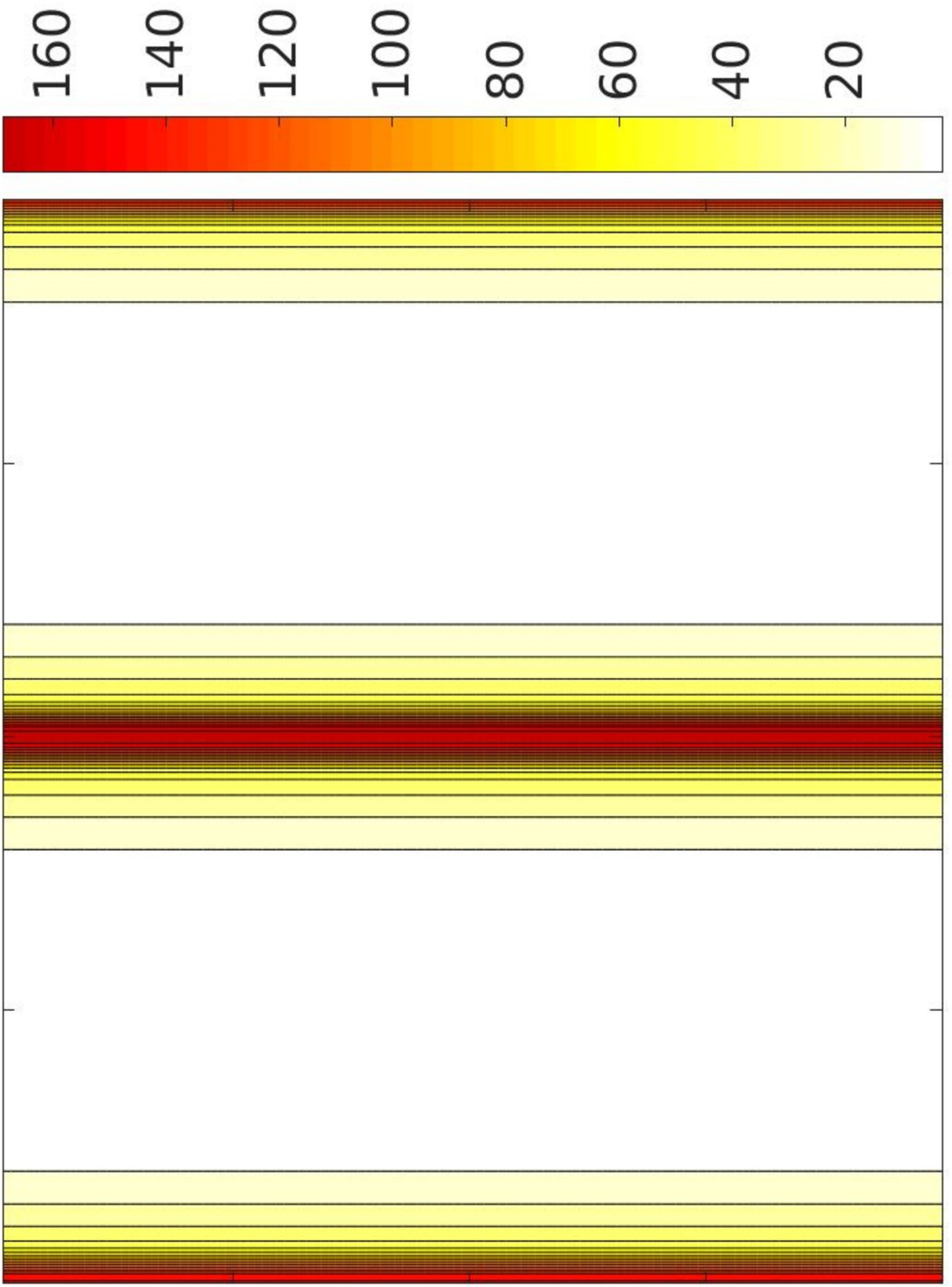
160
140
120
100
80
60
40
20

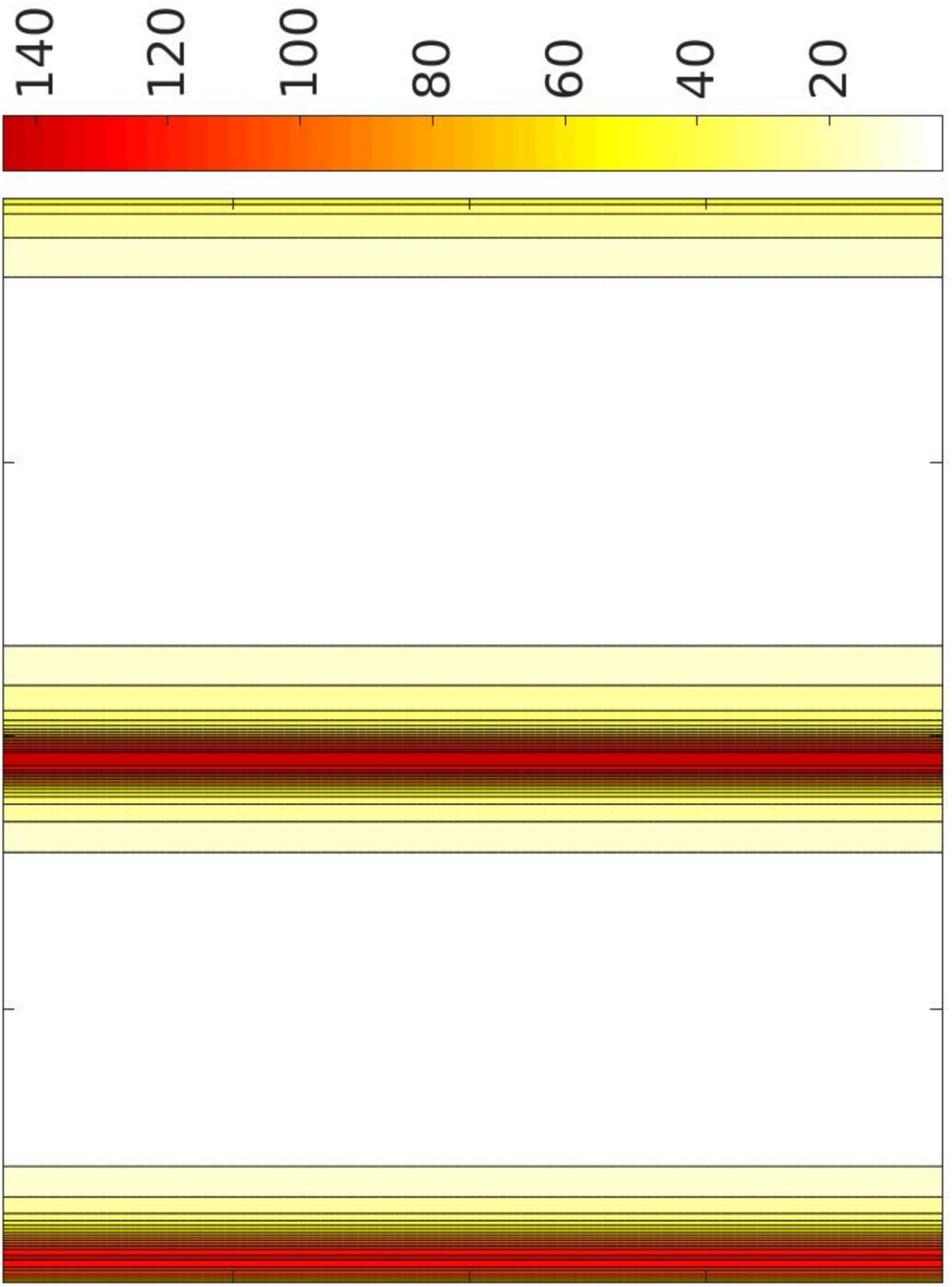
140
120
100
80
60
40
20

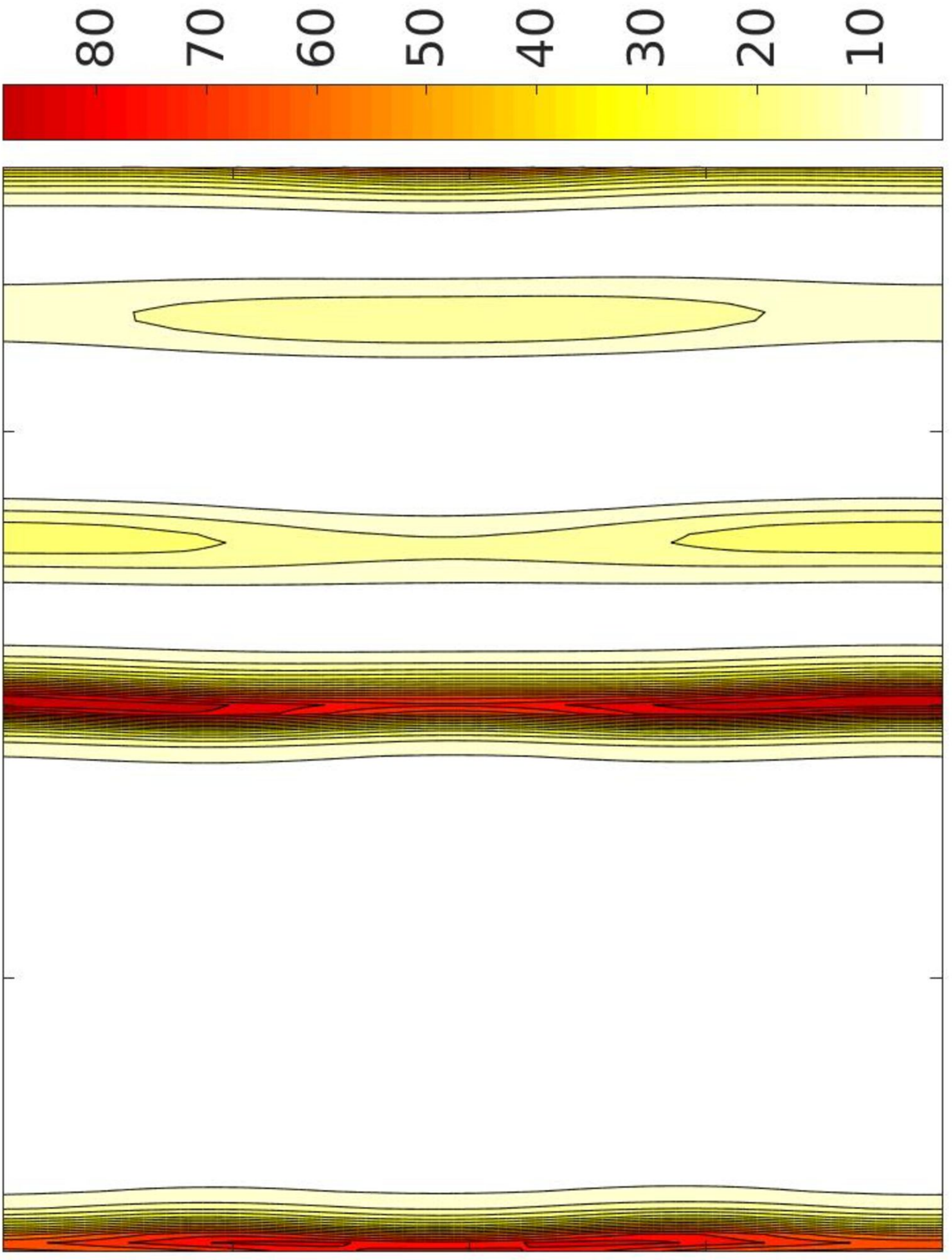
80
70
60
50
40
30
20
10

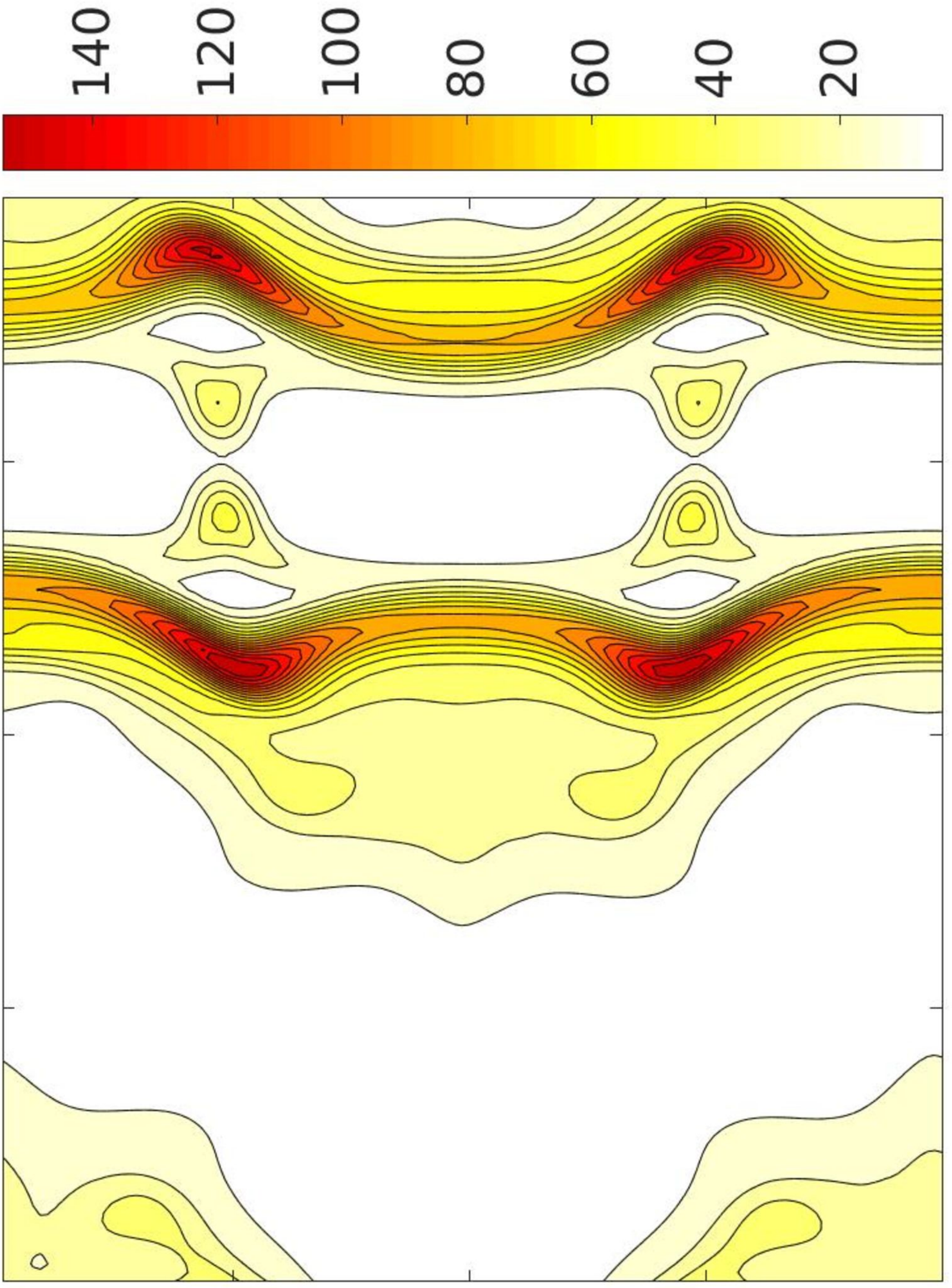
140
120
100
80
60
40
20

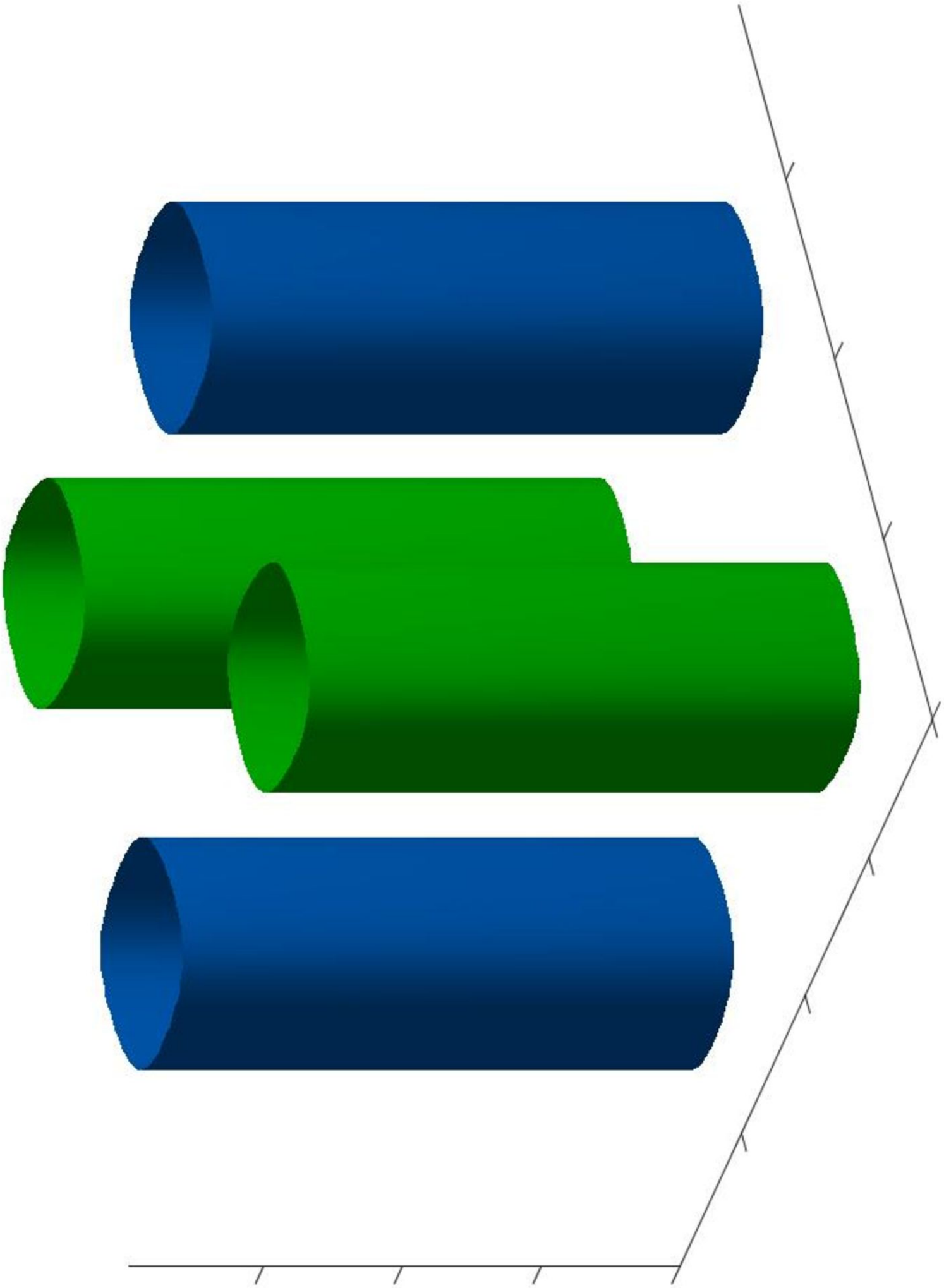

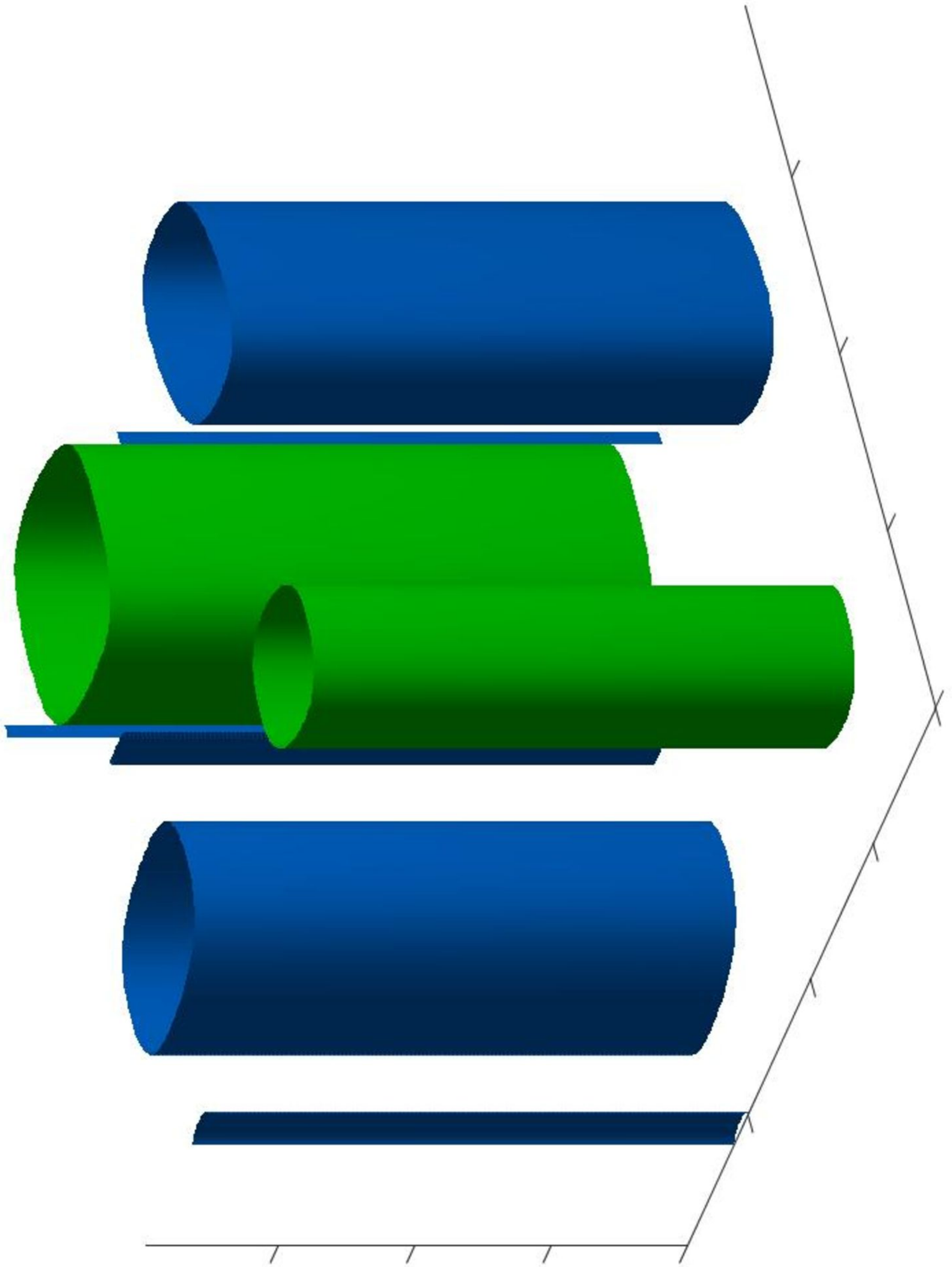

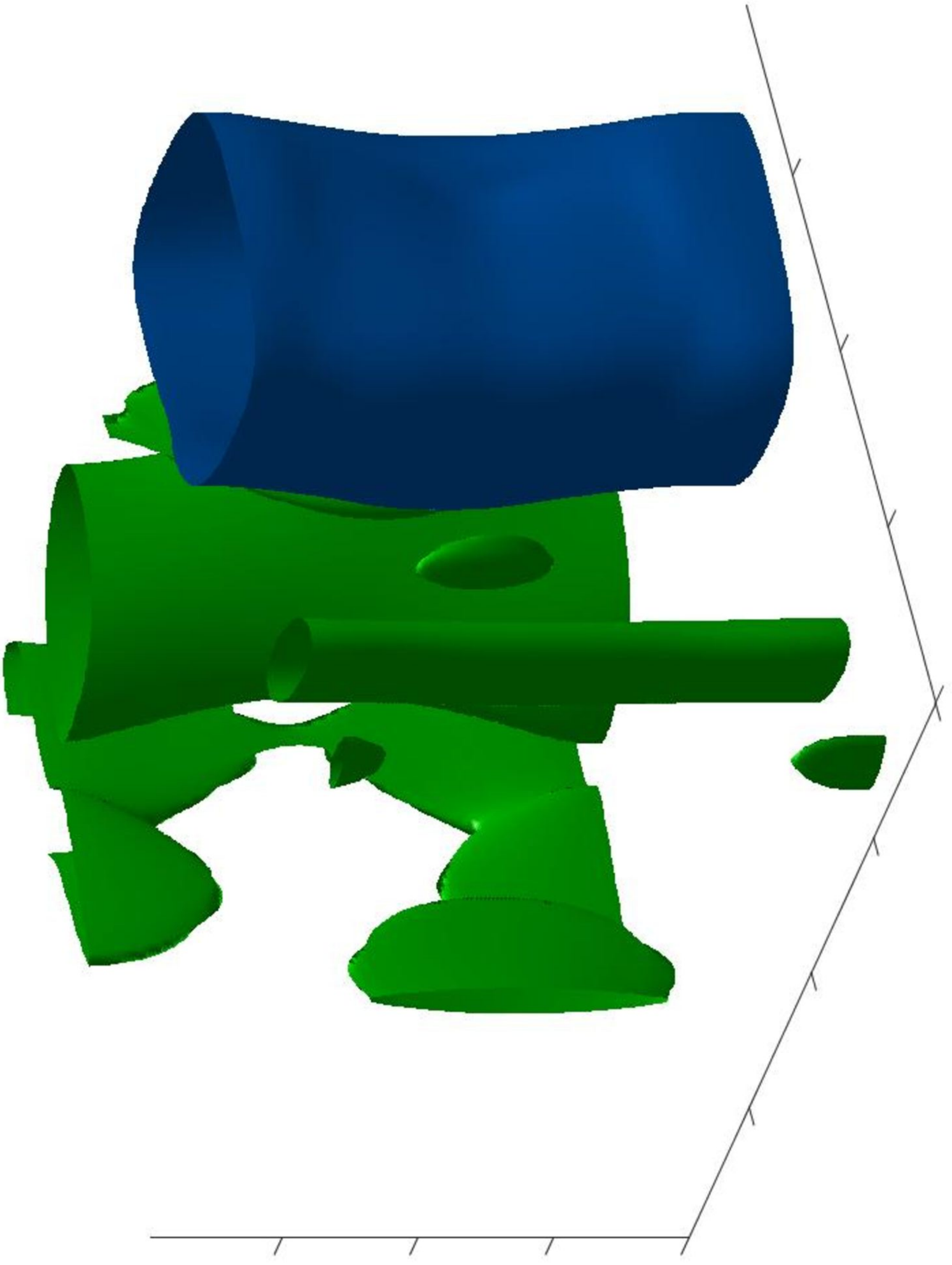

16 December 2024 10:49:31

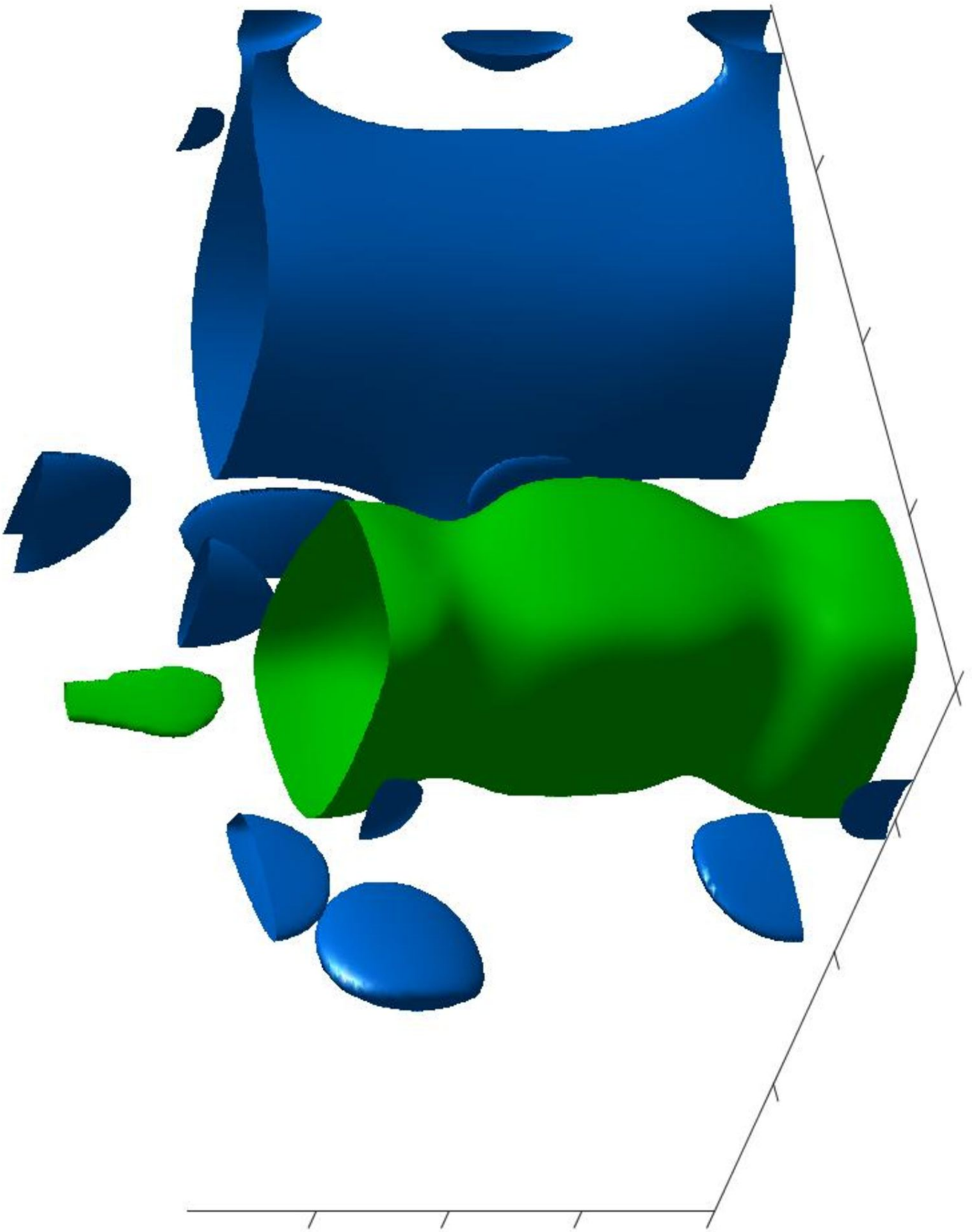

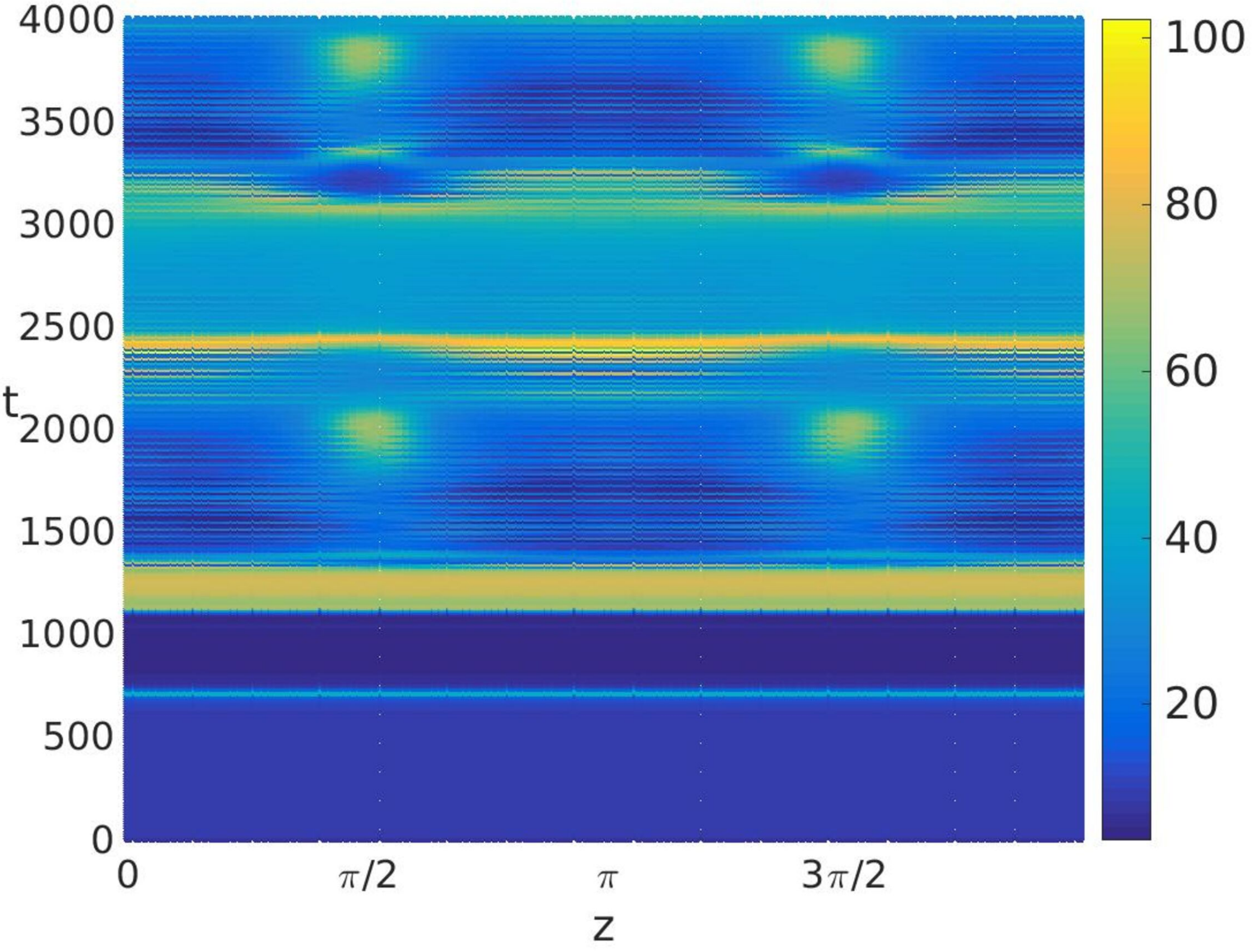

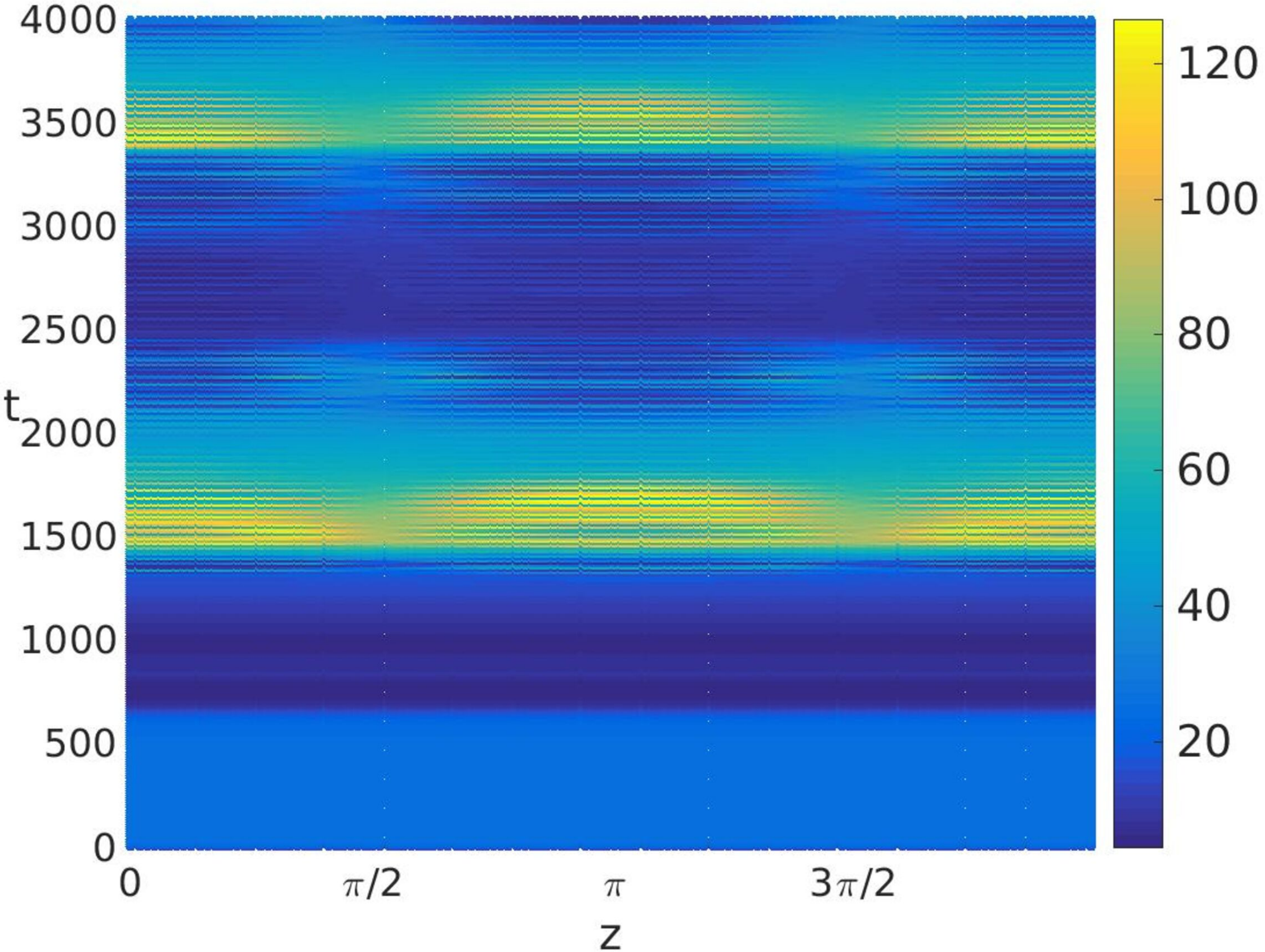

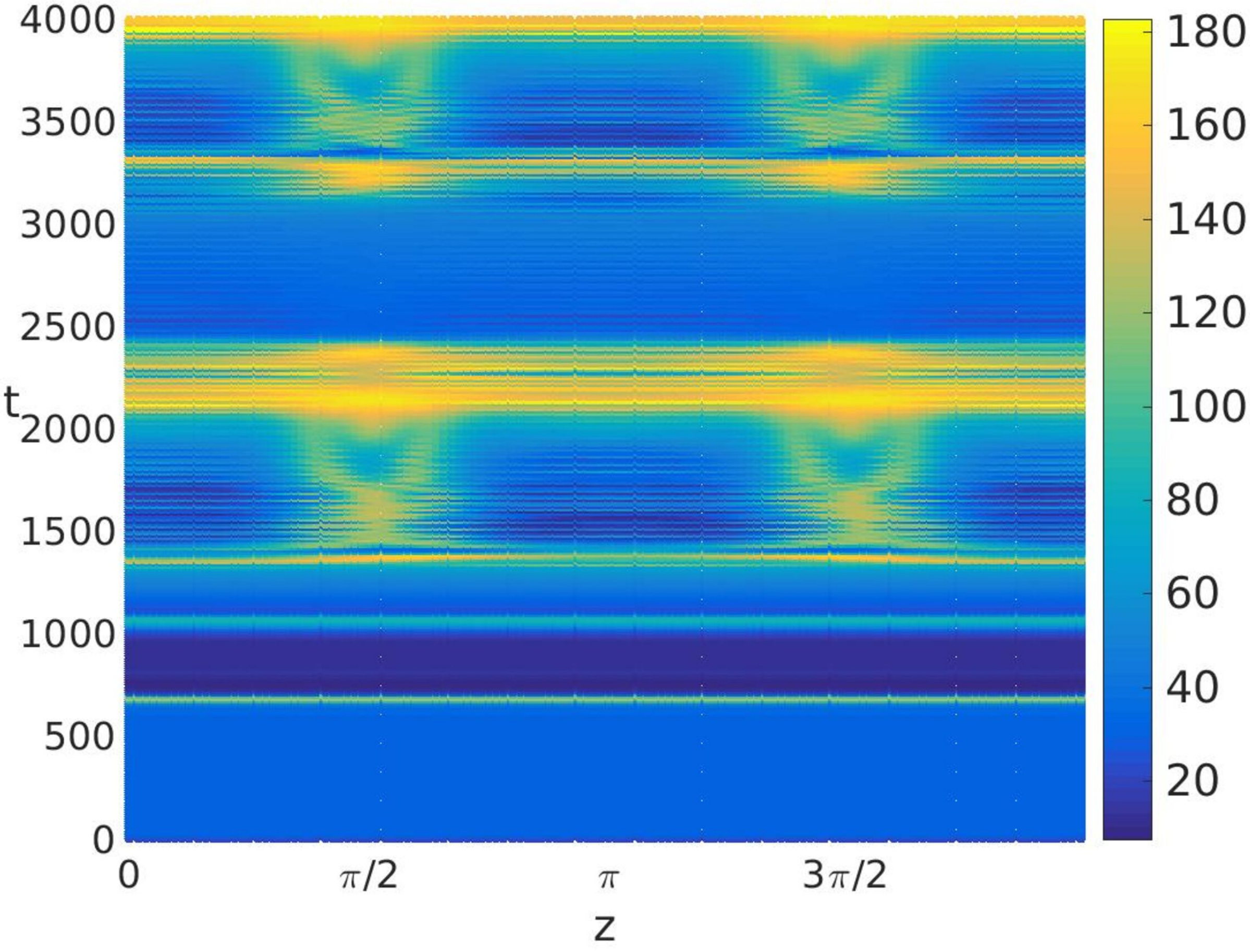

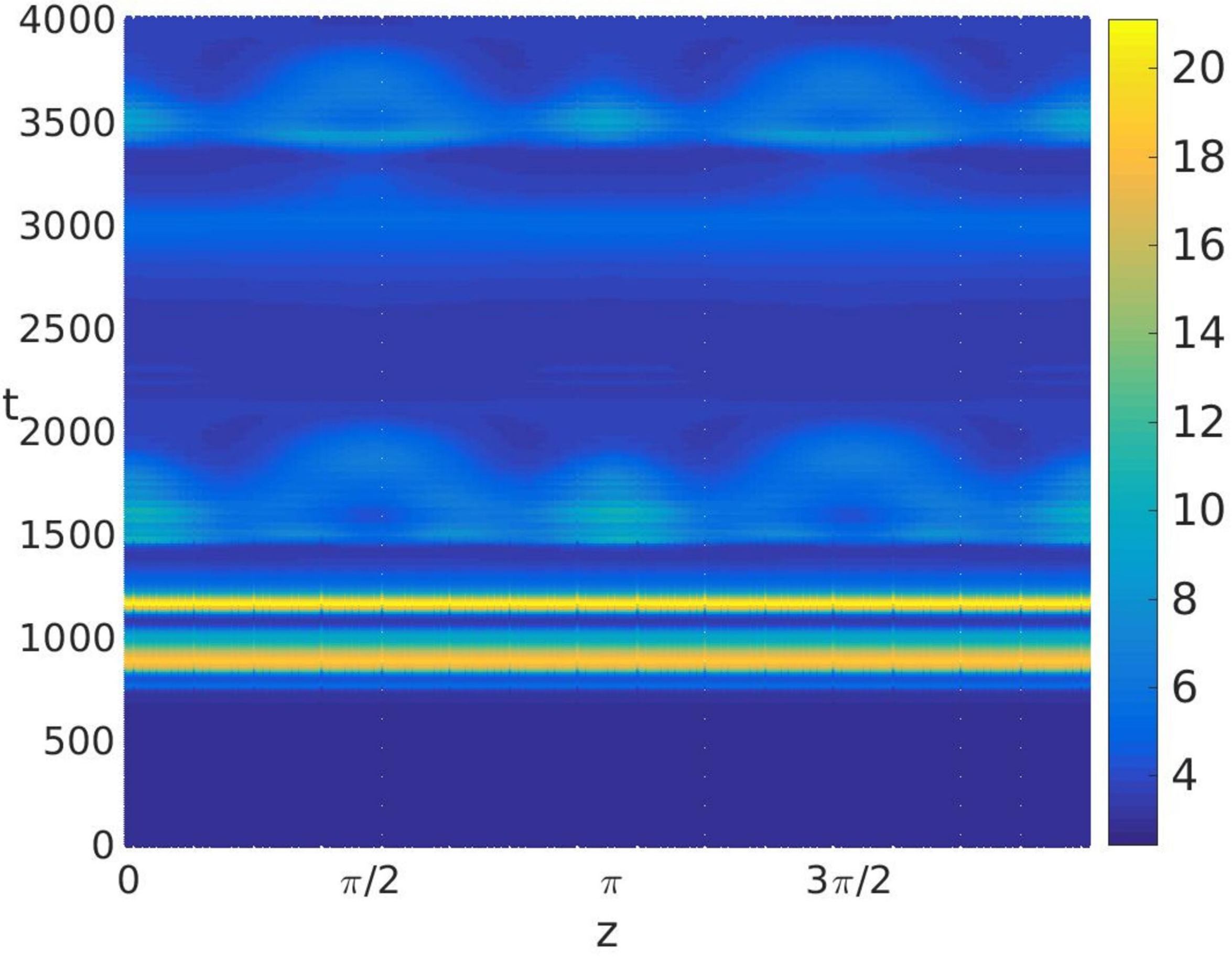

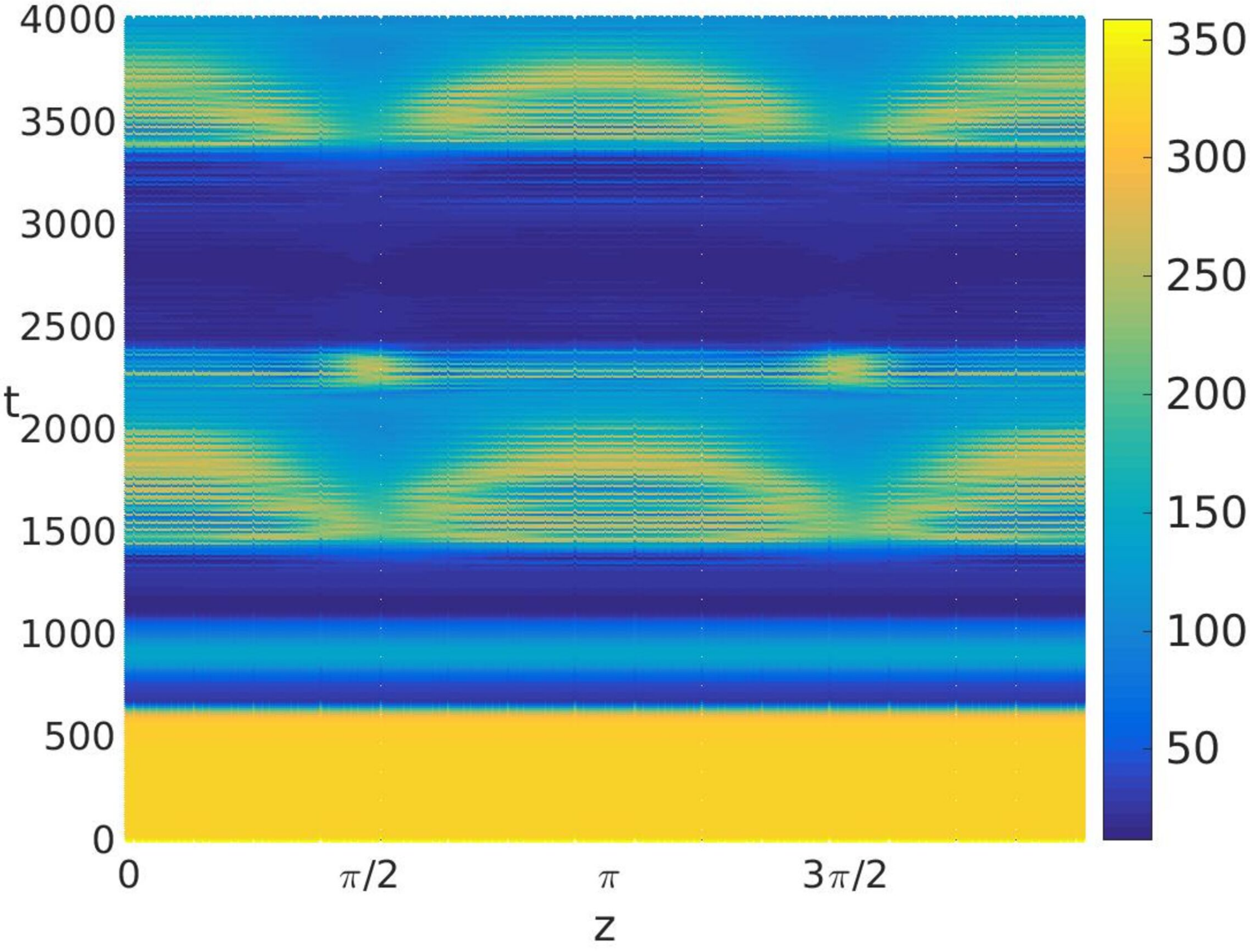

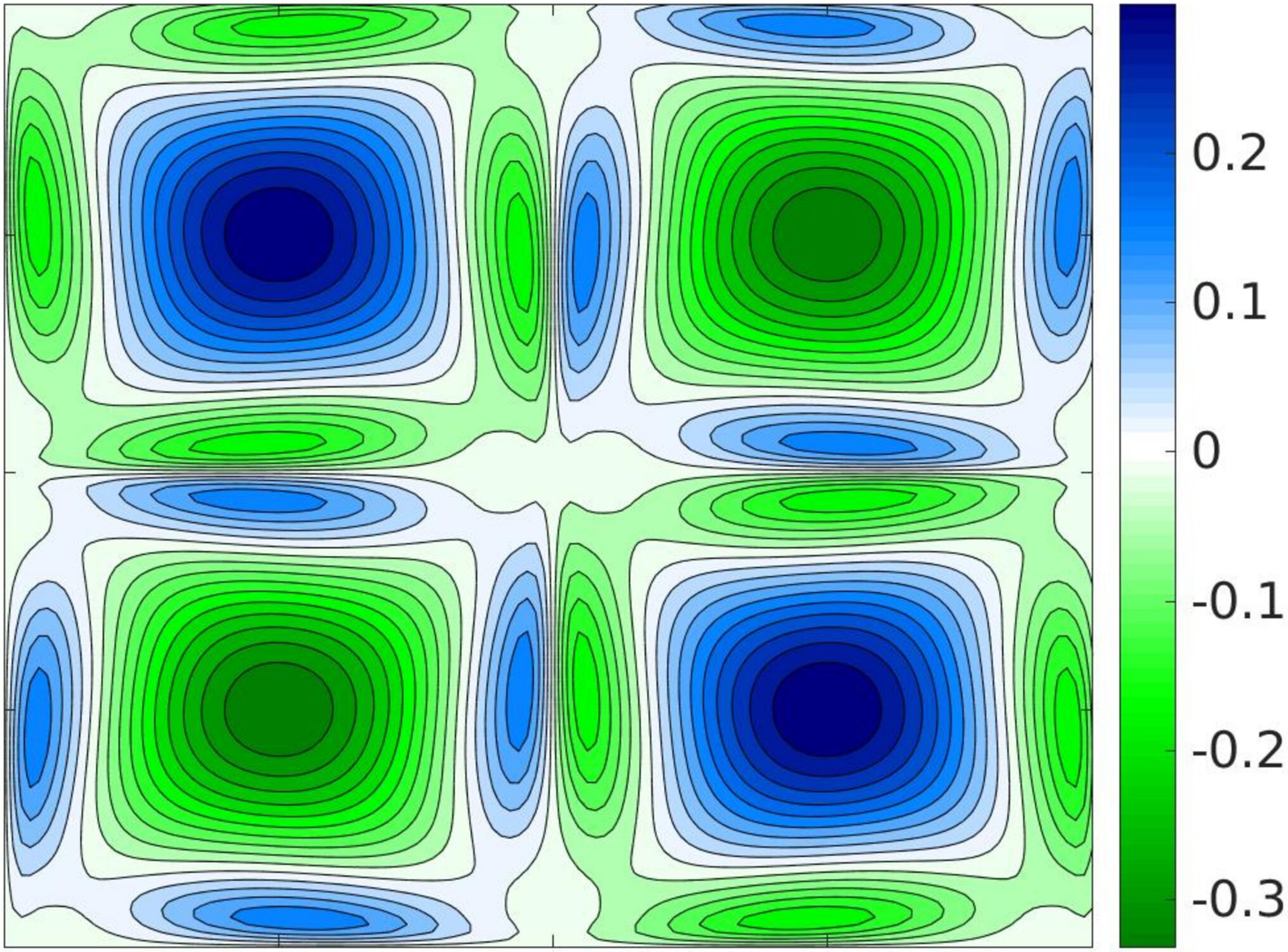

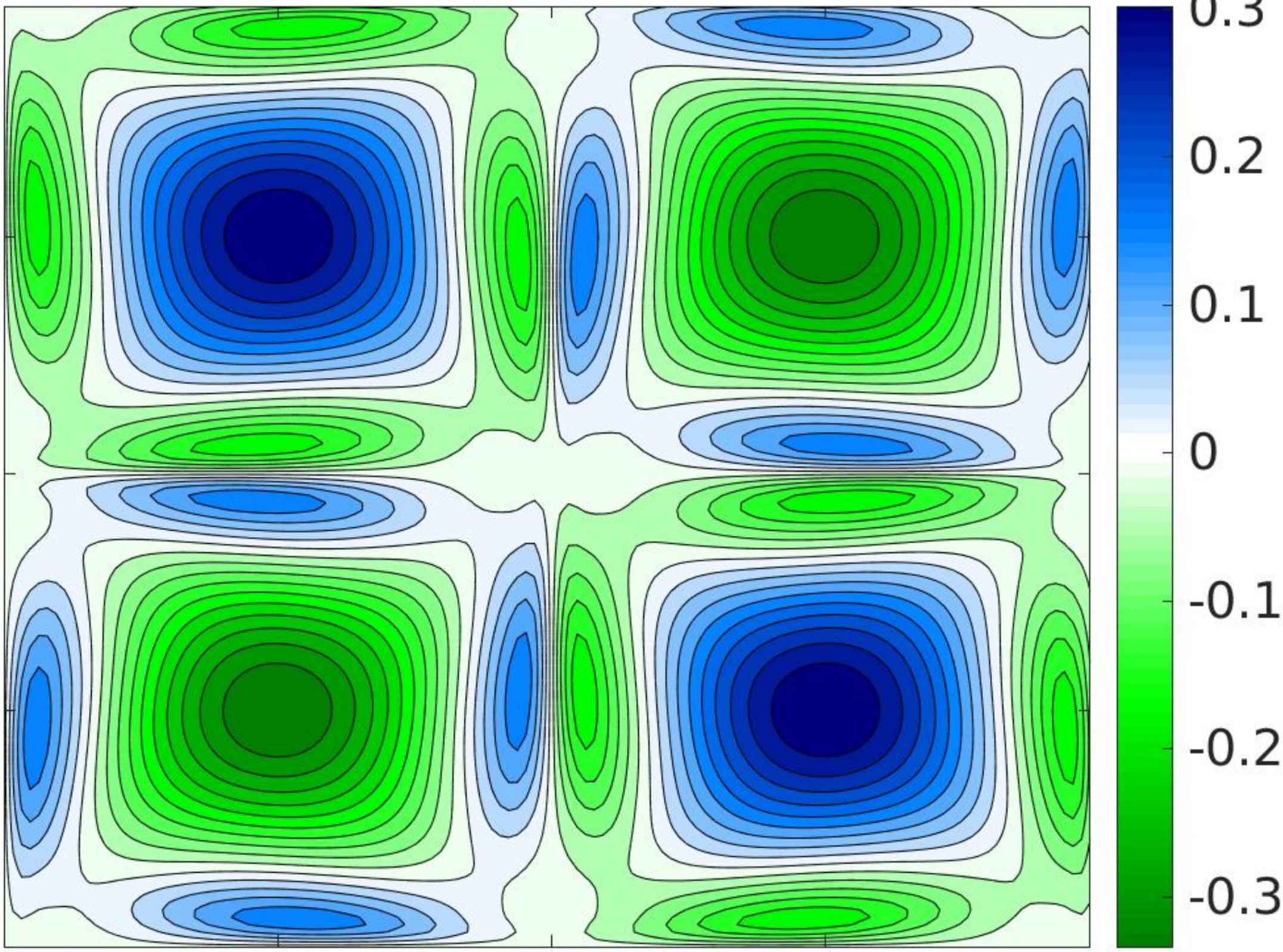

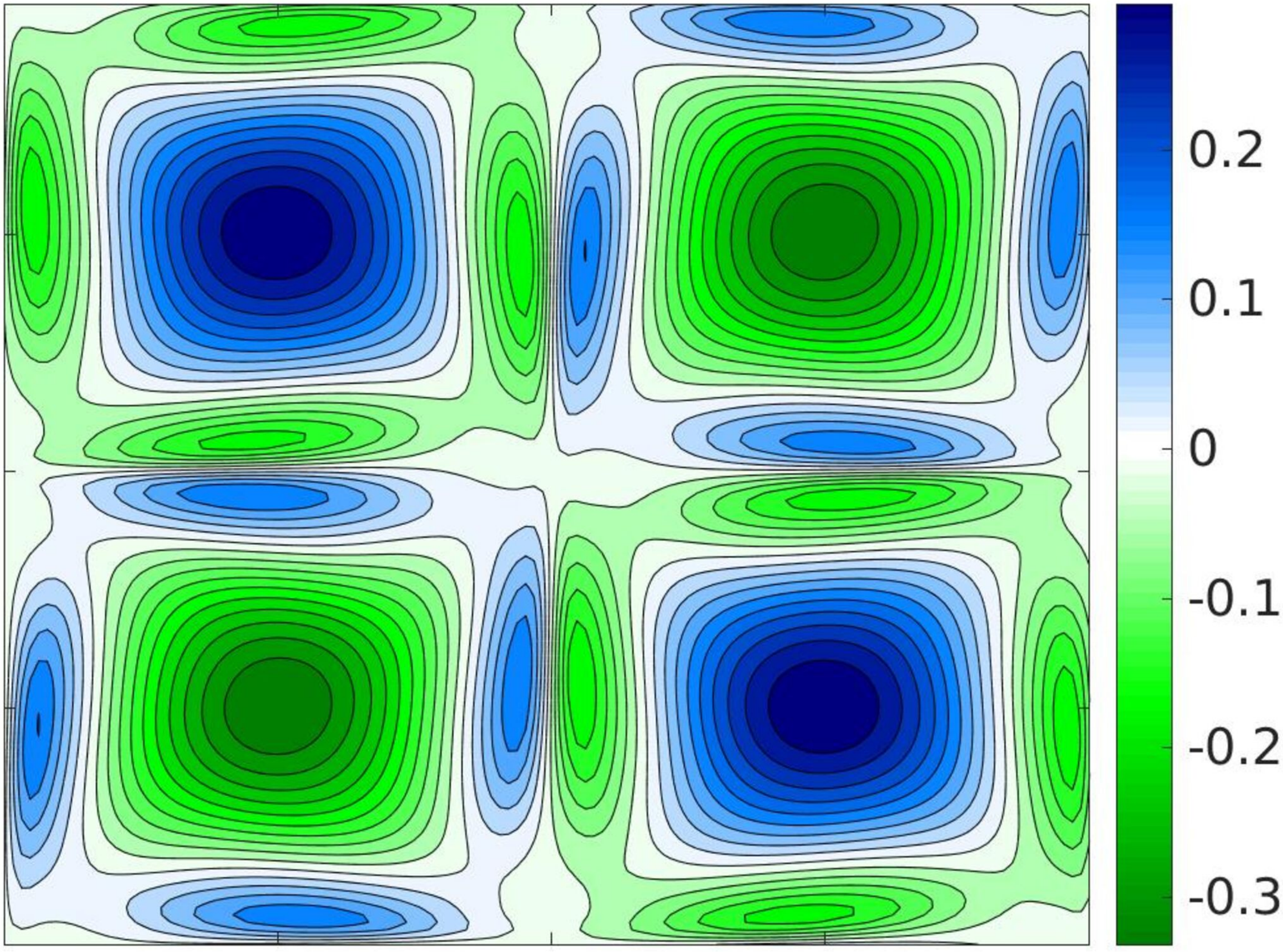

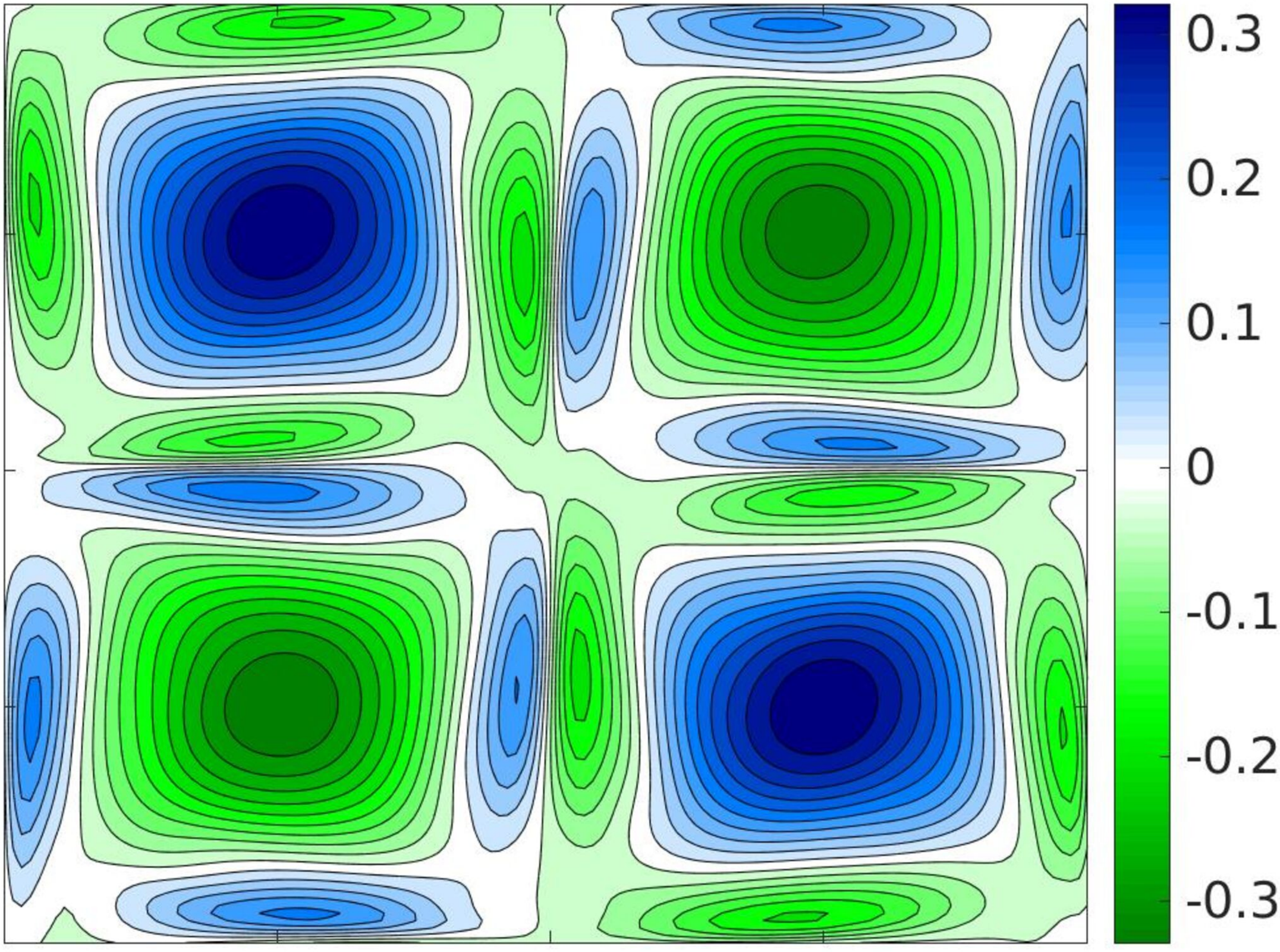

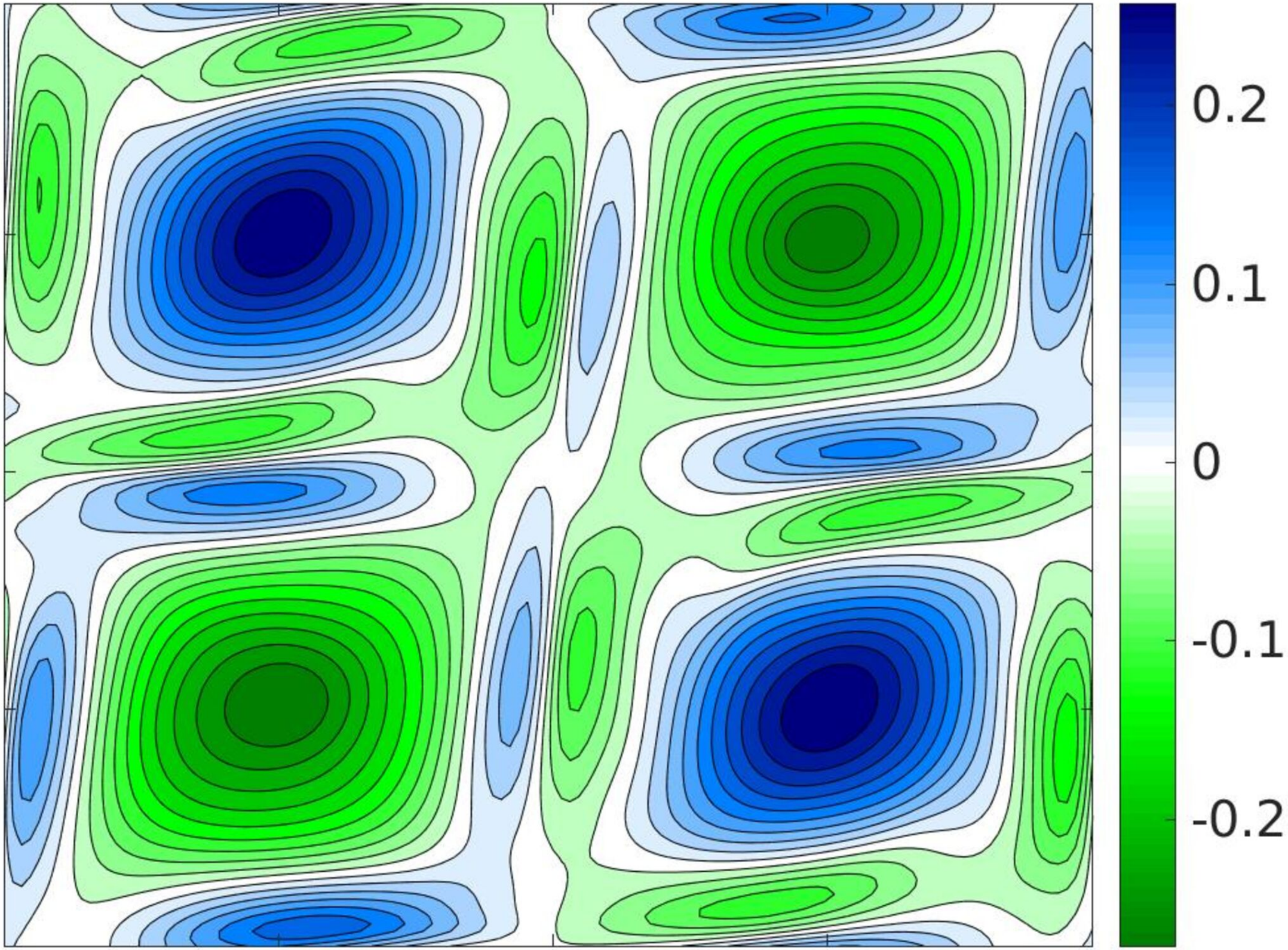

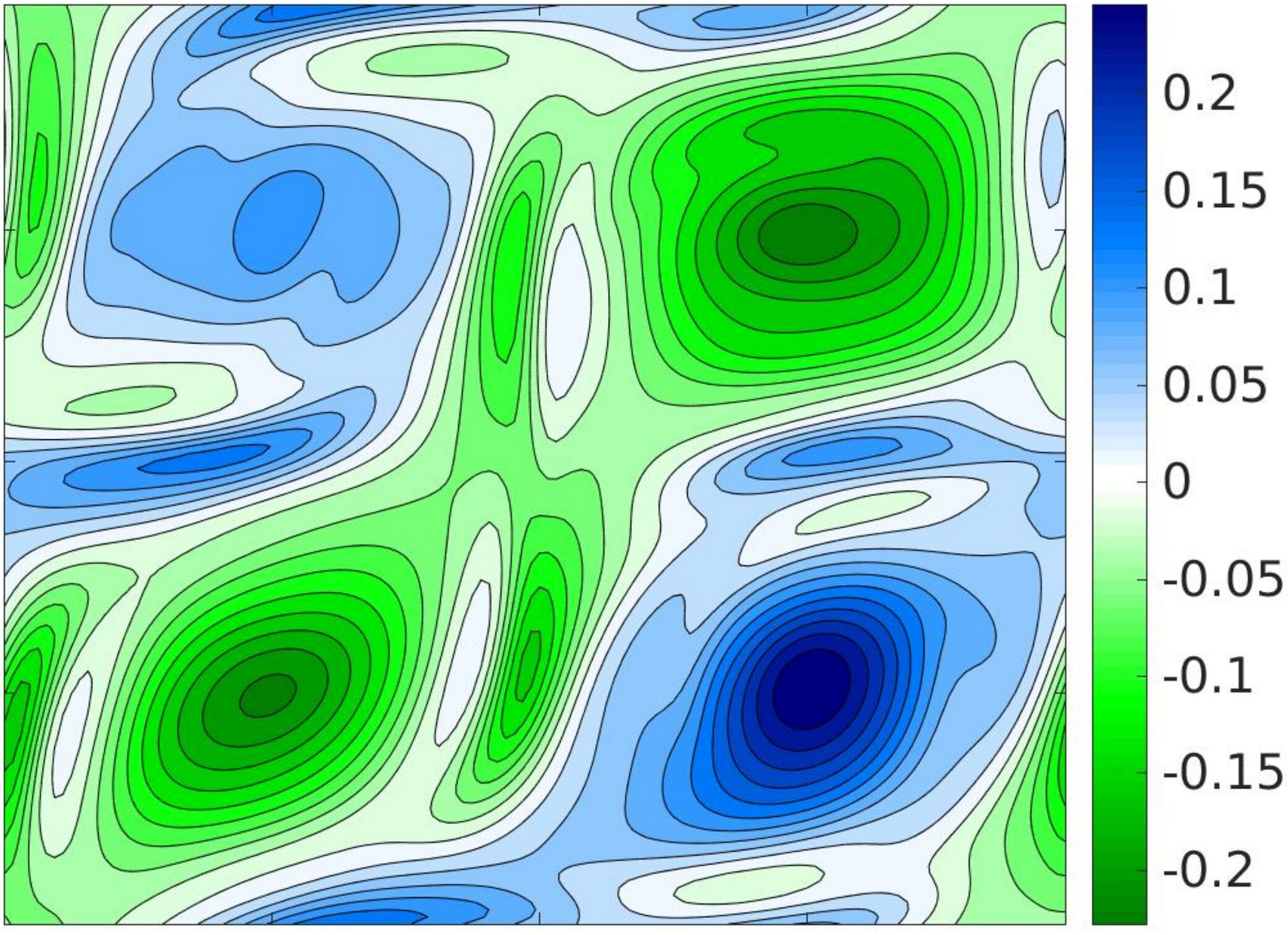

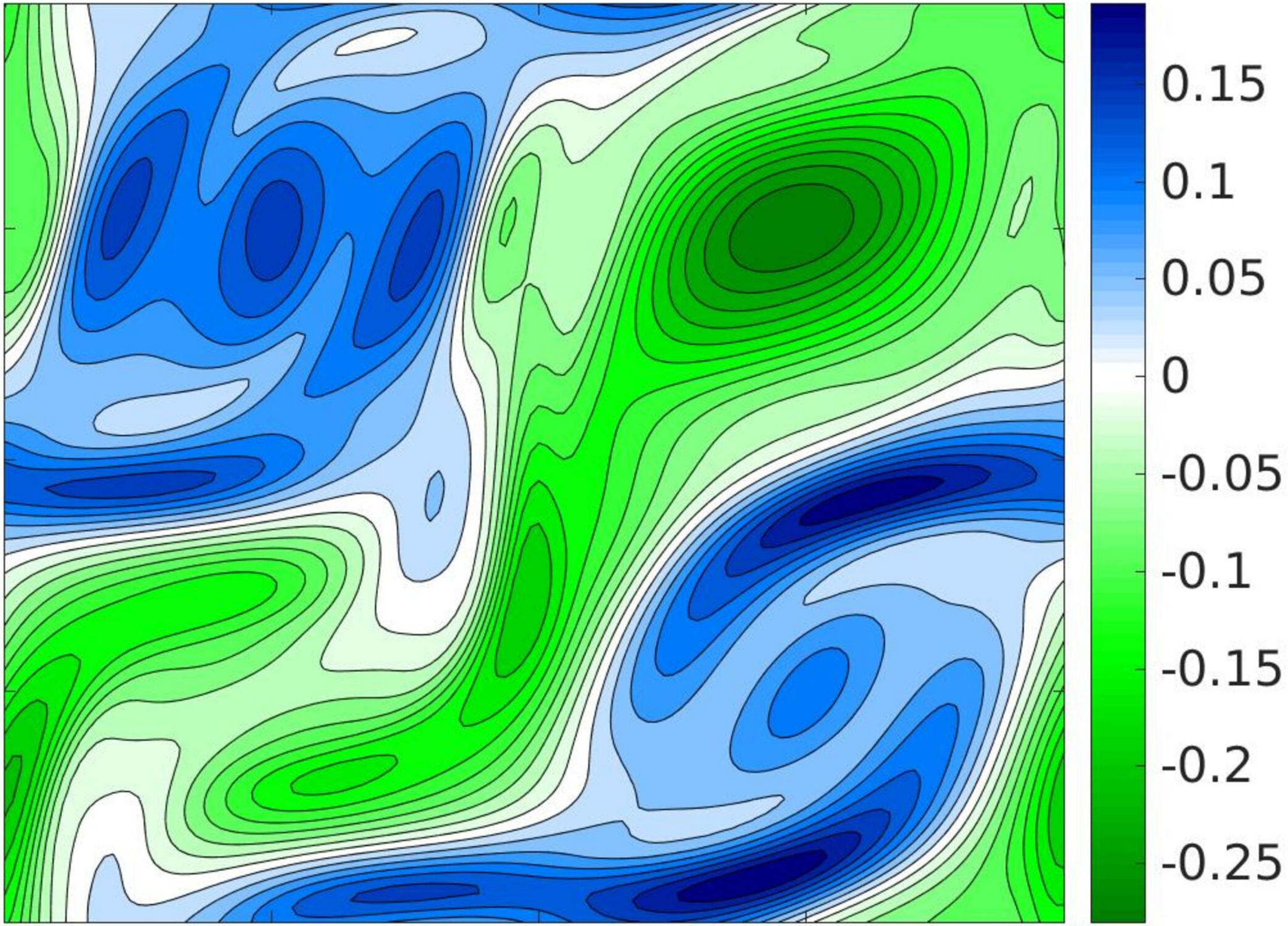

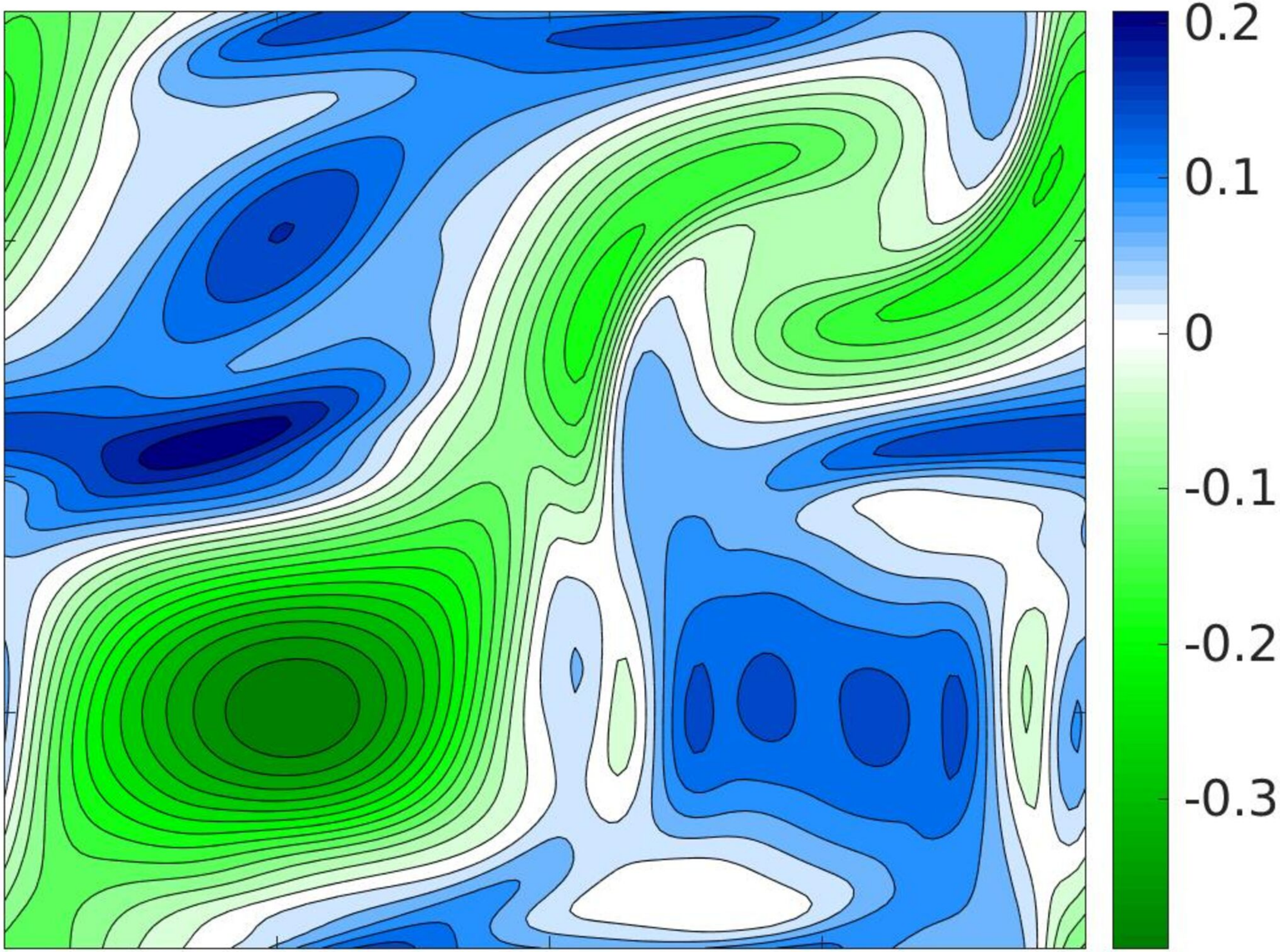

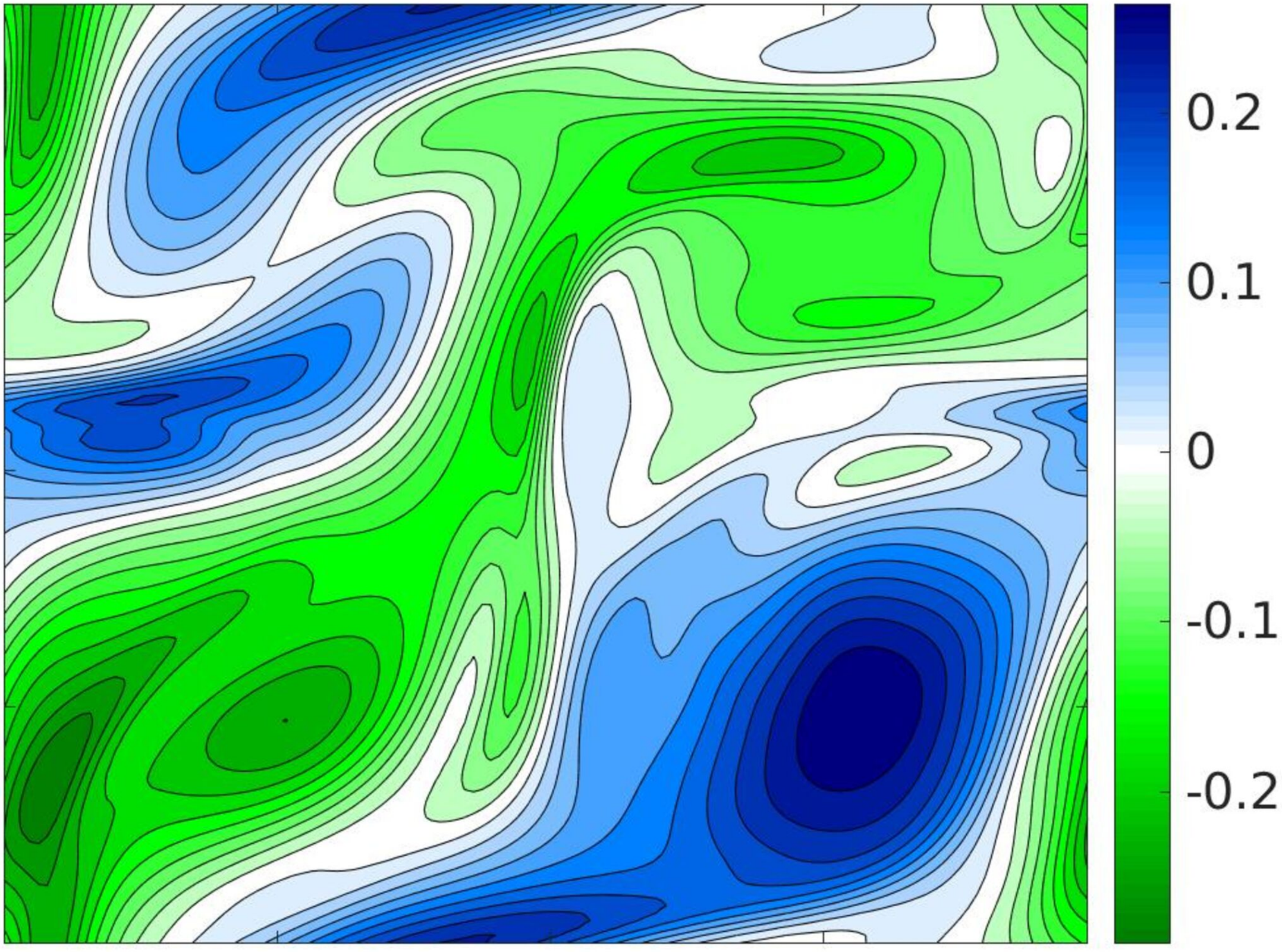

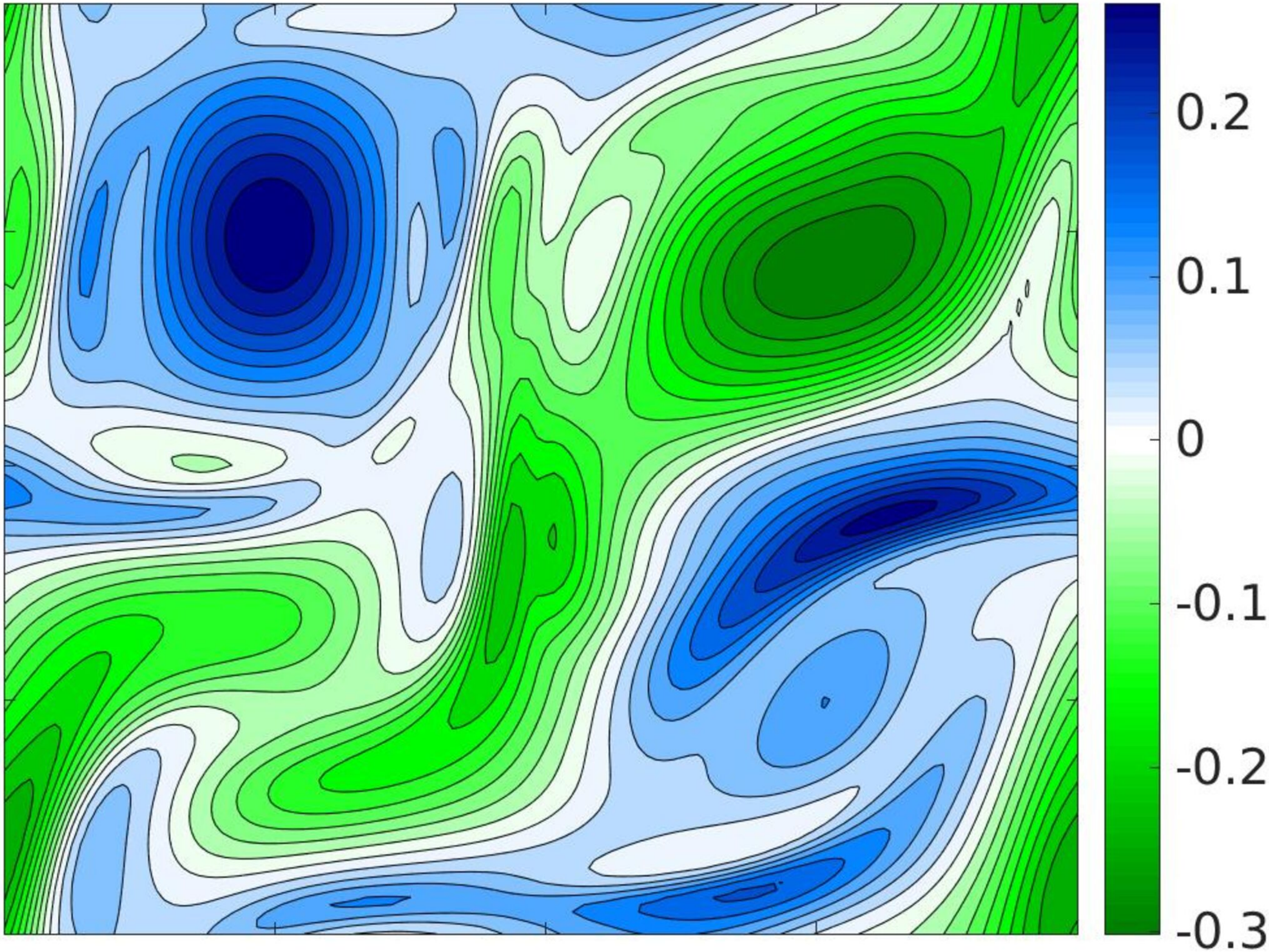

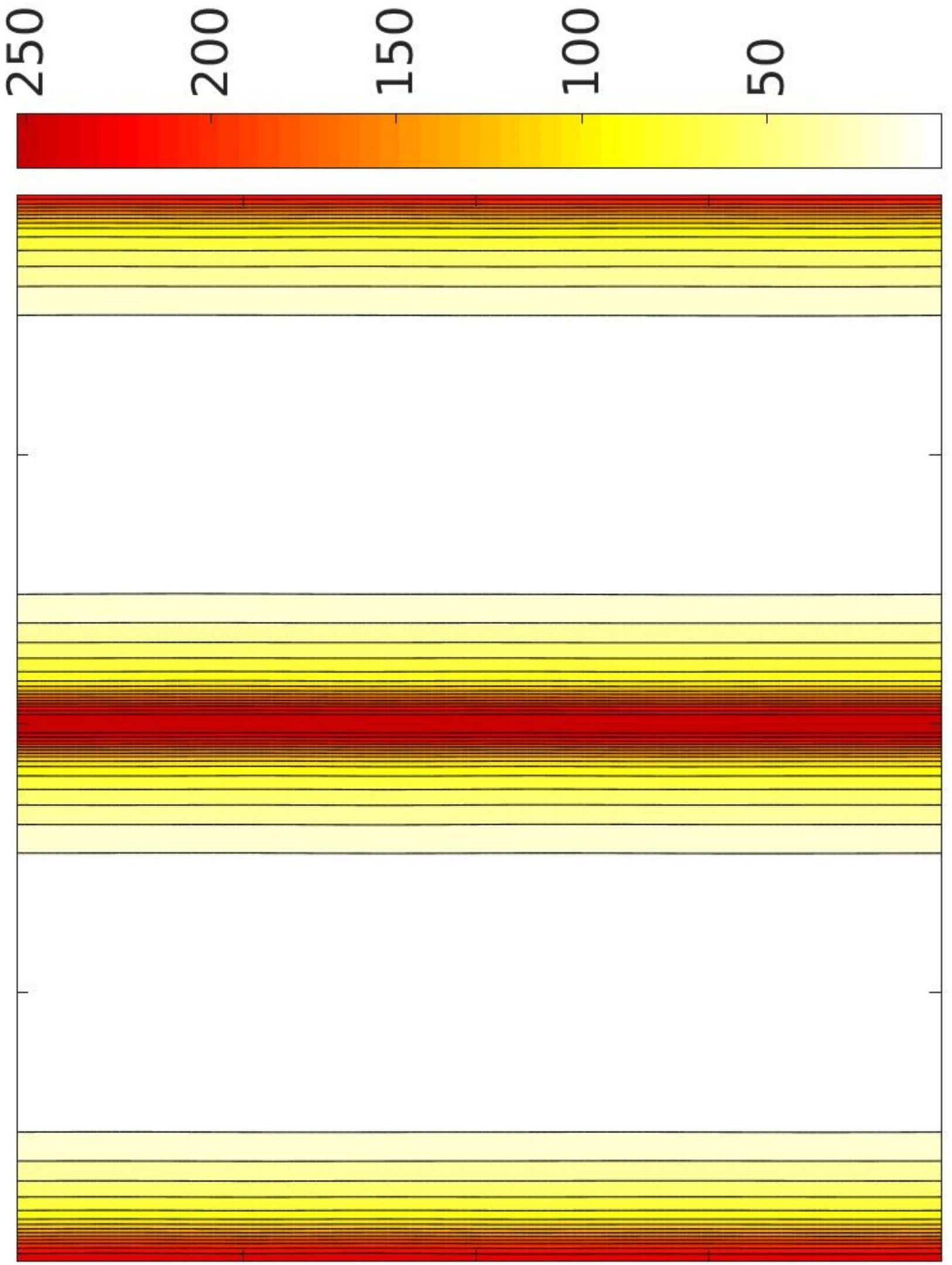
250
200
150
100
50

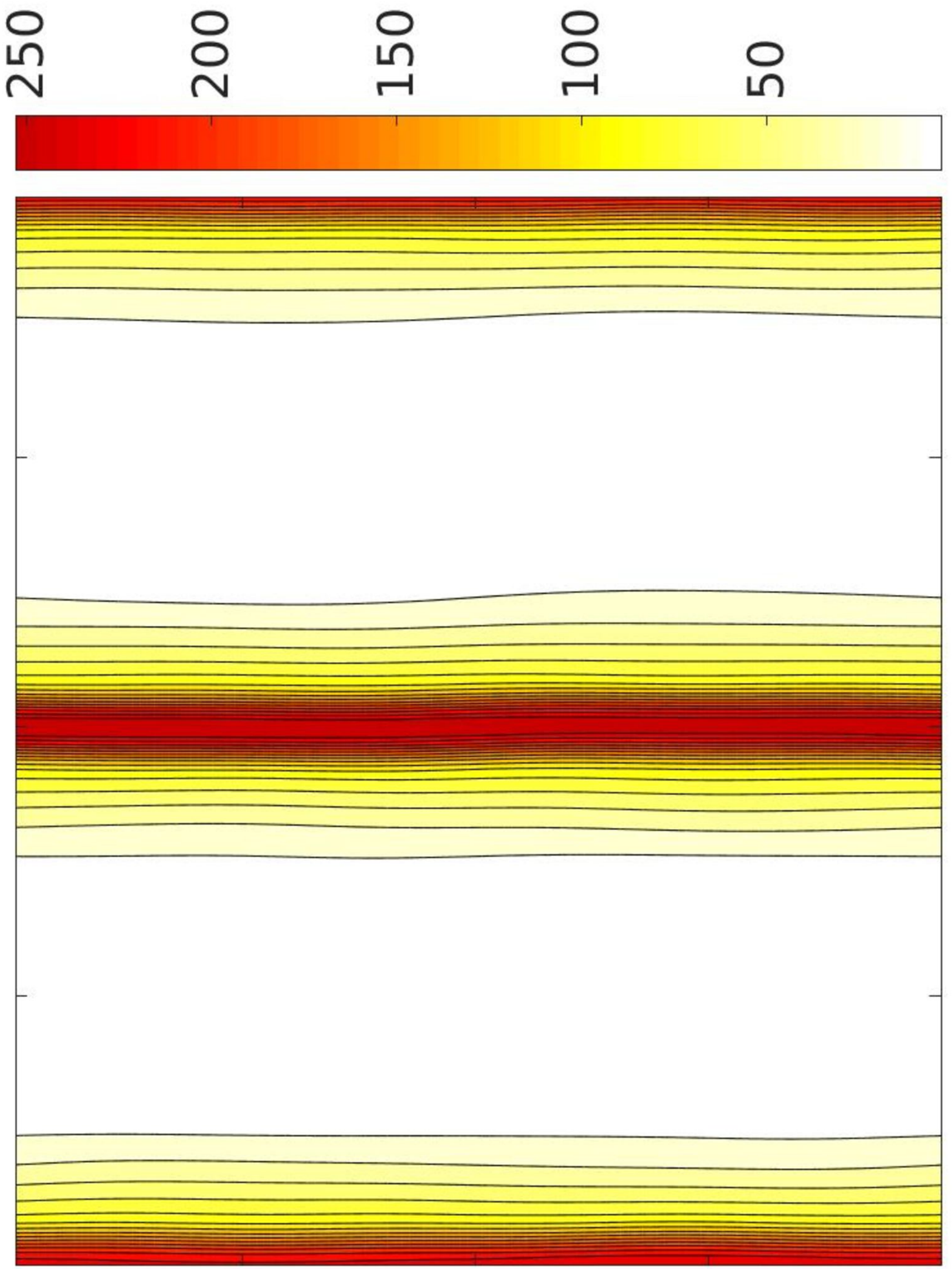
250
200
150
100
50

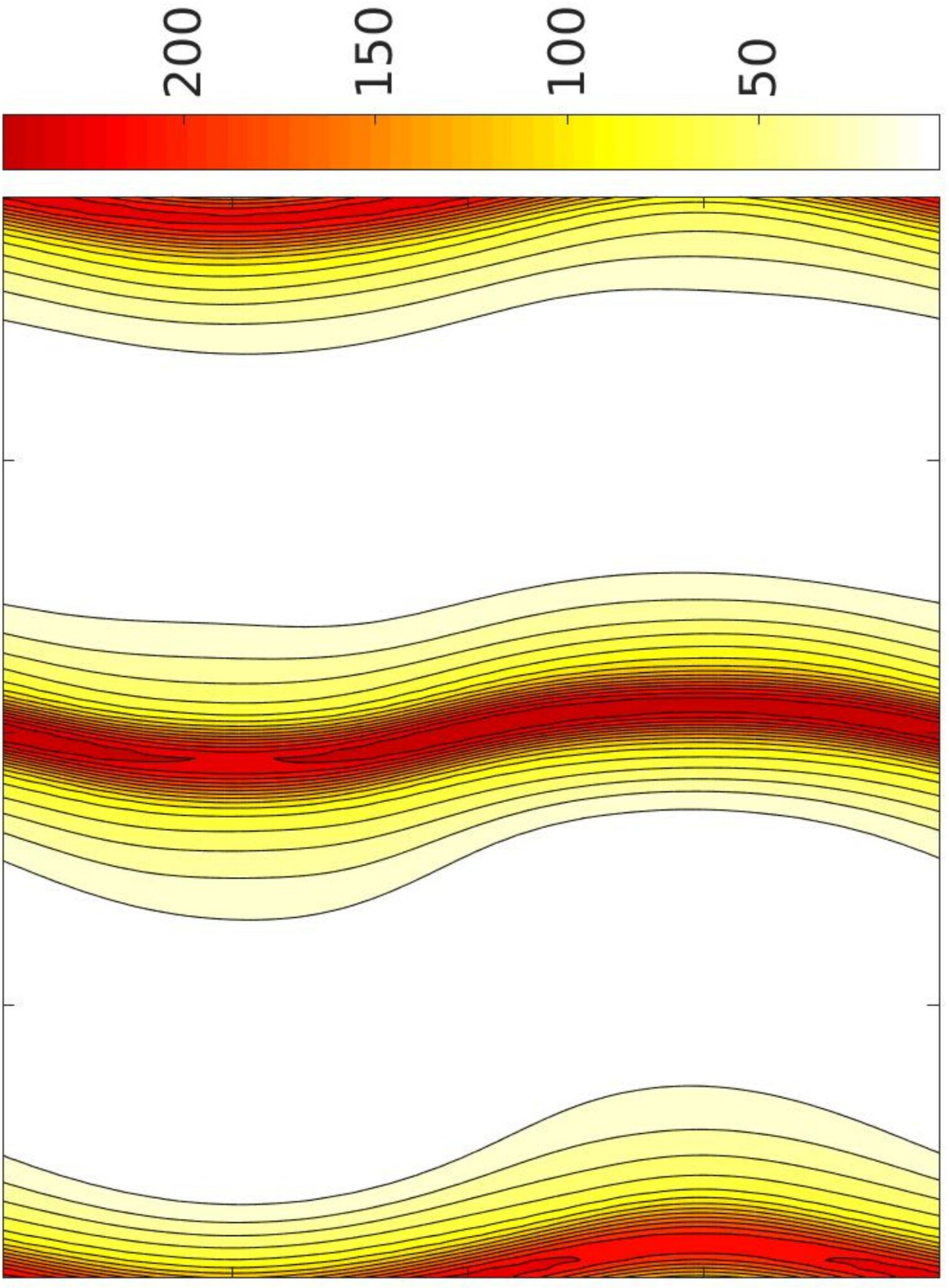
200
150
100
50

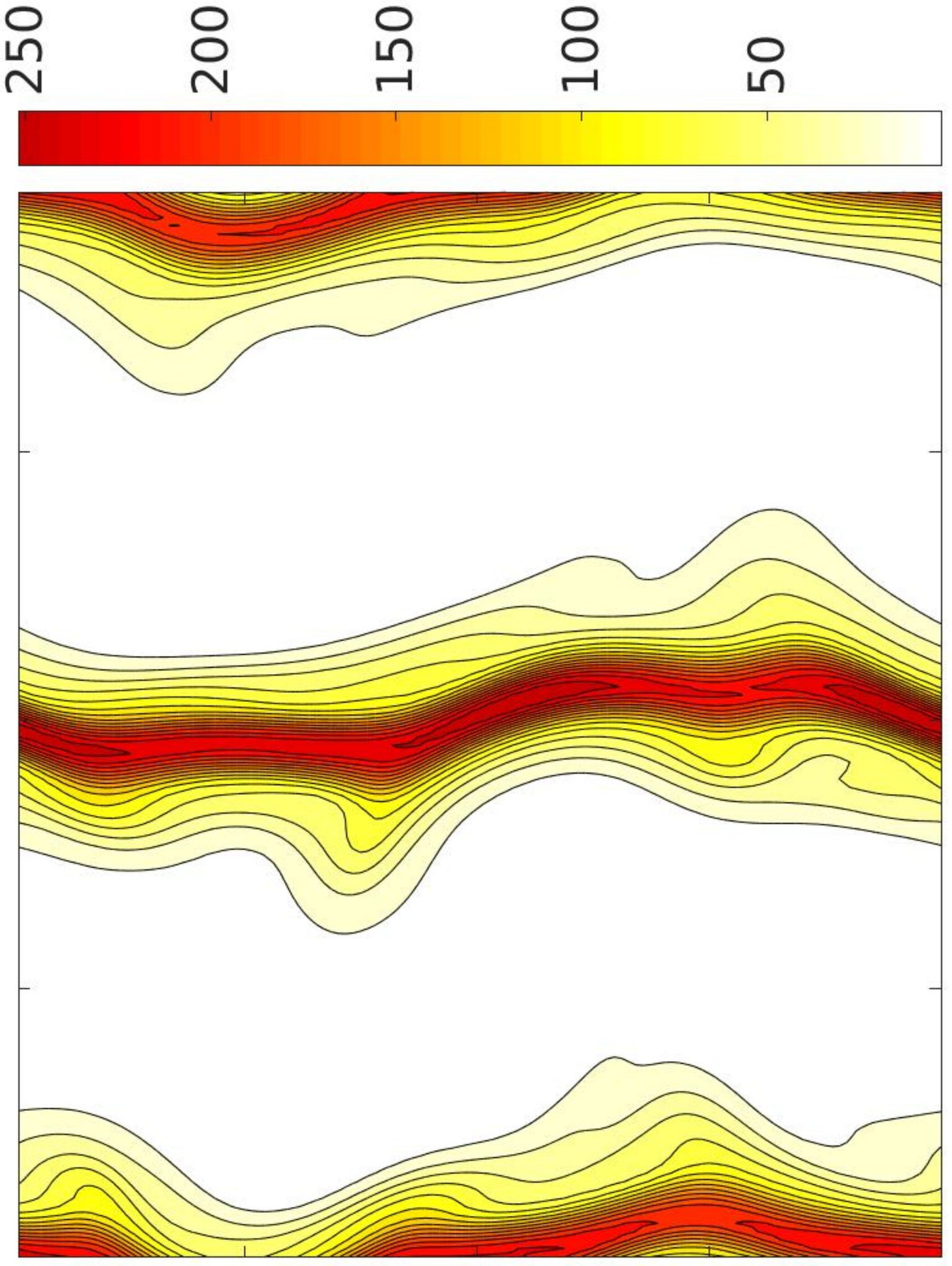
250
200
150
100
50

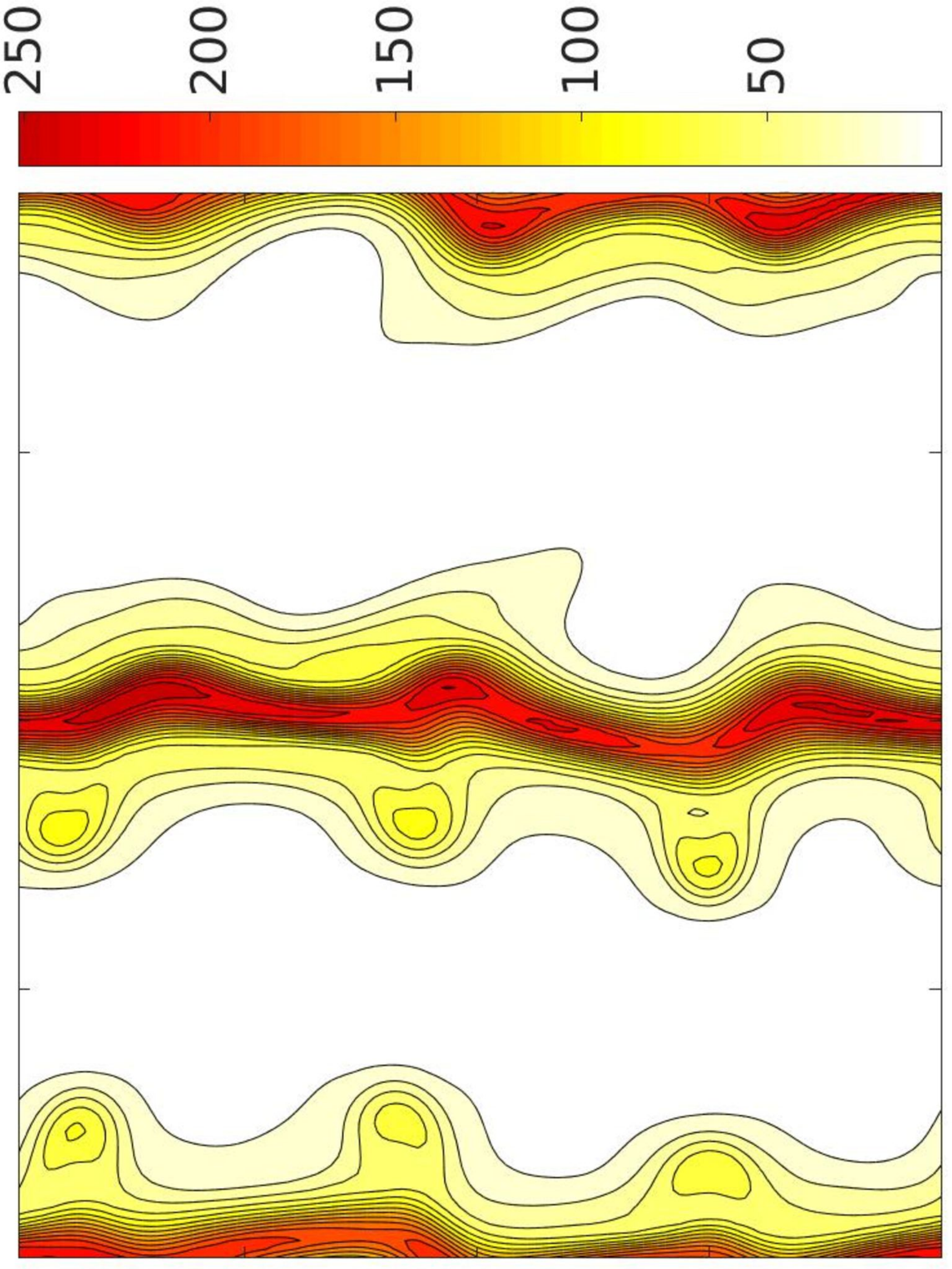
250
200
150
100
50

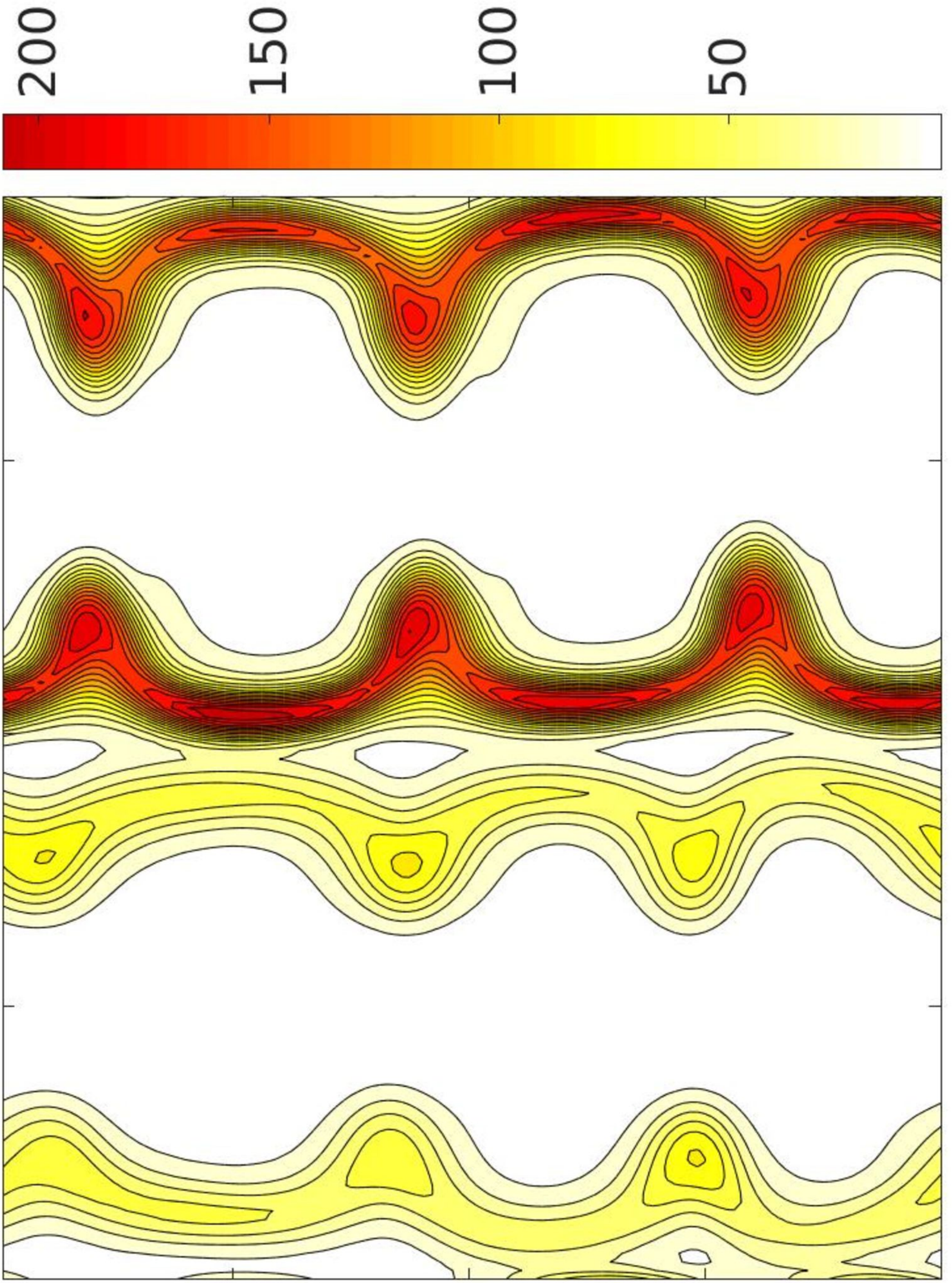
200
150
100
50

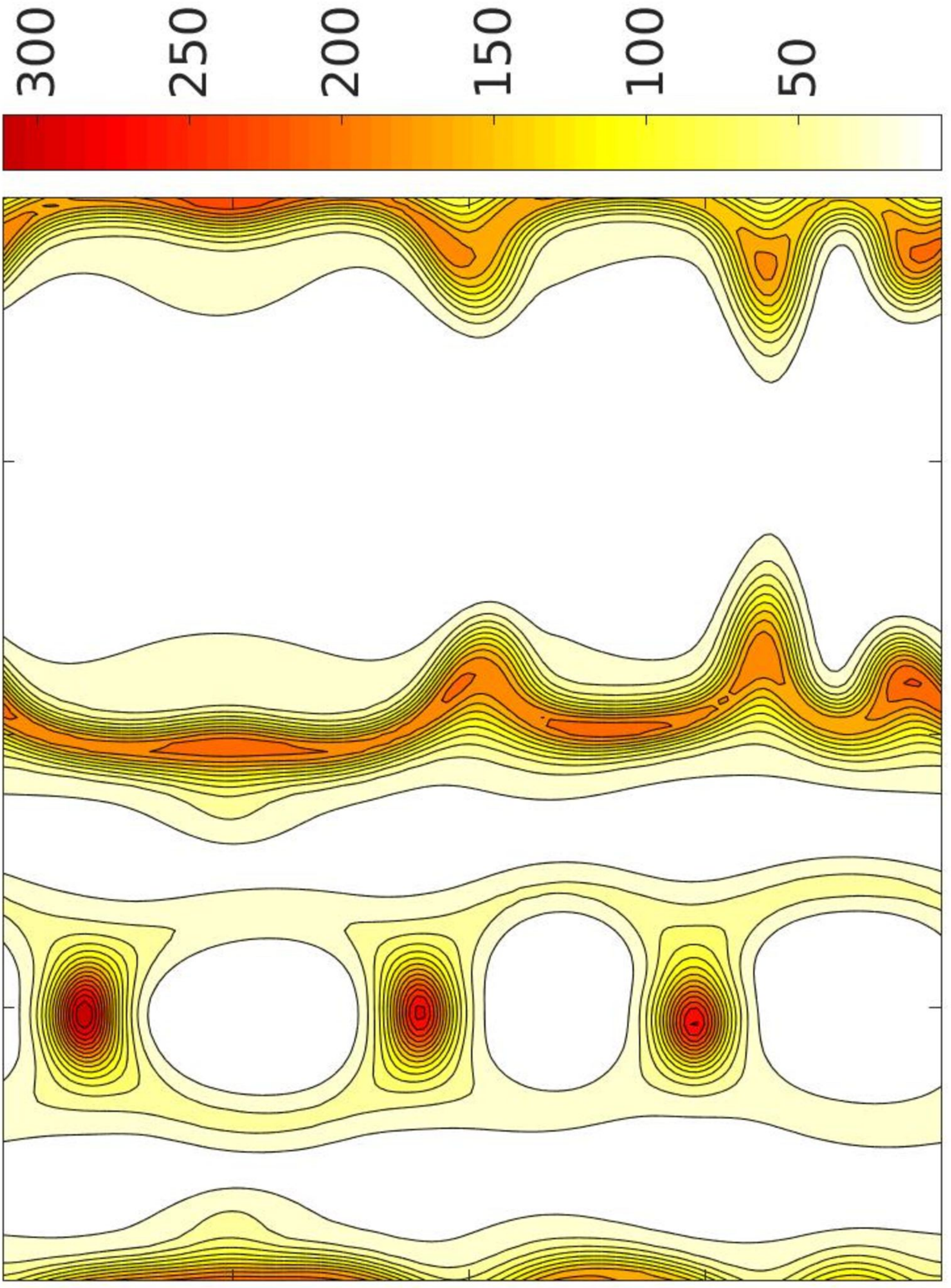
300
250
200
150
100
50

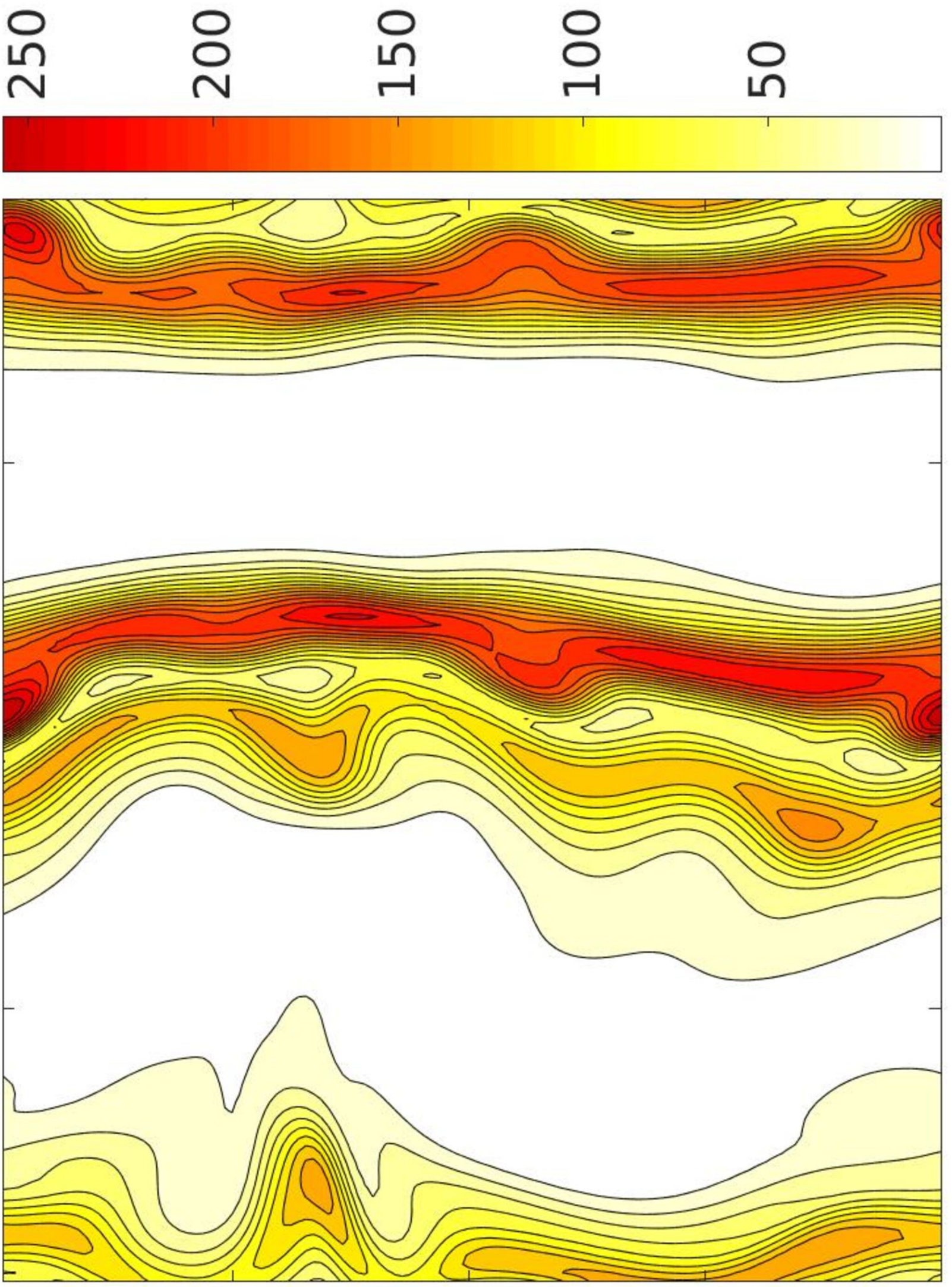
250
200
150
100
50

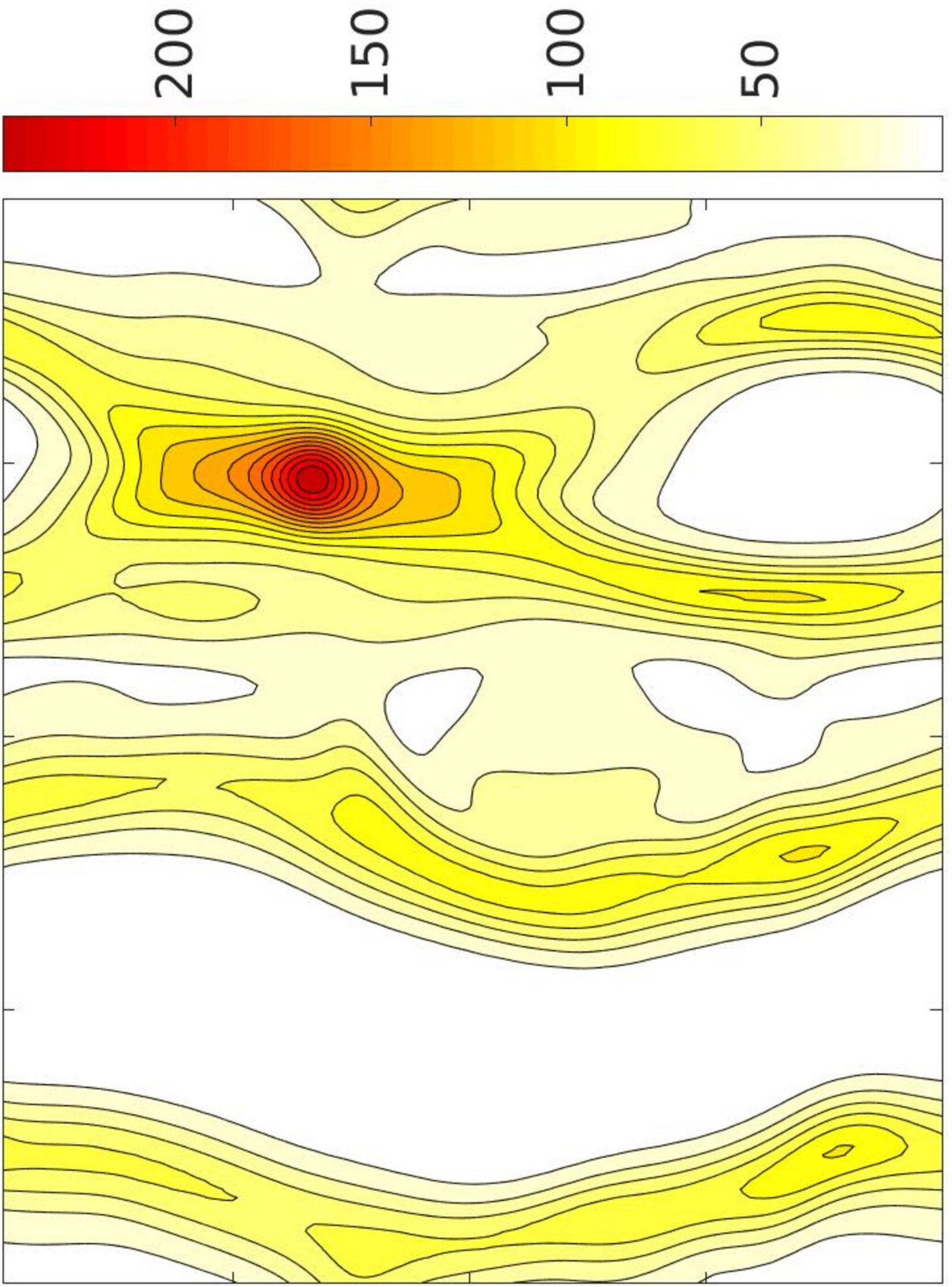
200
150
100
50

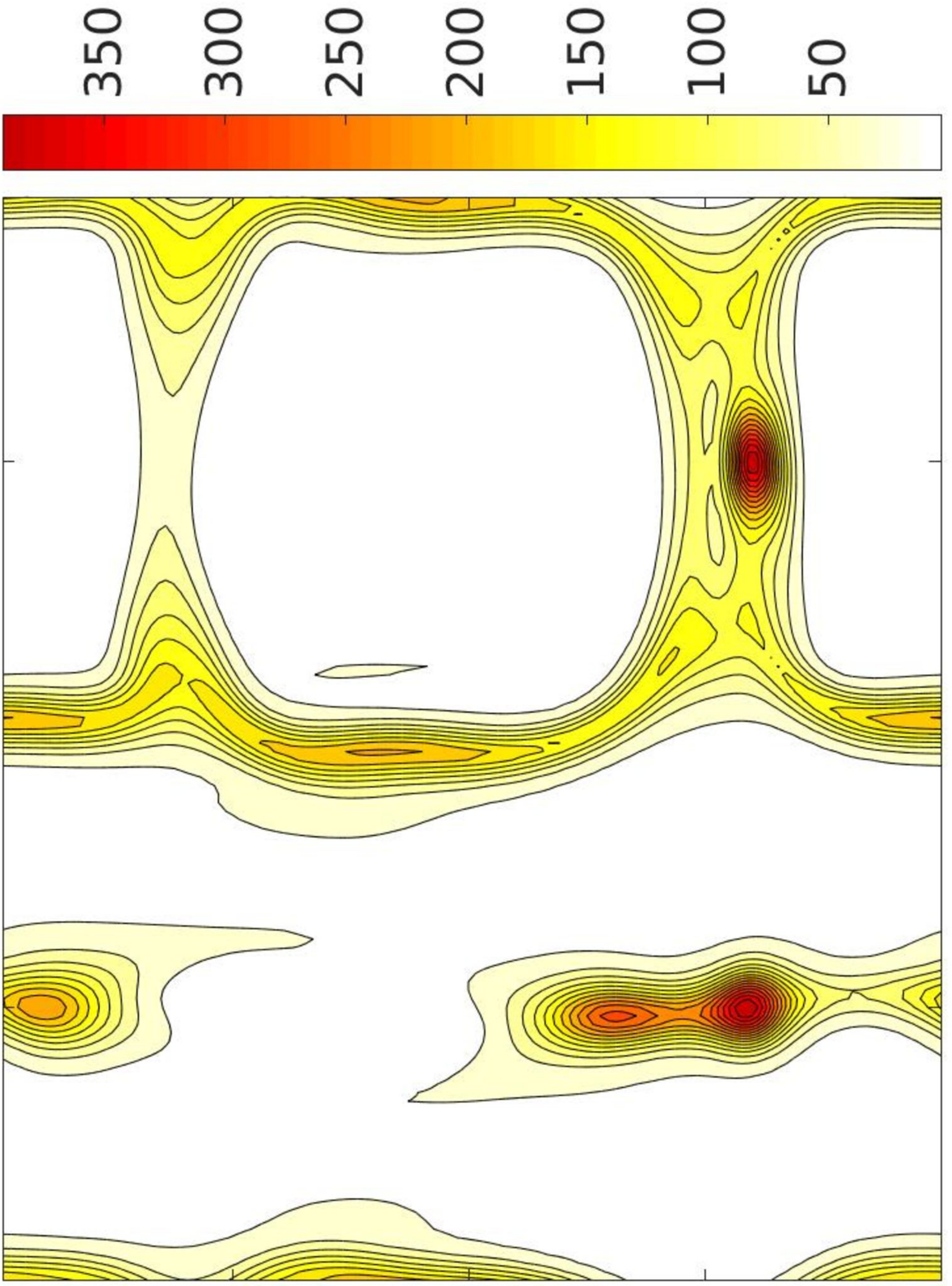
350
300
250
200
150
100
50

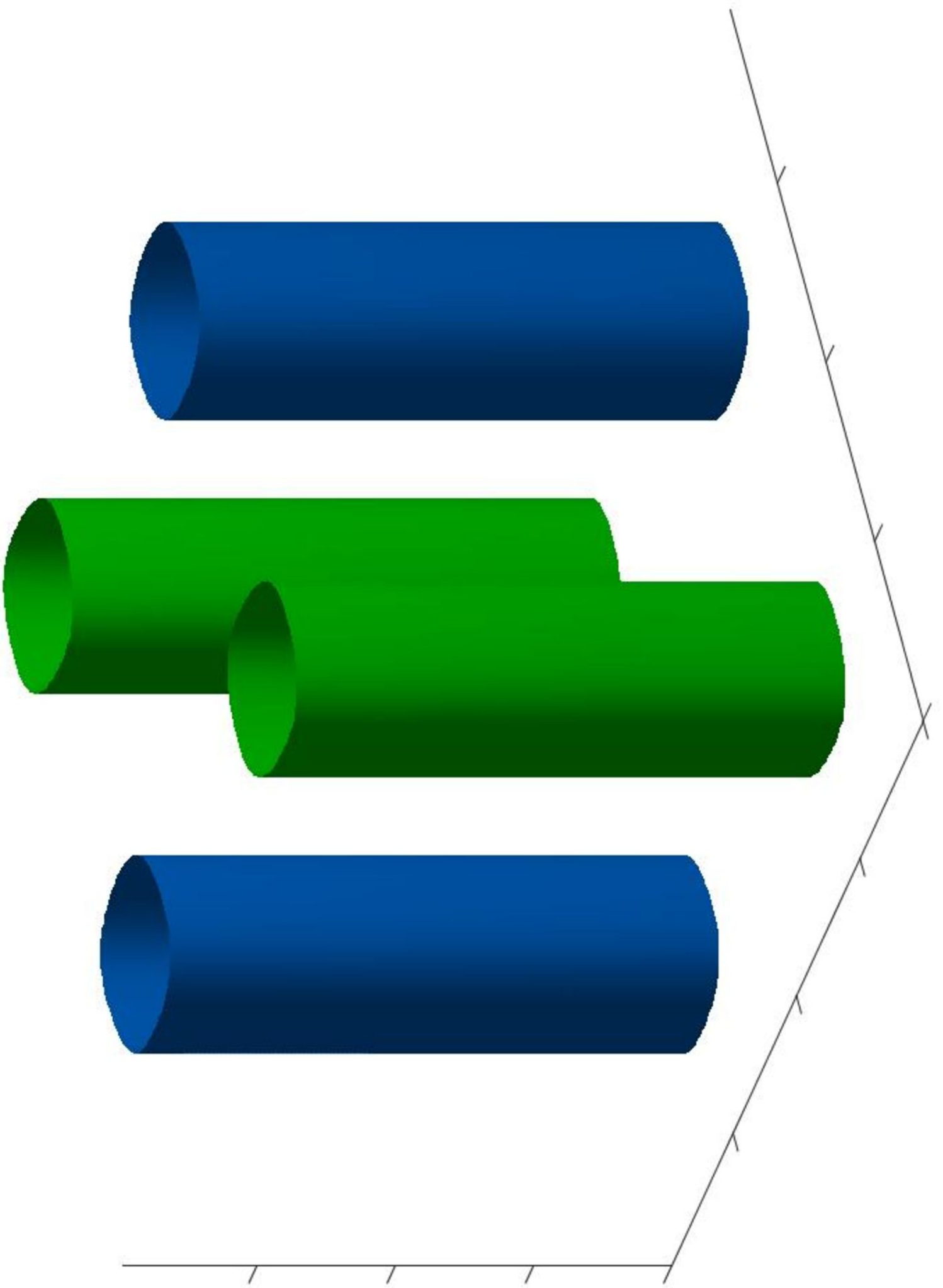

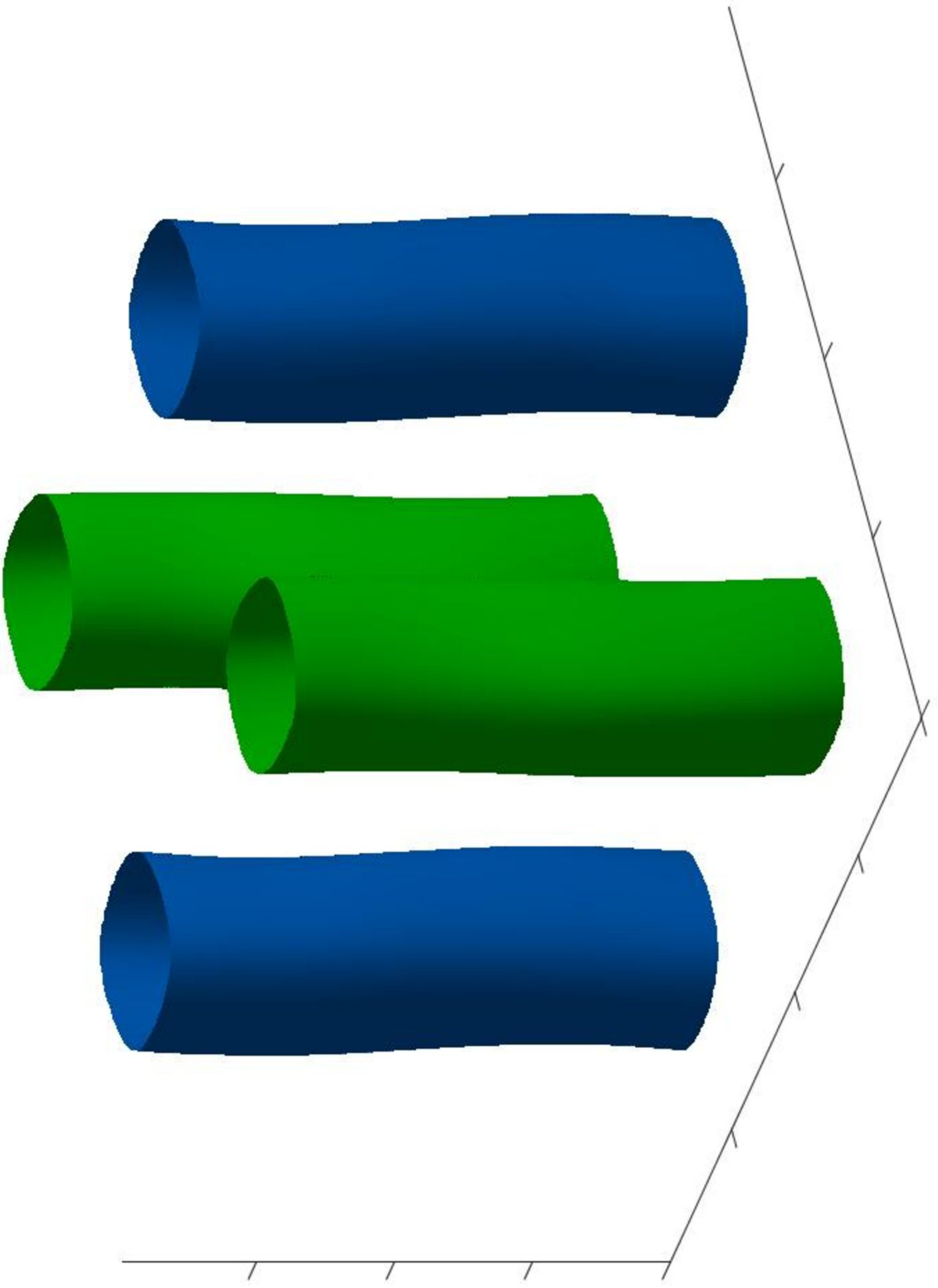

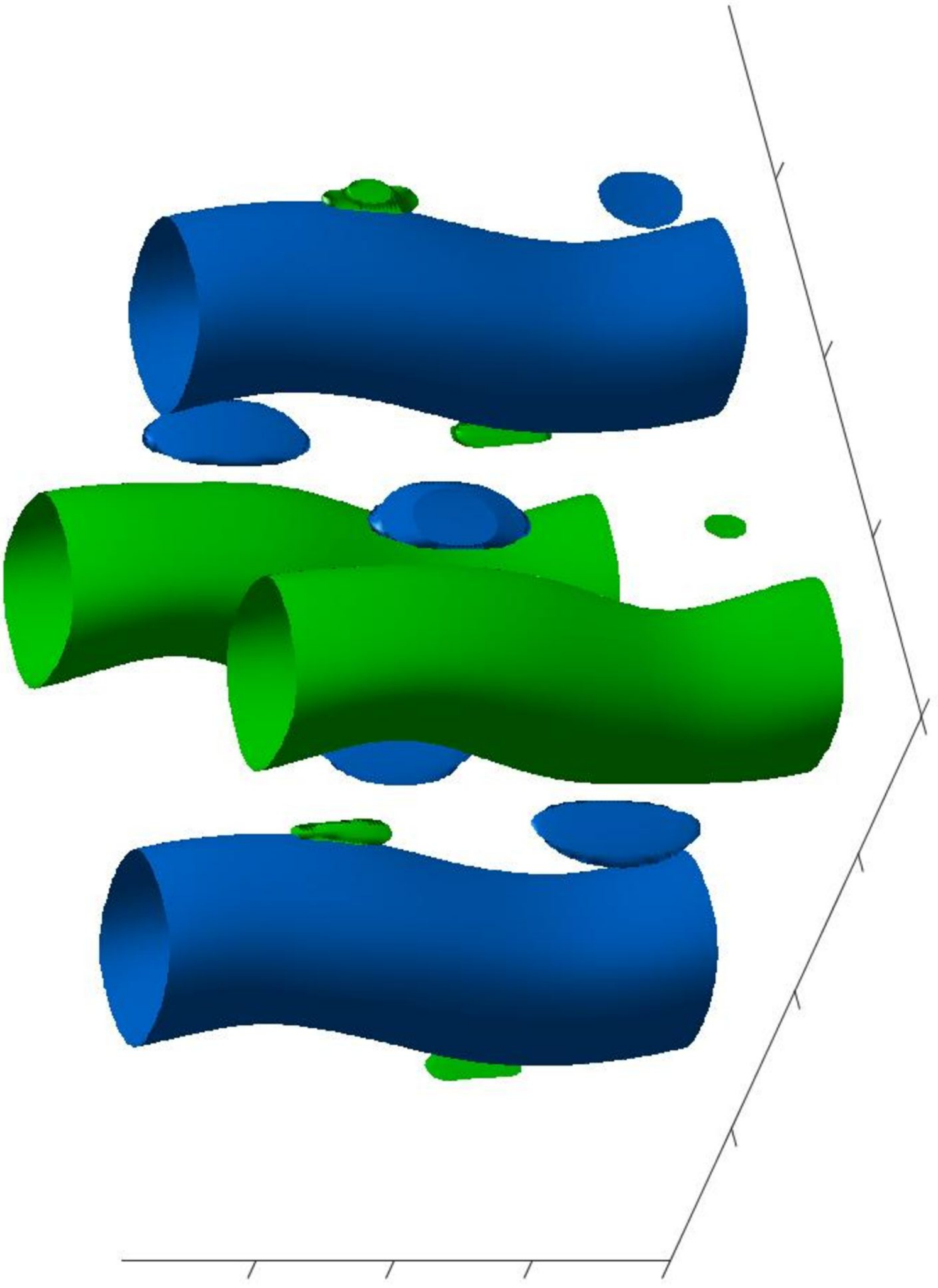

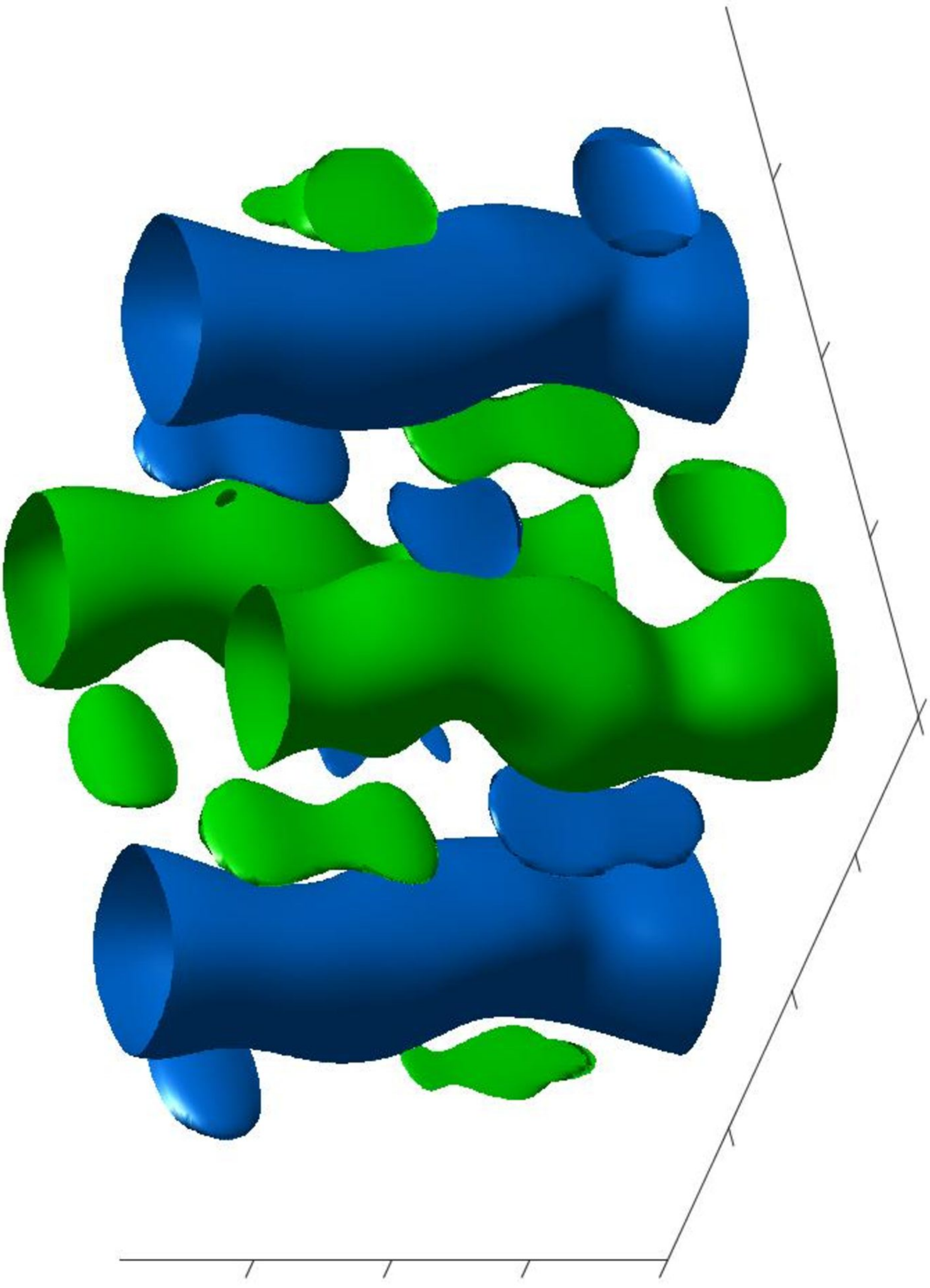

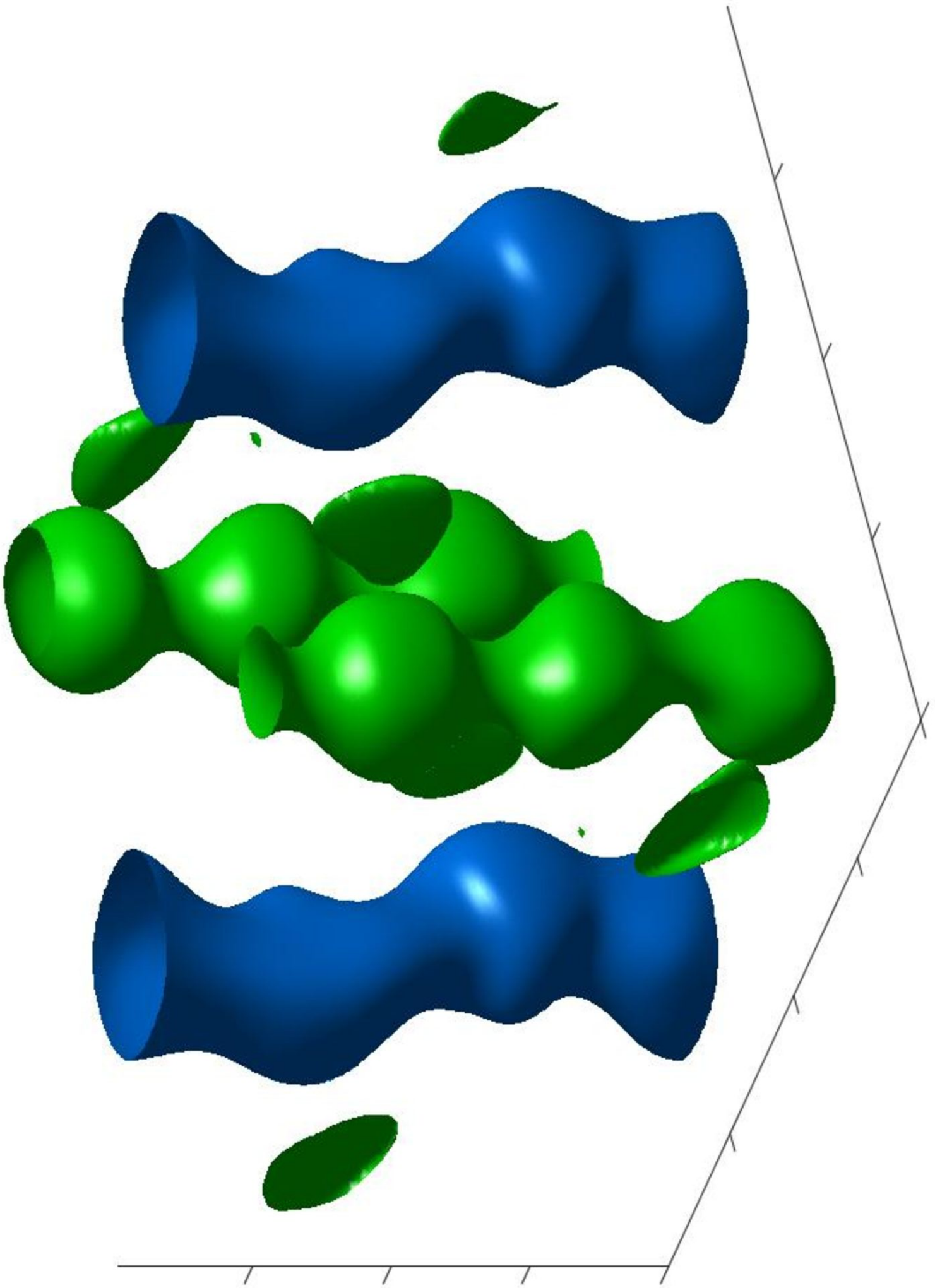

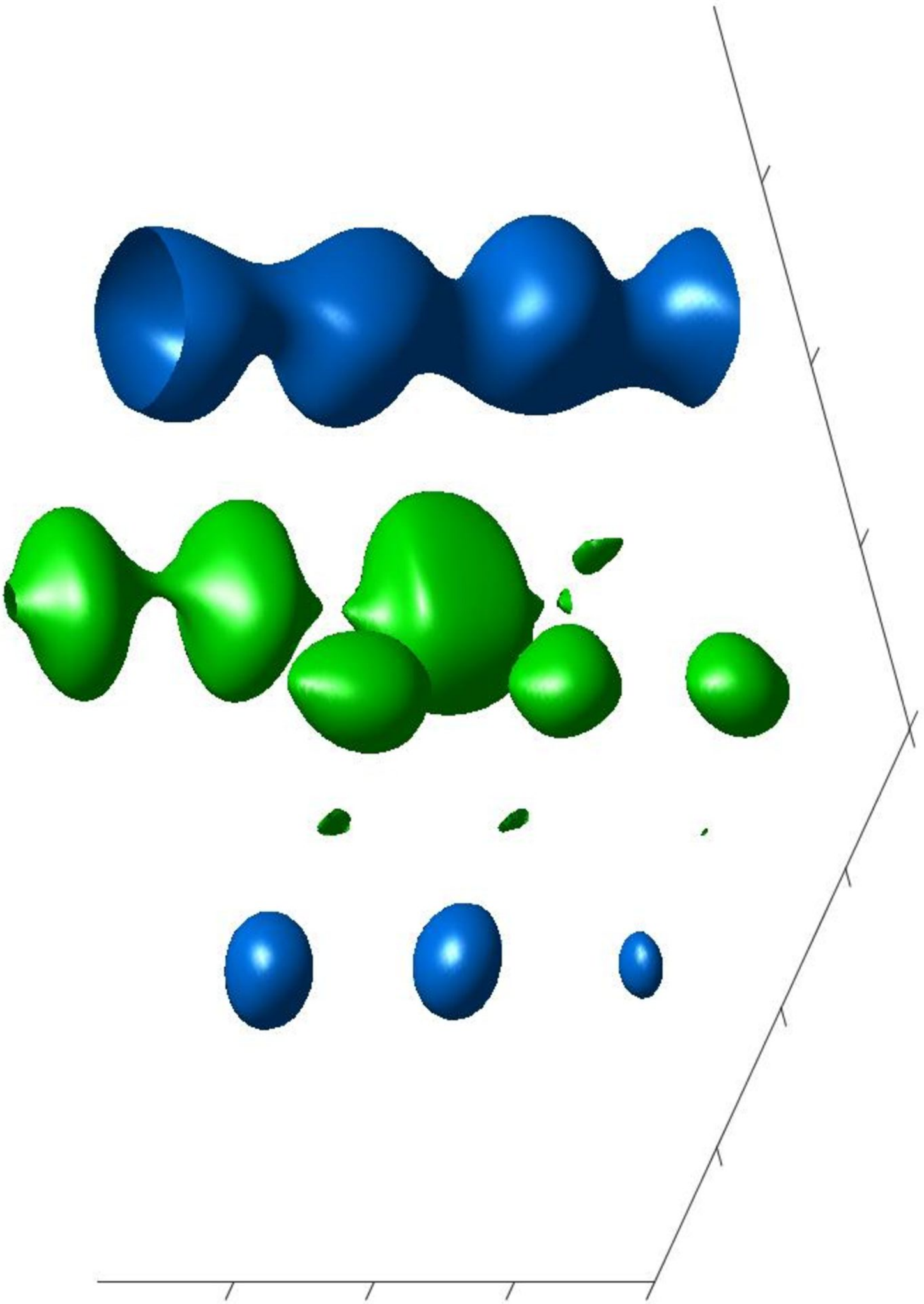

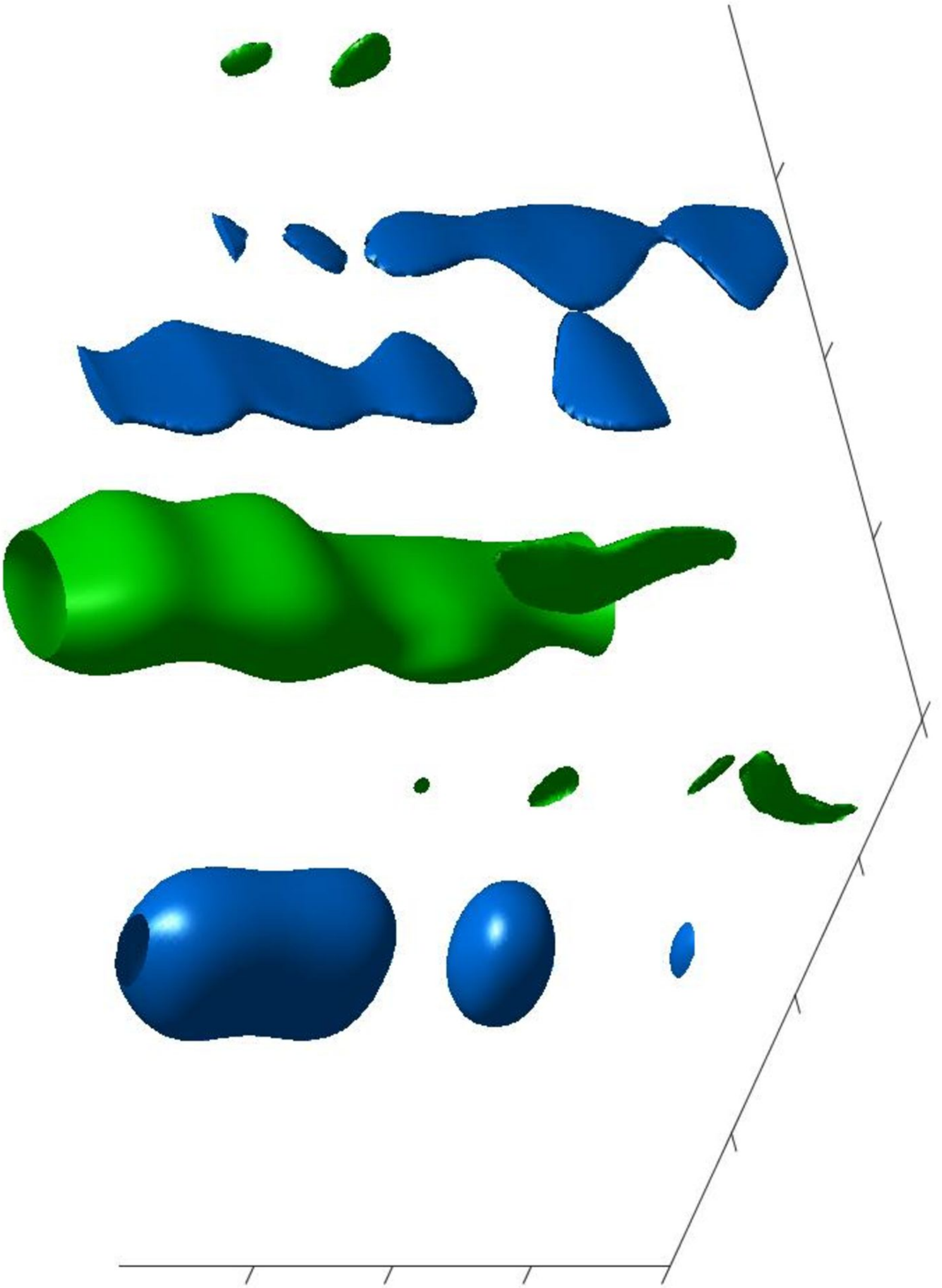

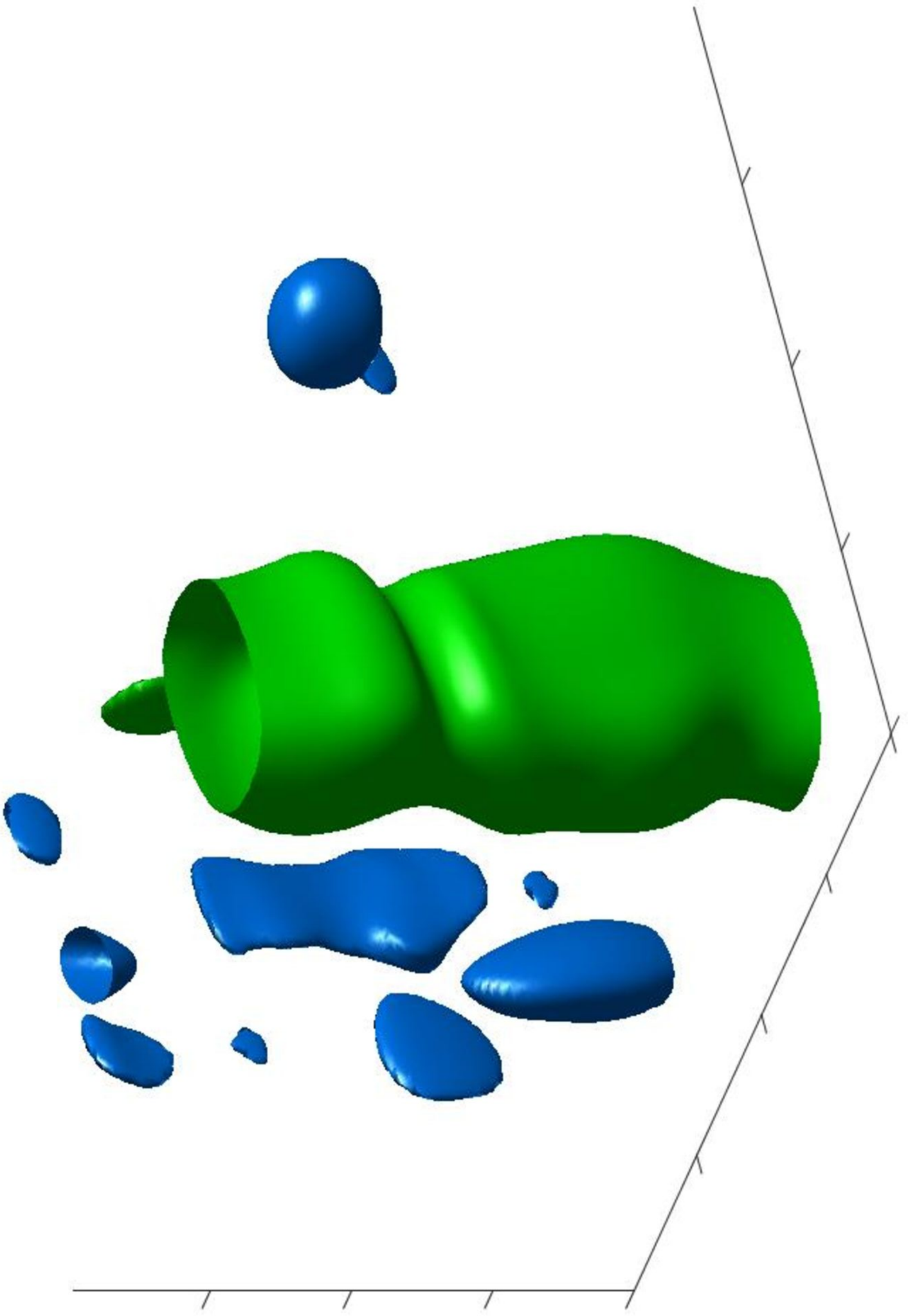

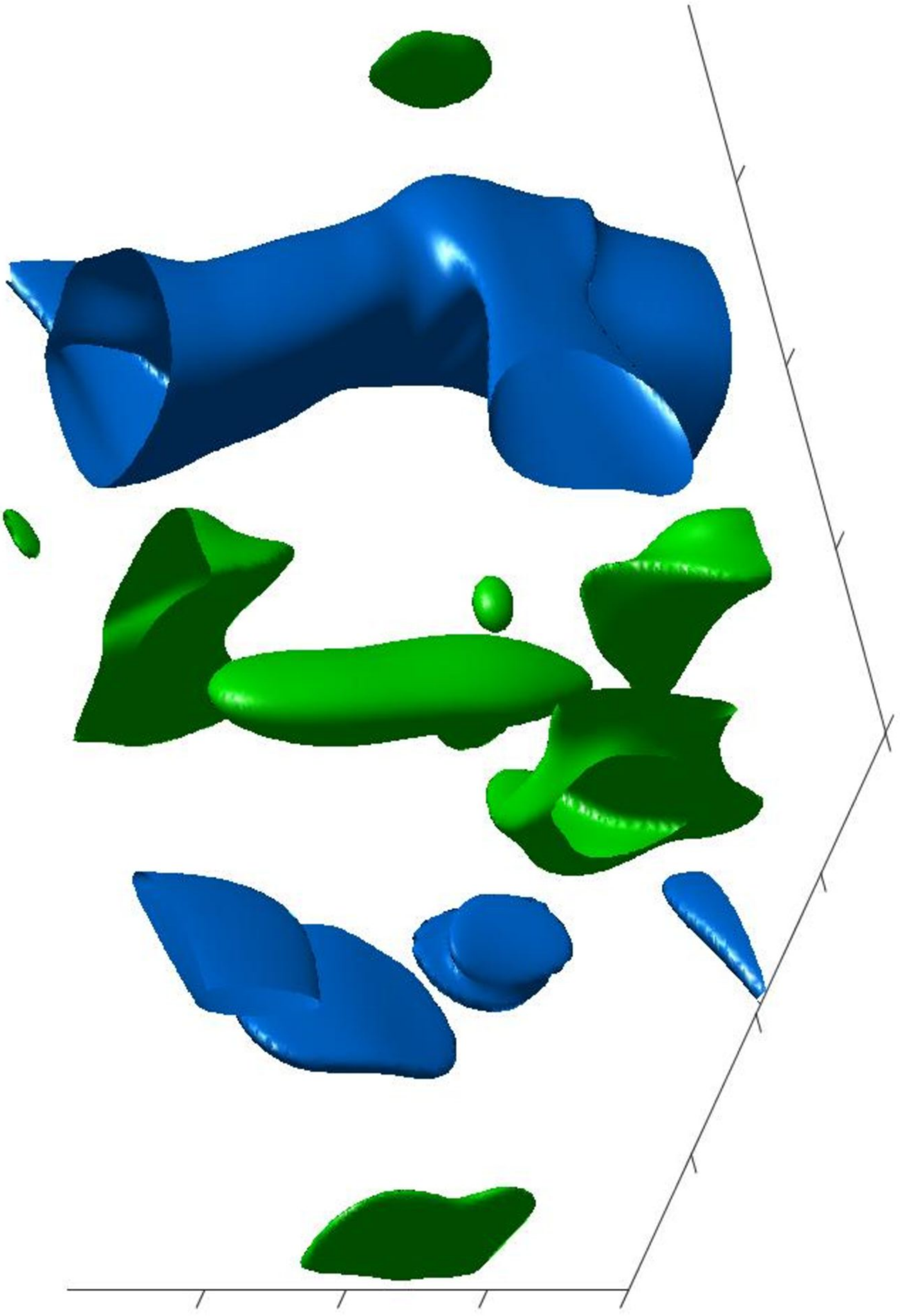

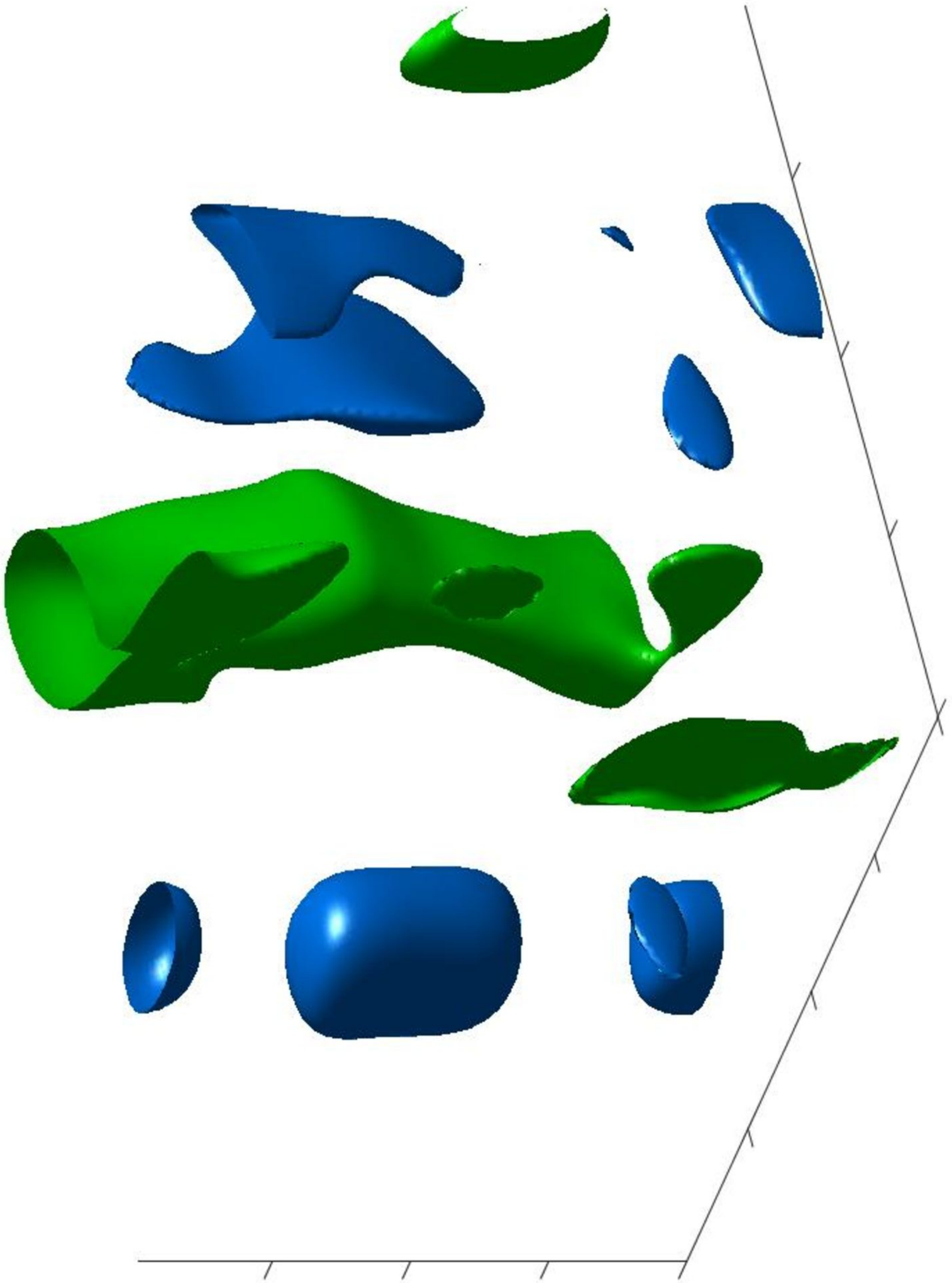

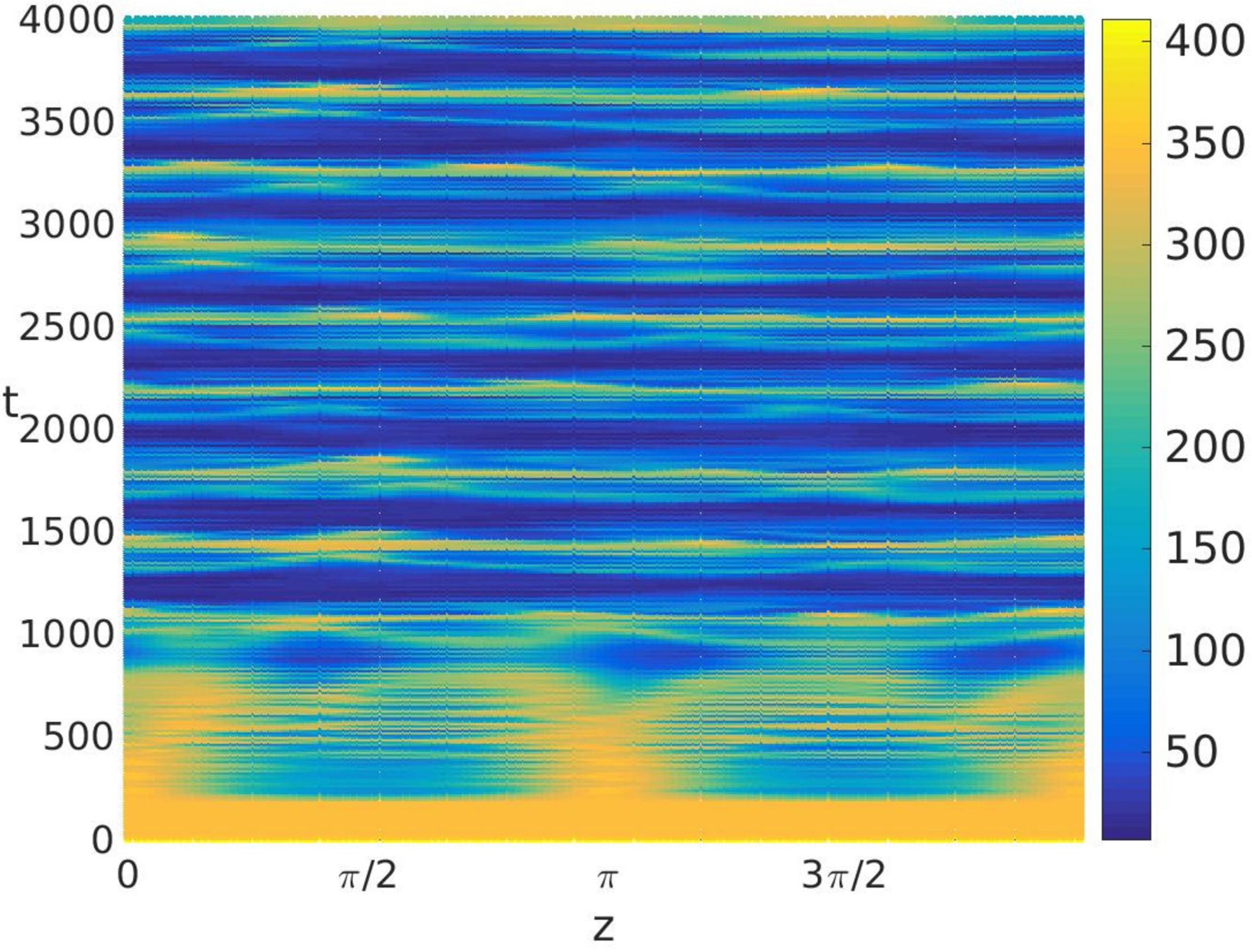

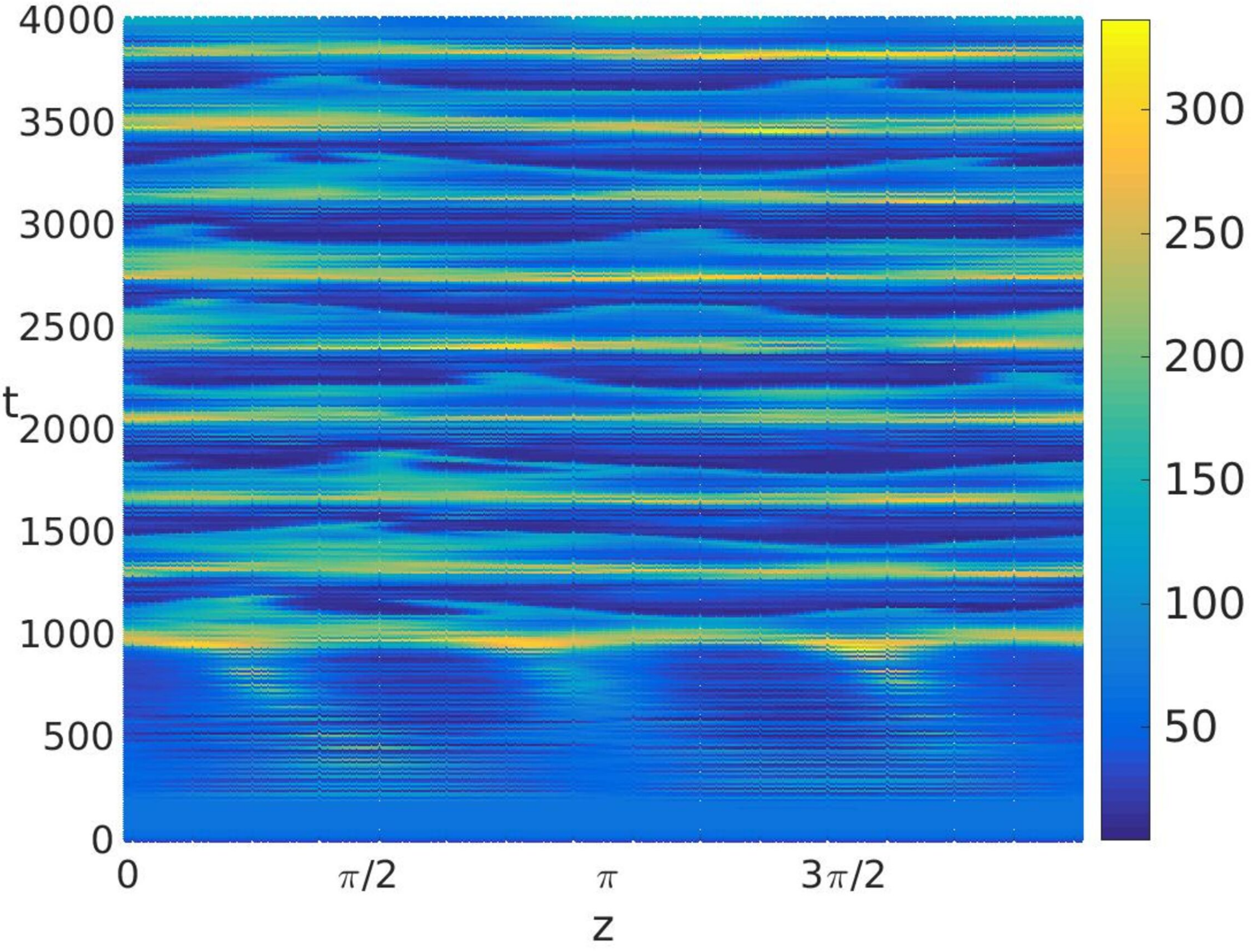

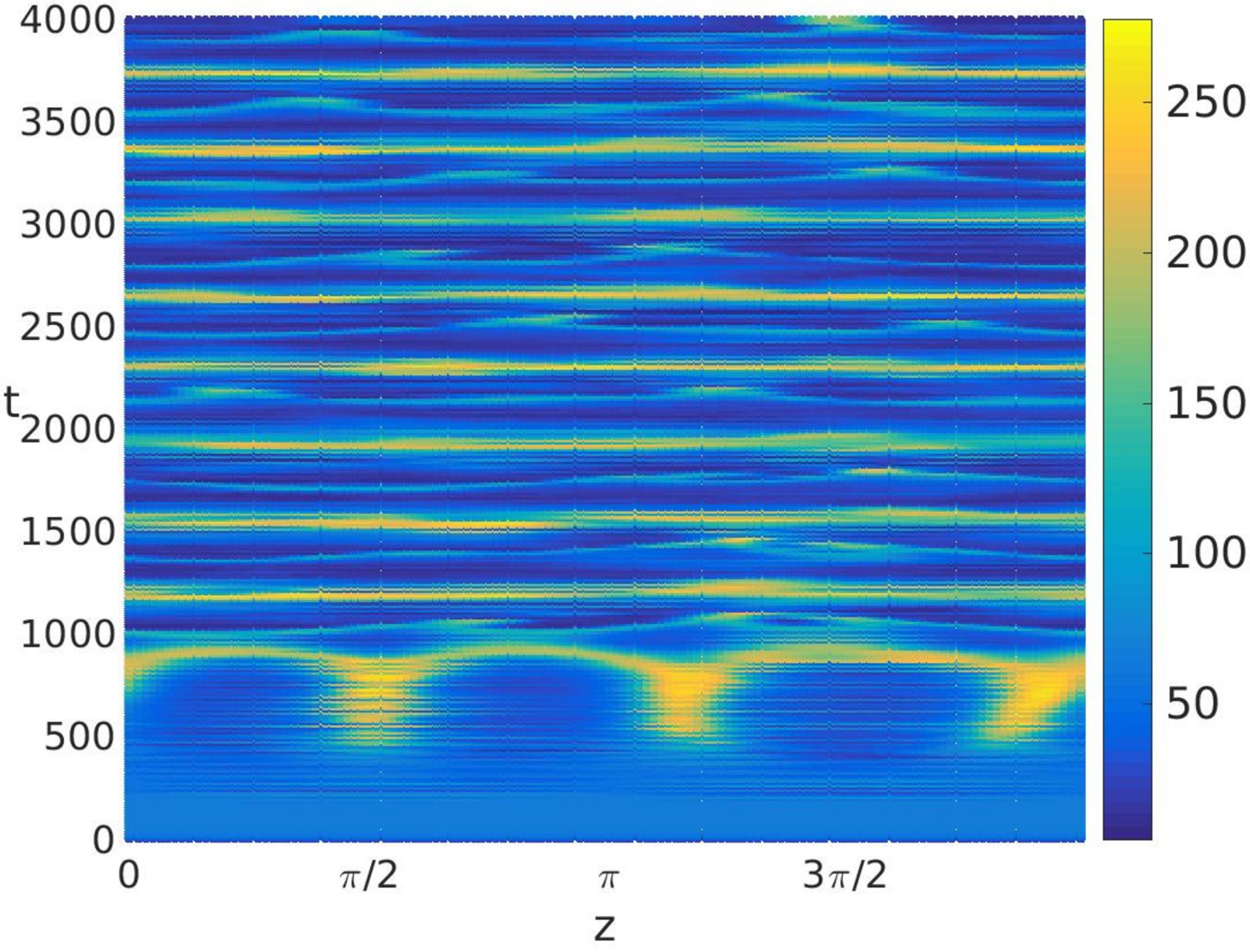

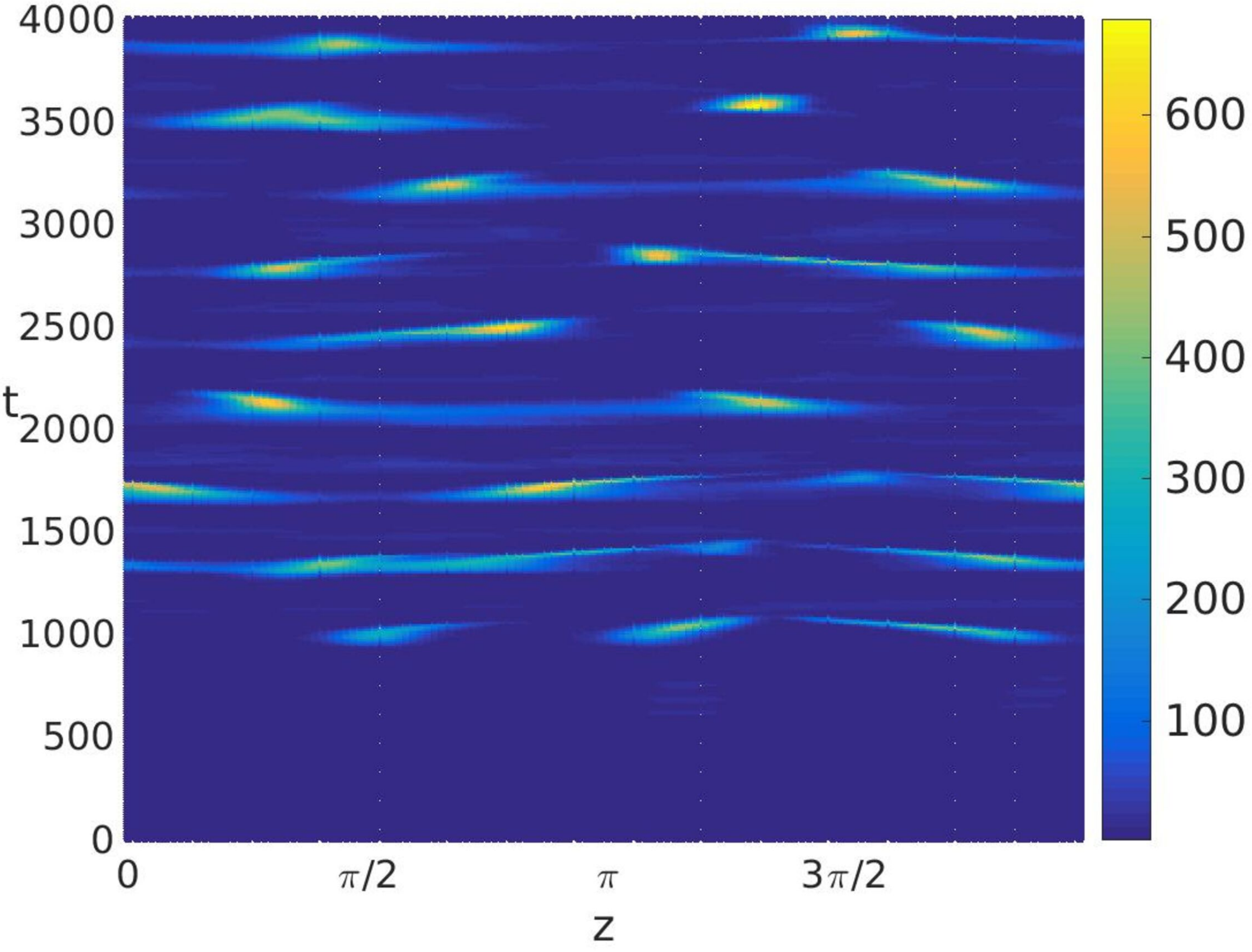

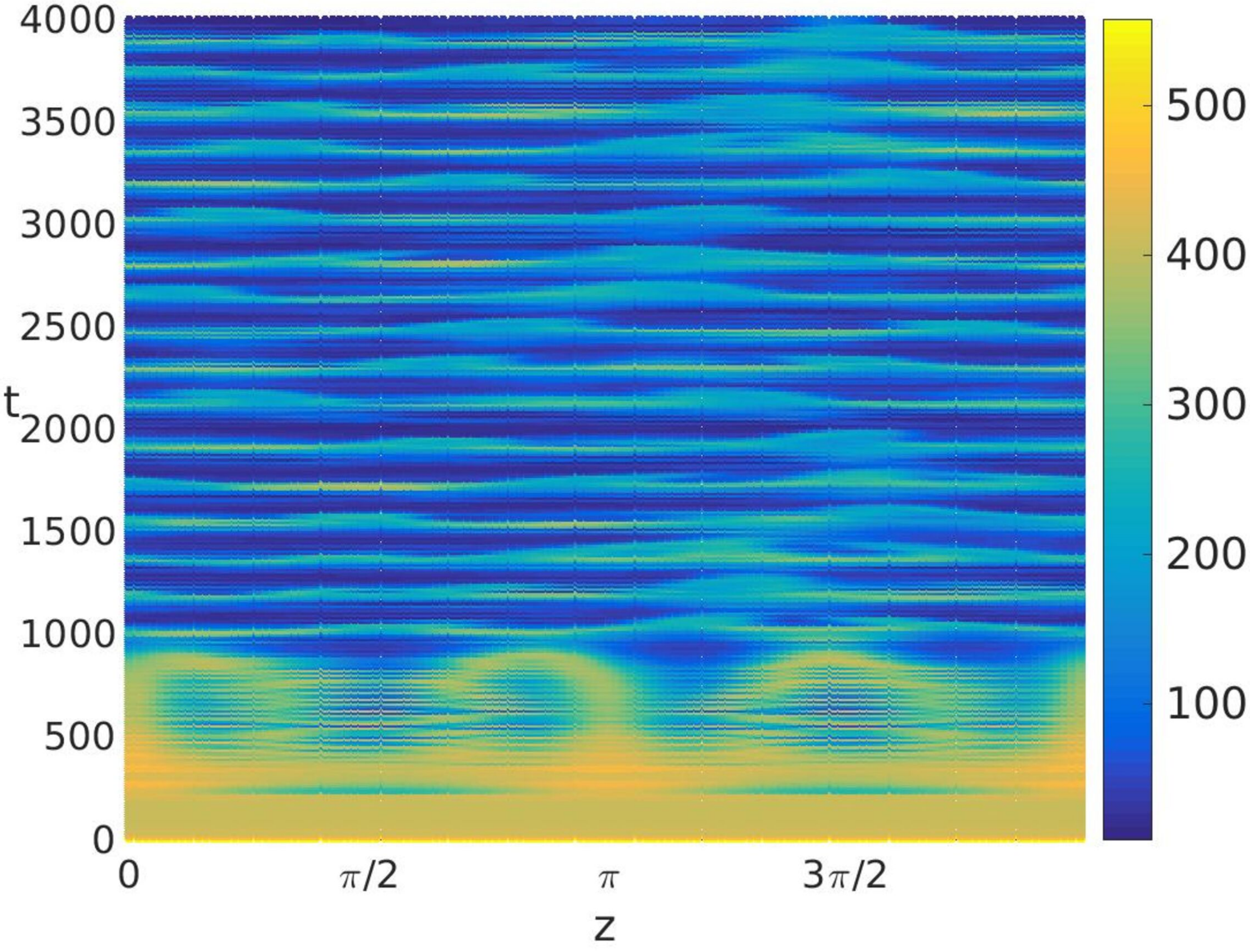

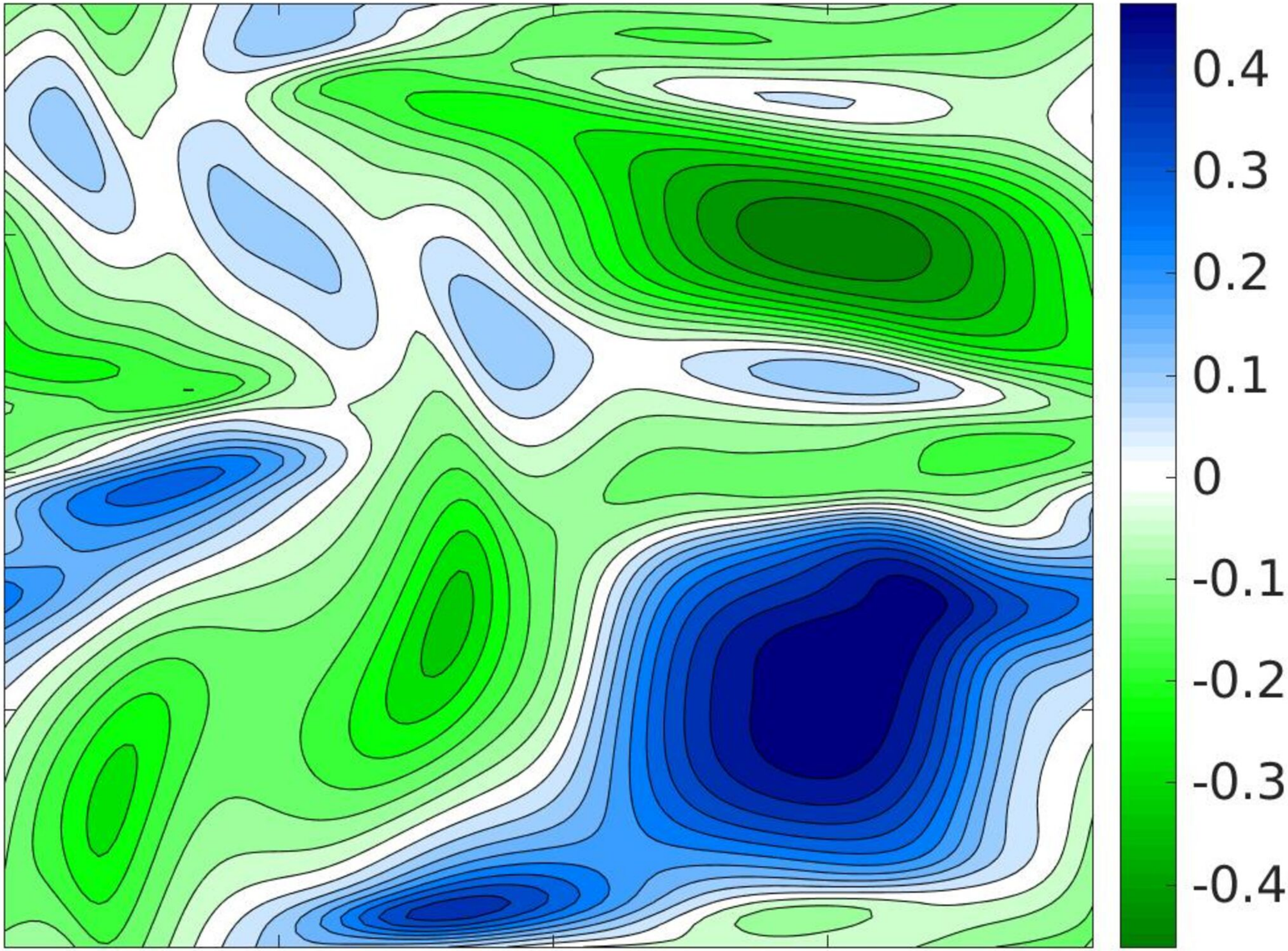

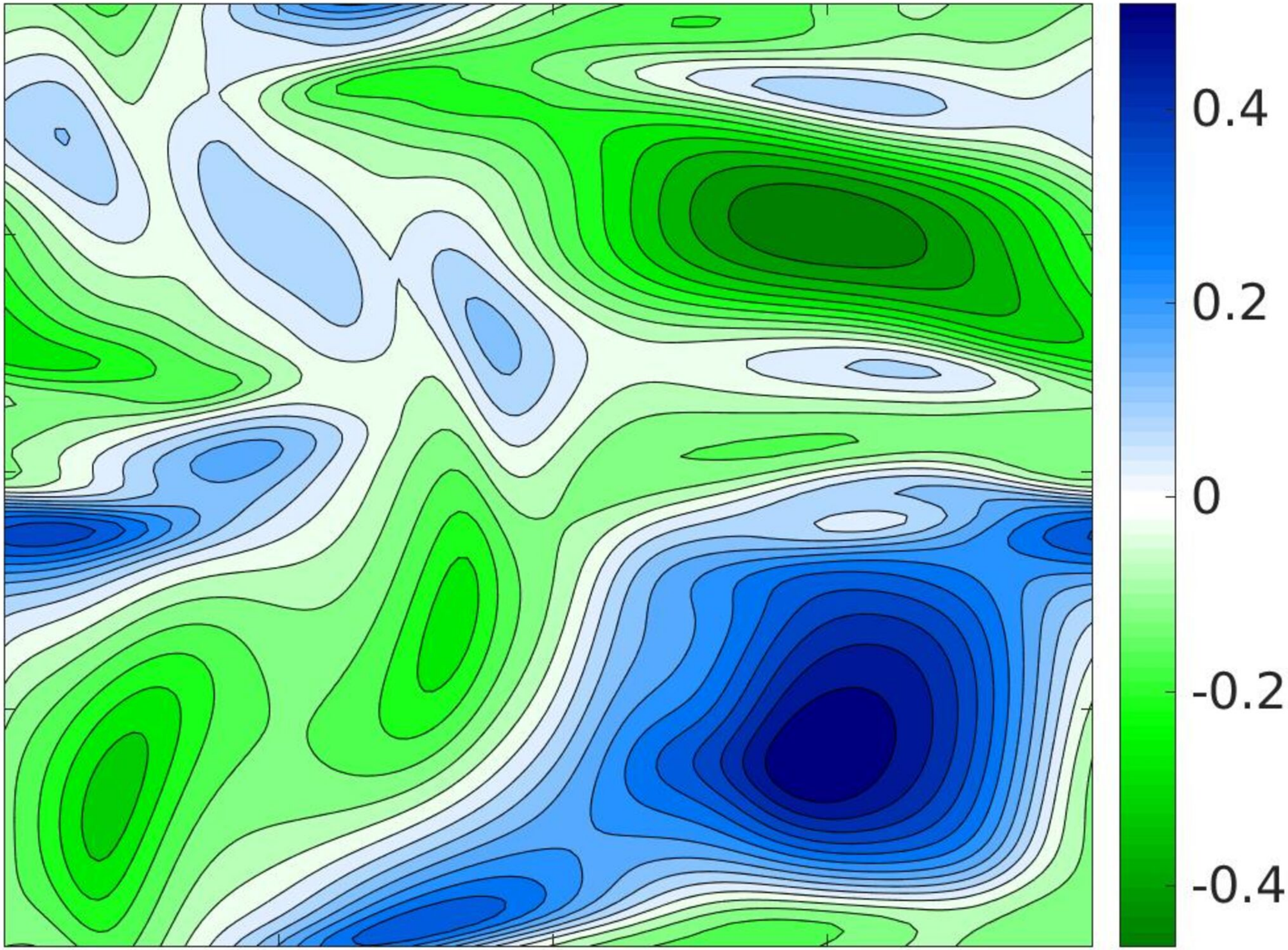

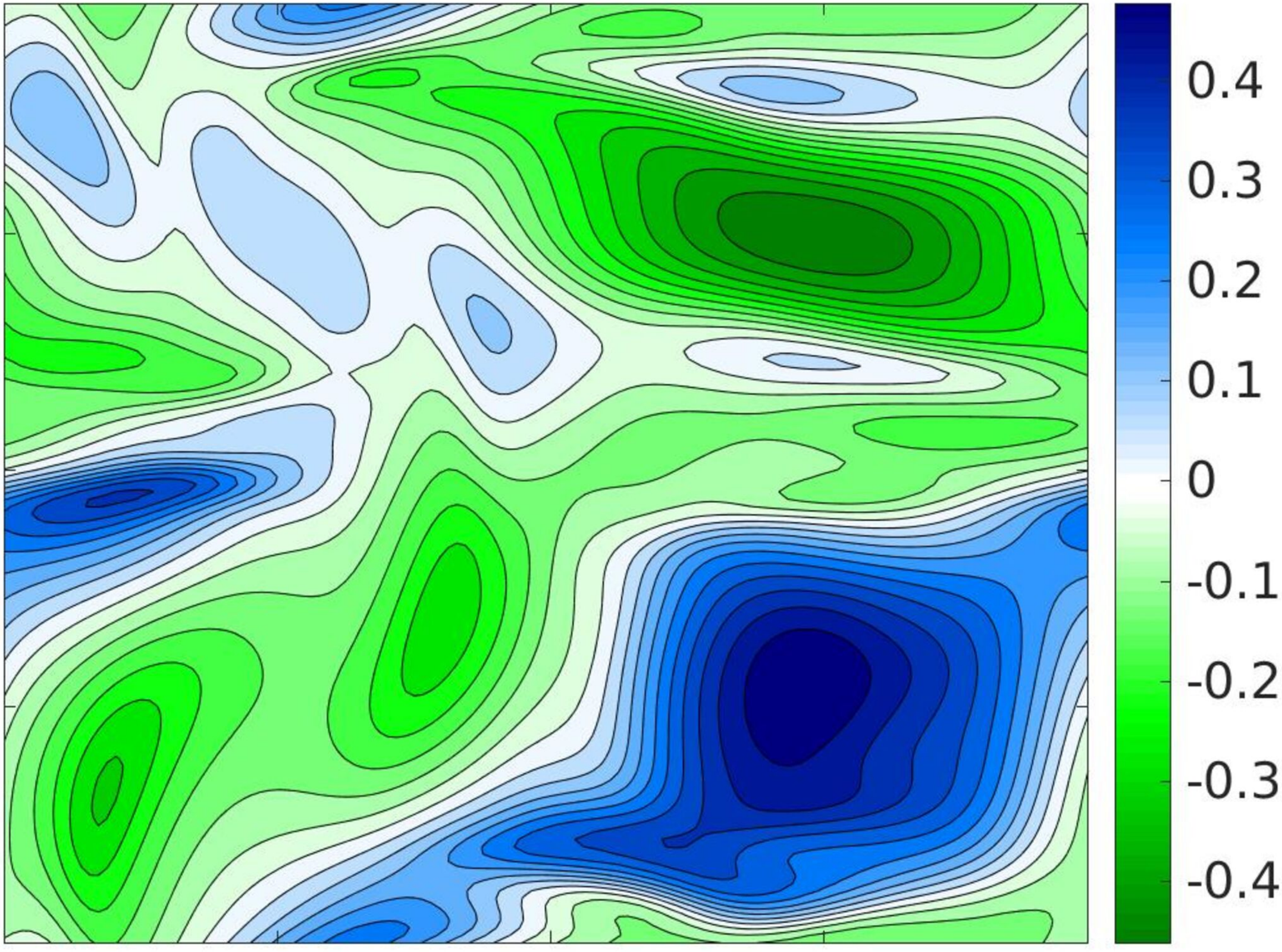

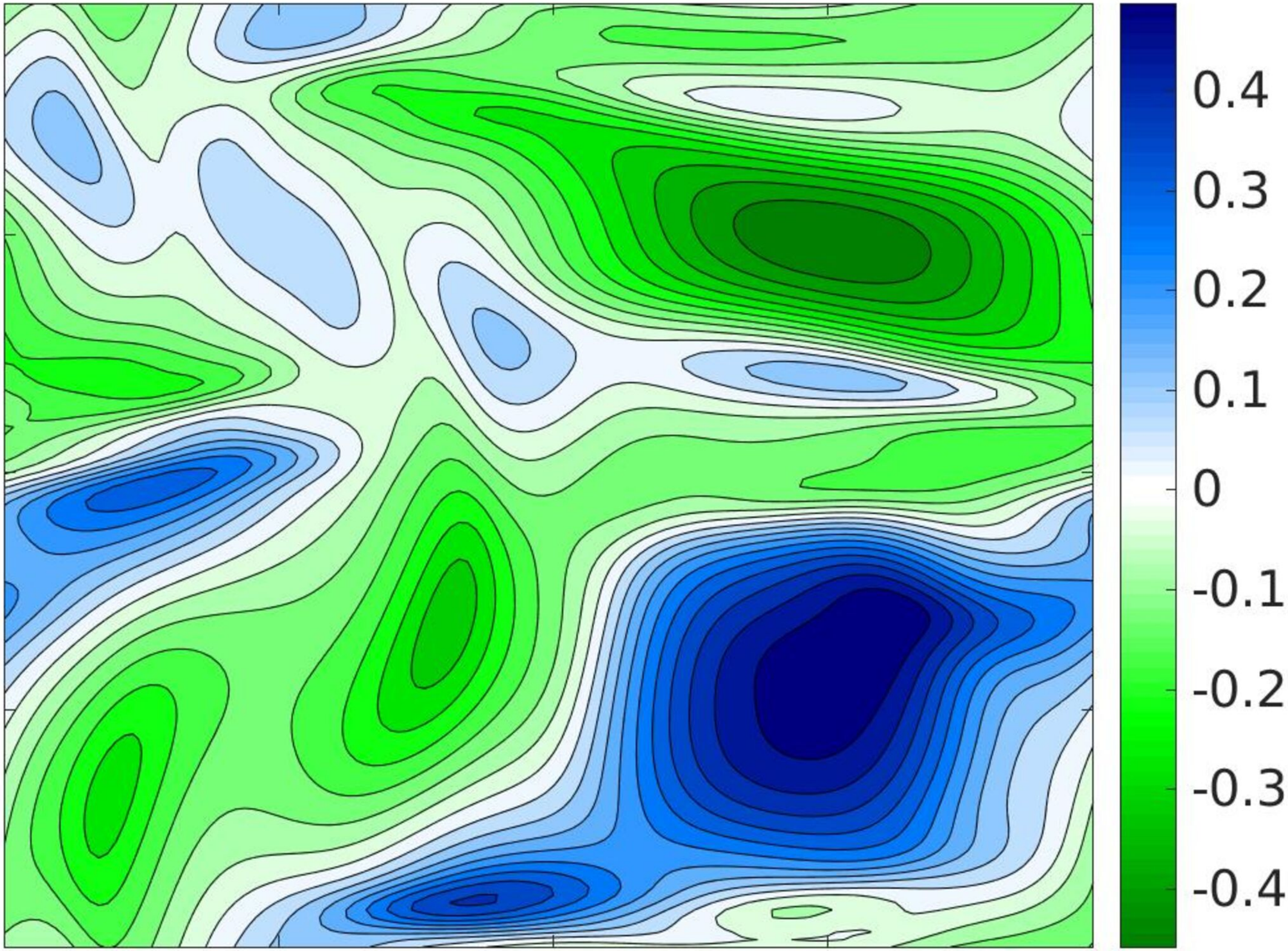

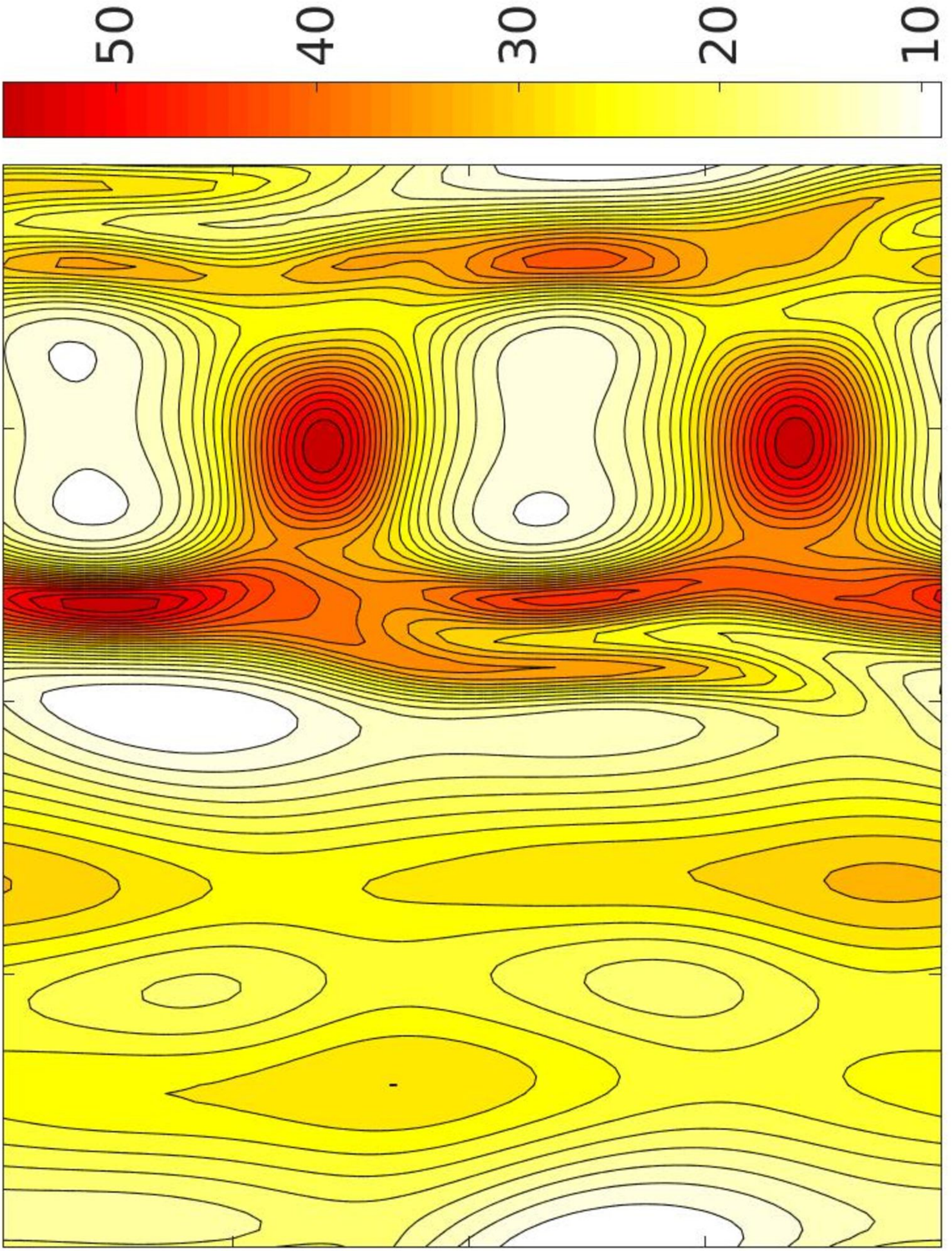
50
40
30
20
10

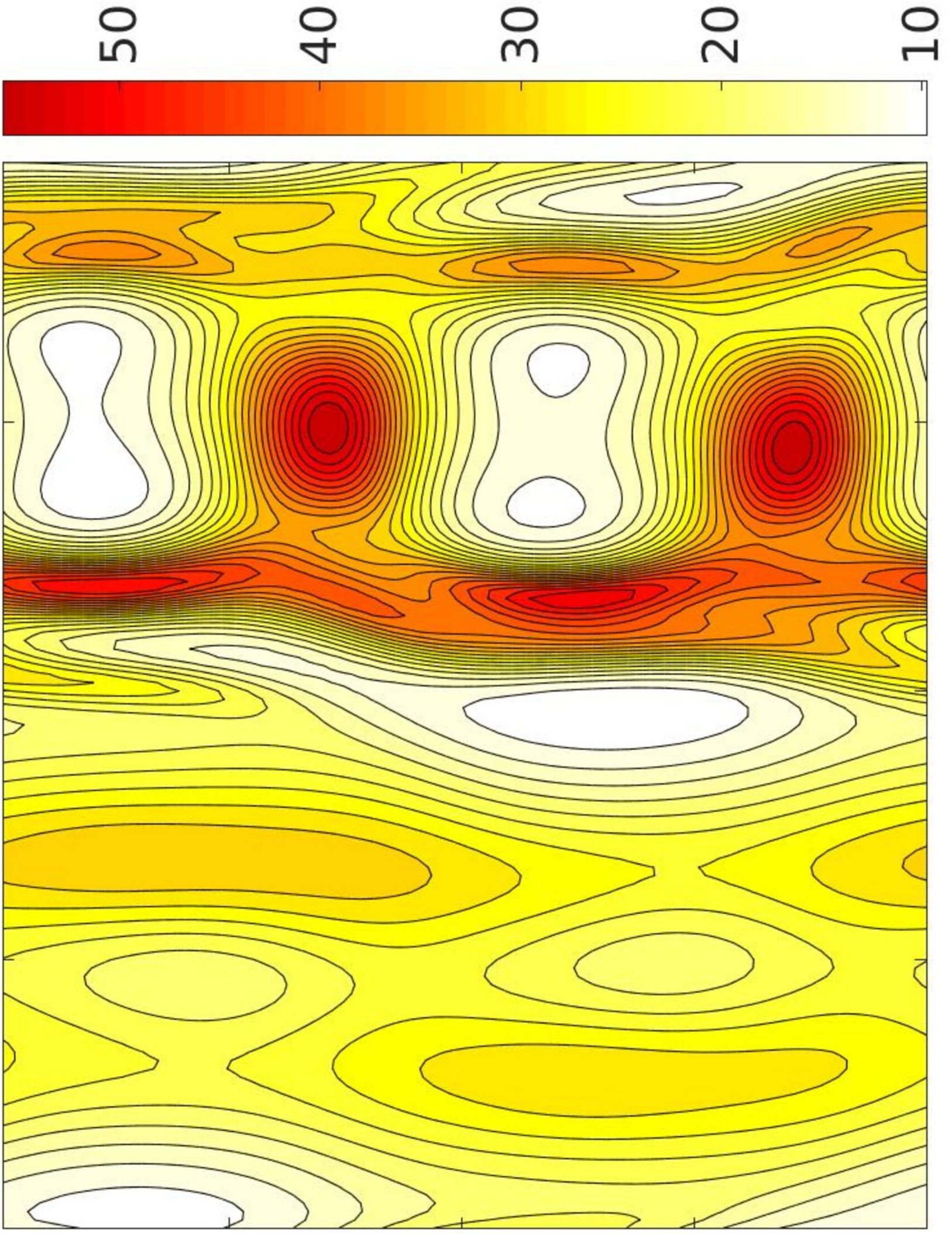
50
40
30
20
10

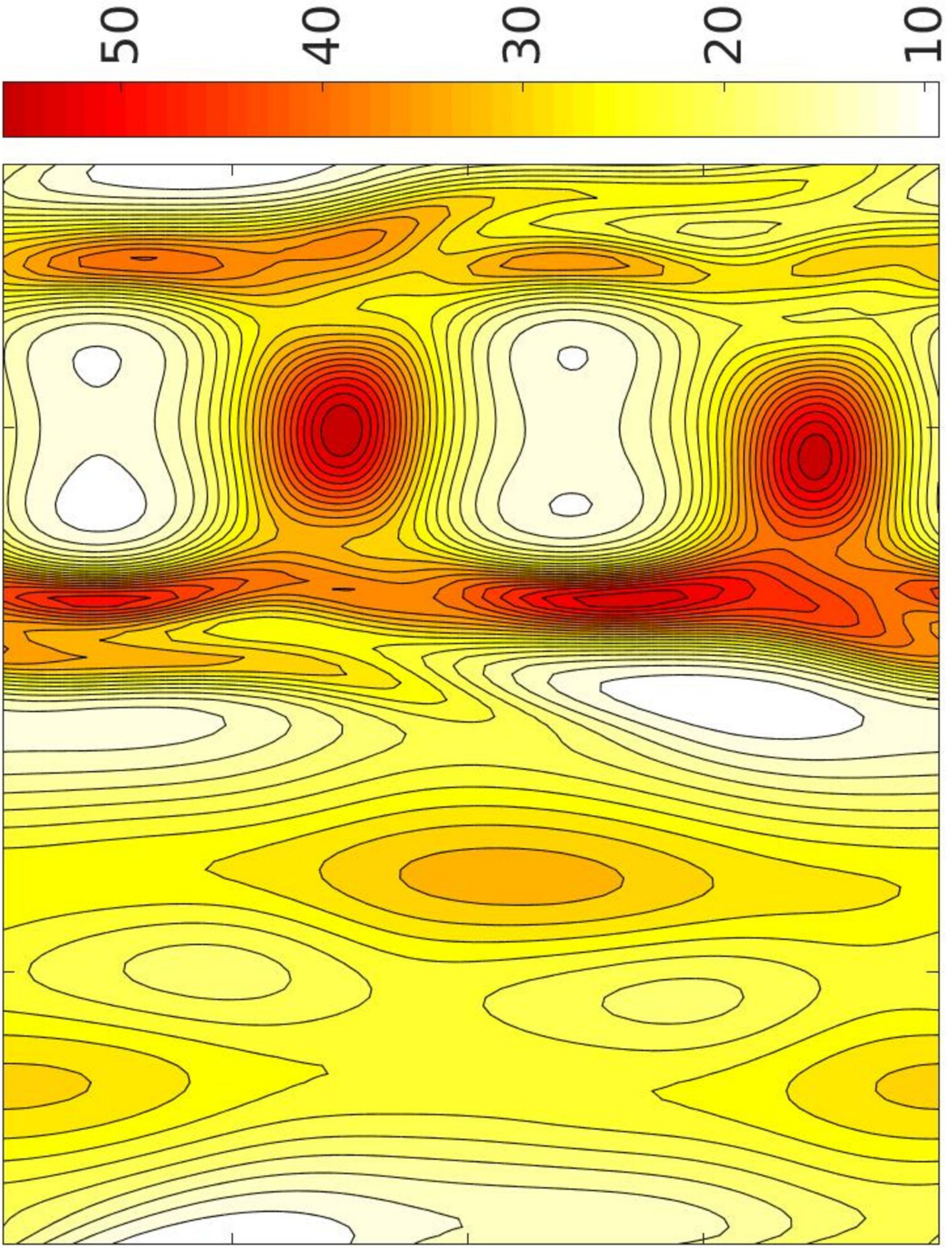
50
40
30
20
10

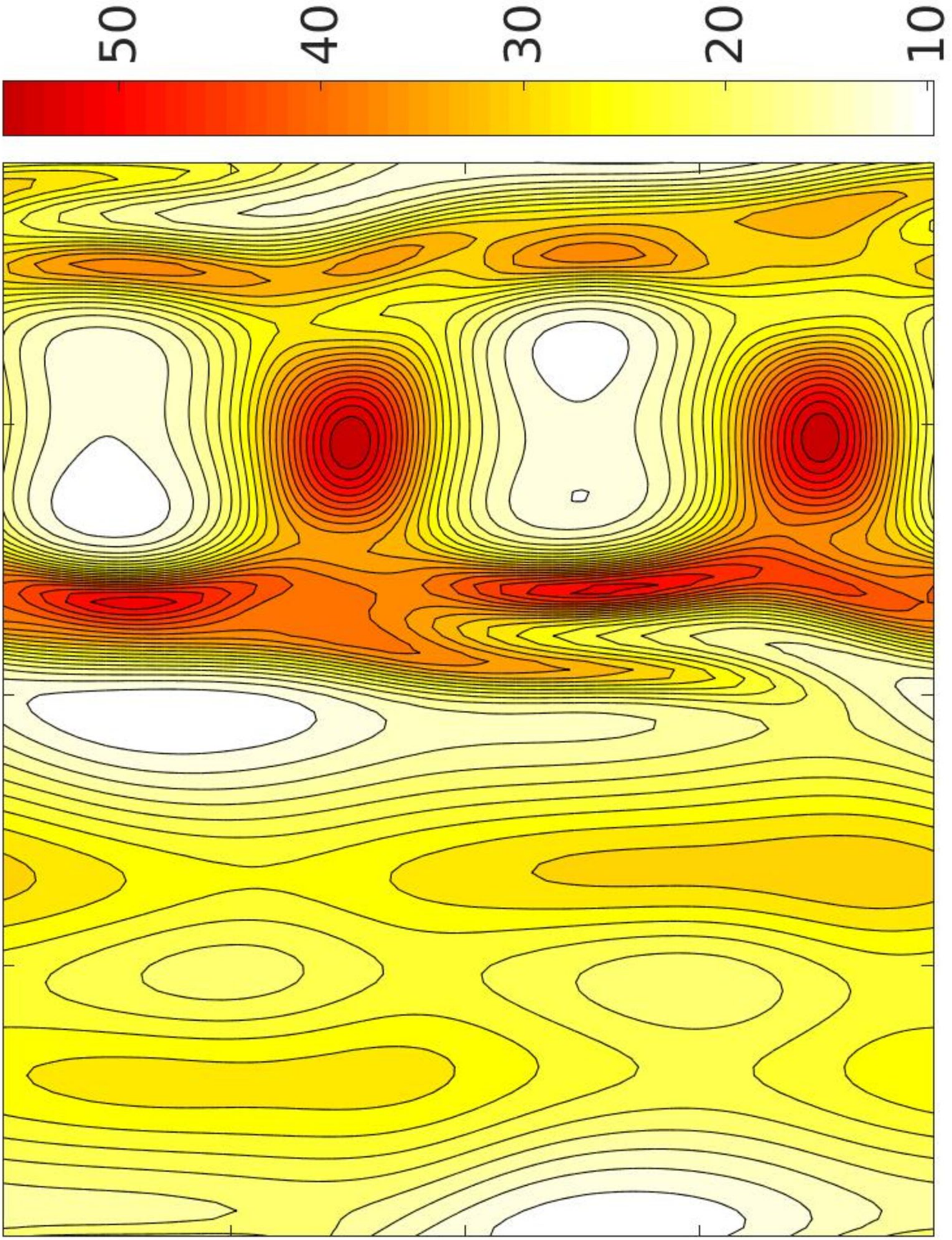
50
40
30
20
10

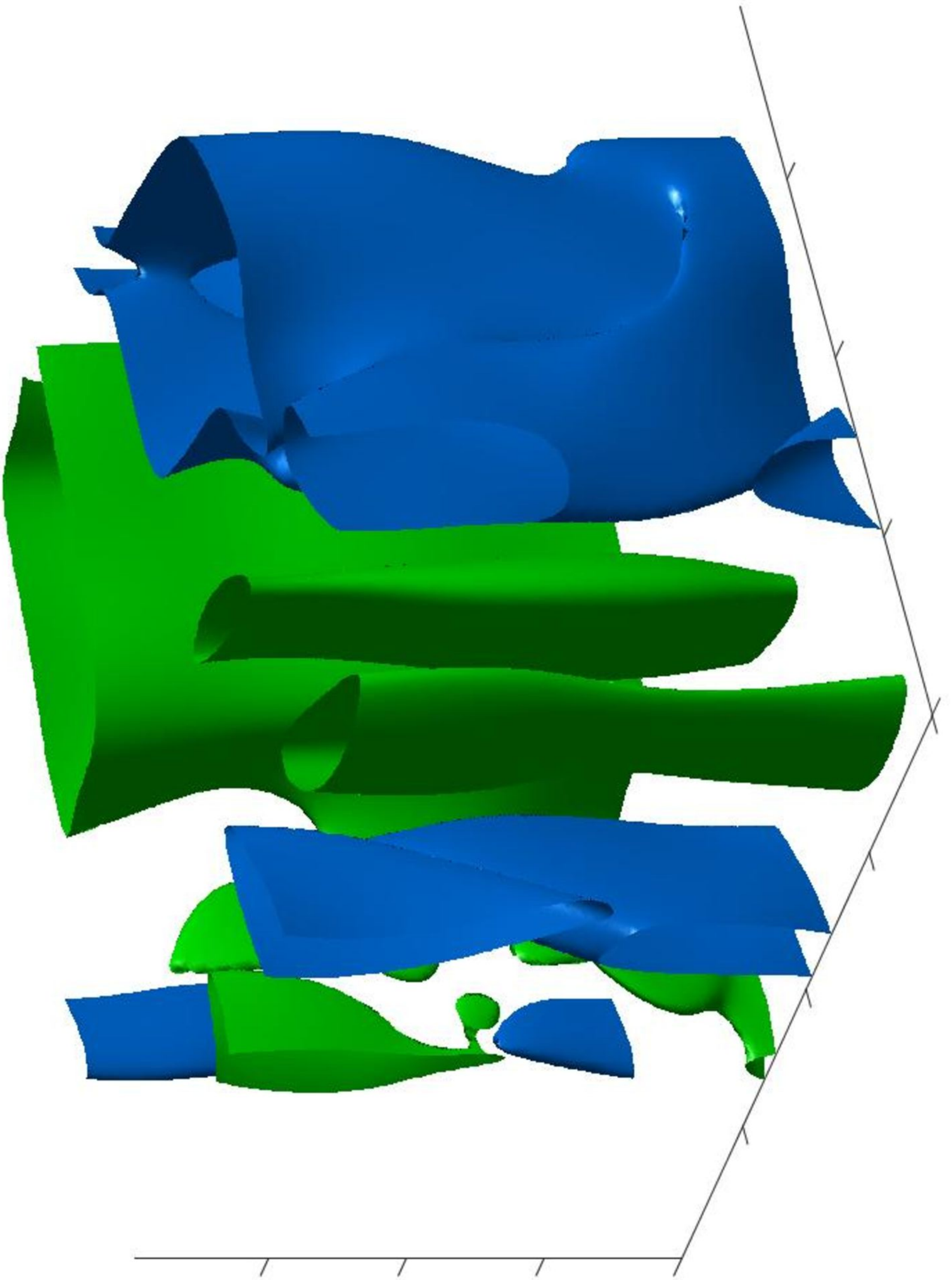

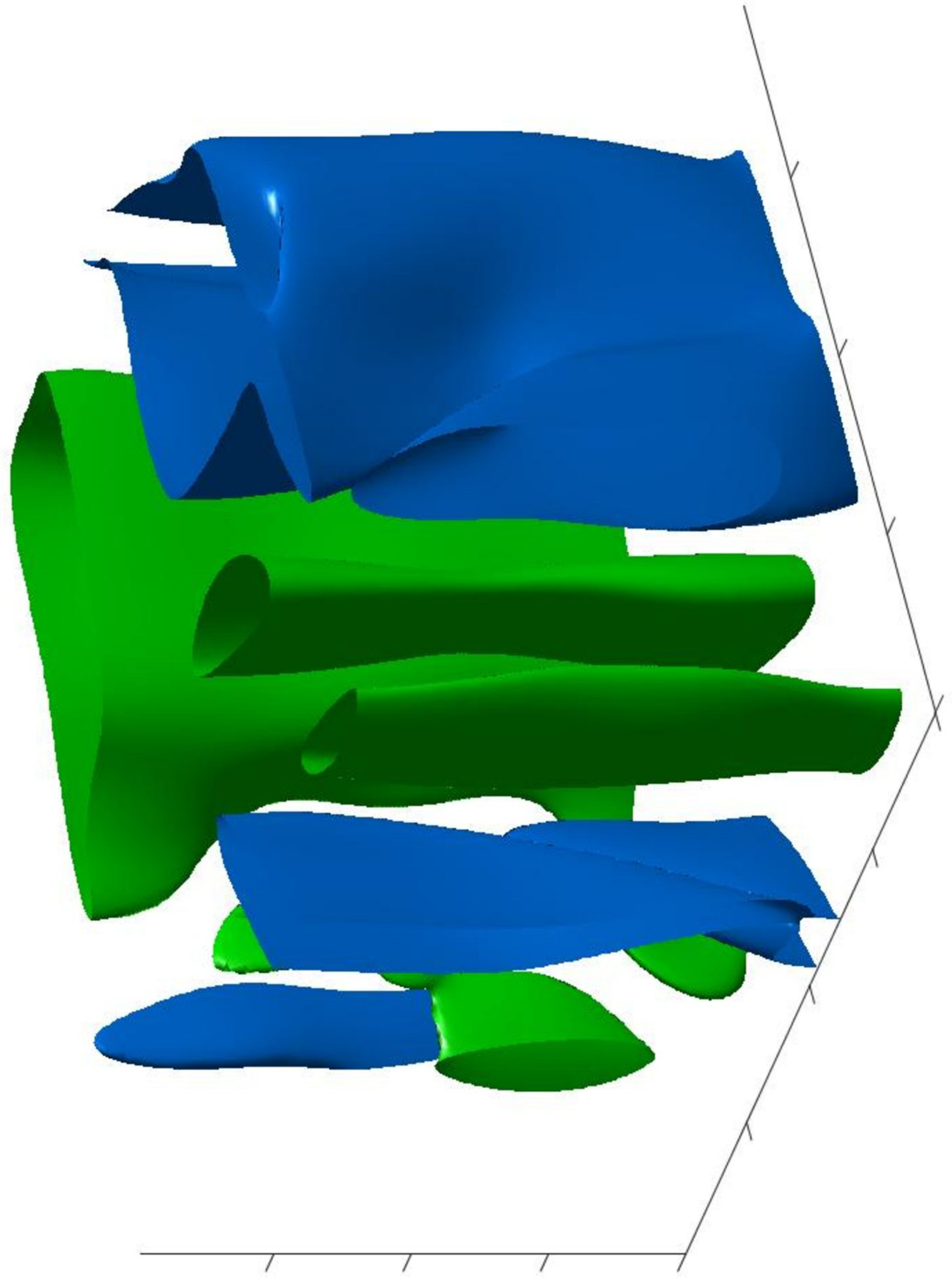

16 December 2024 10:49:31

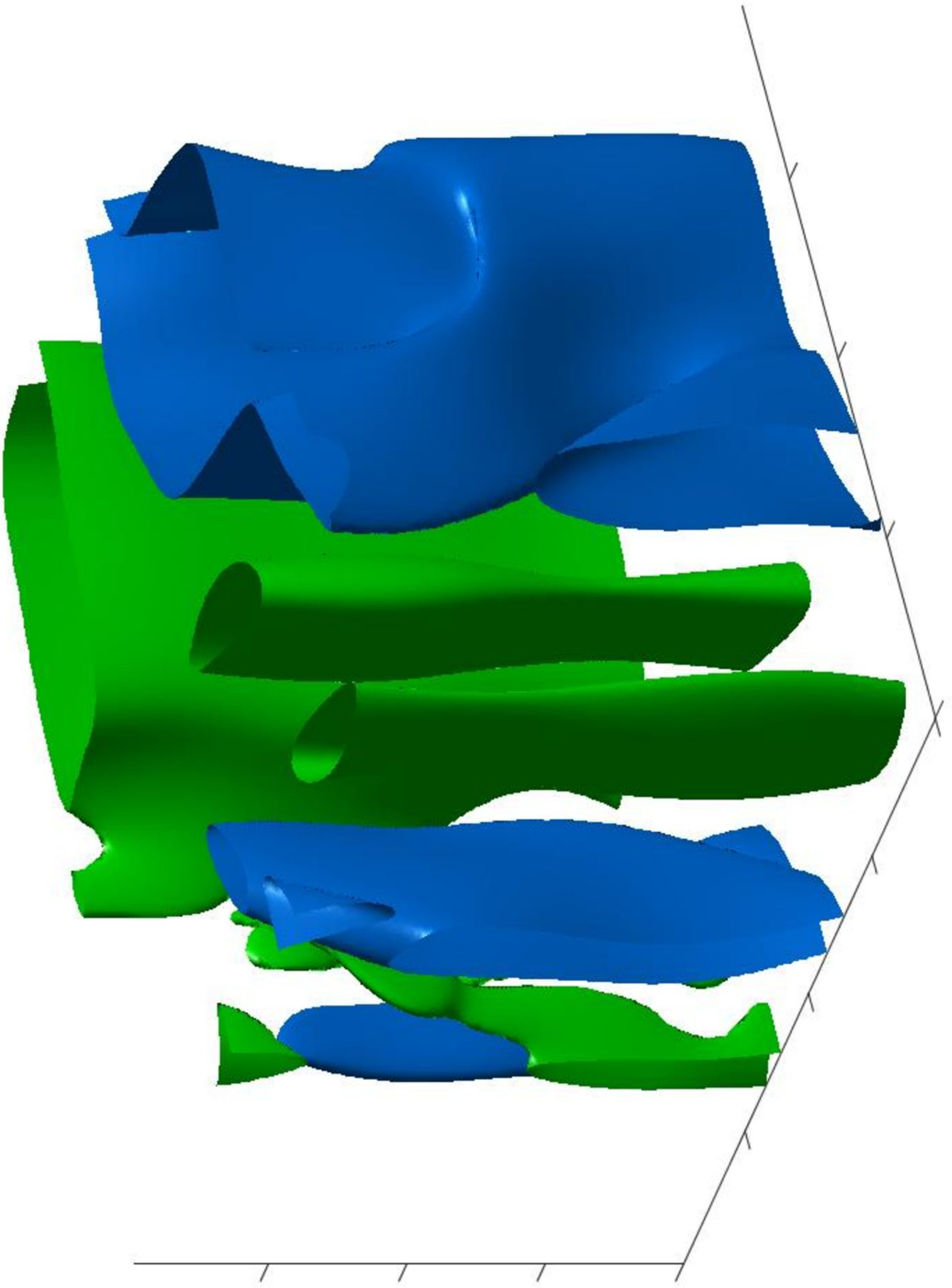

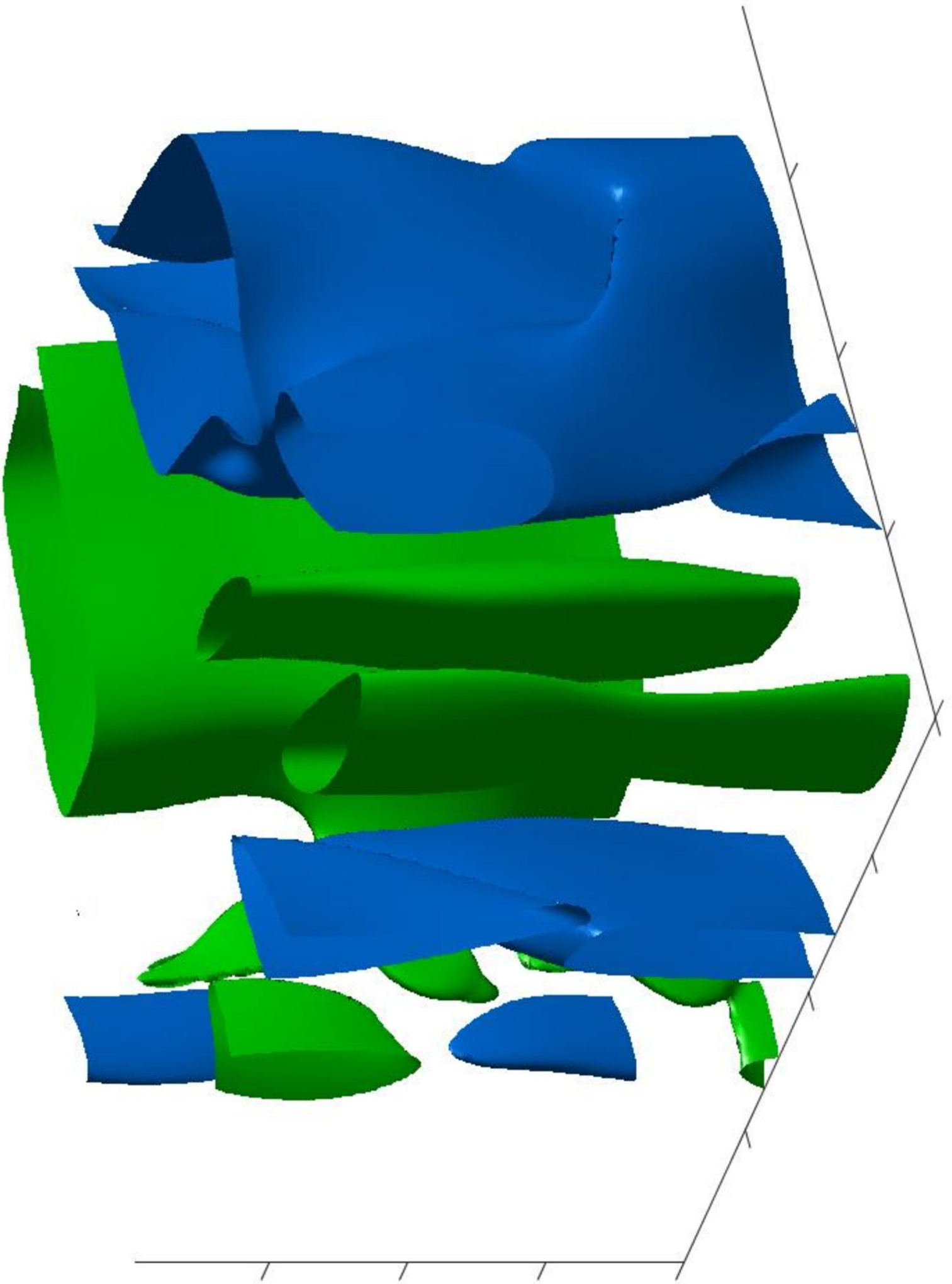

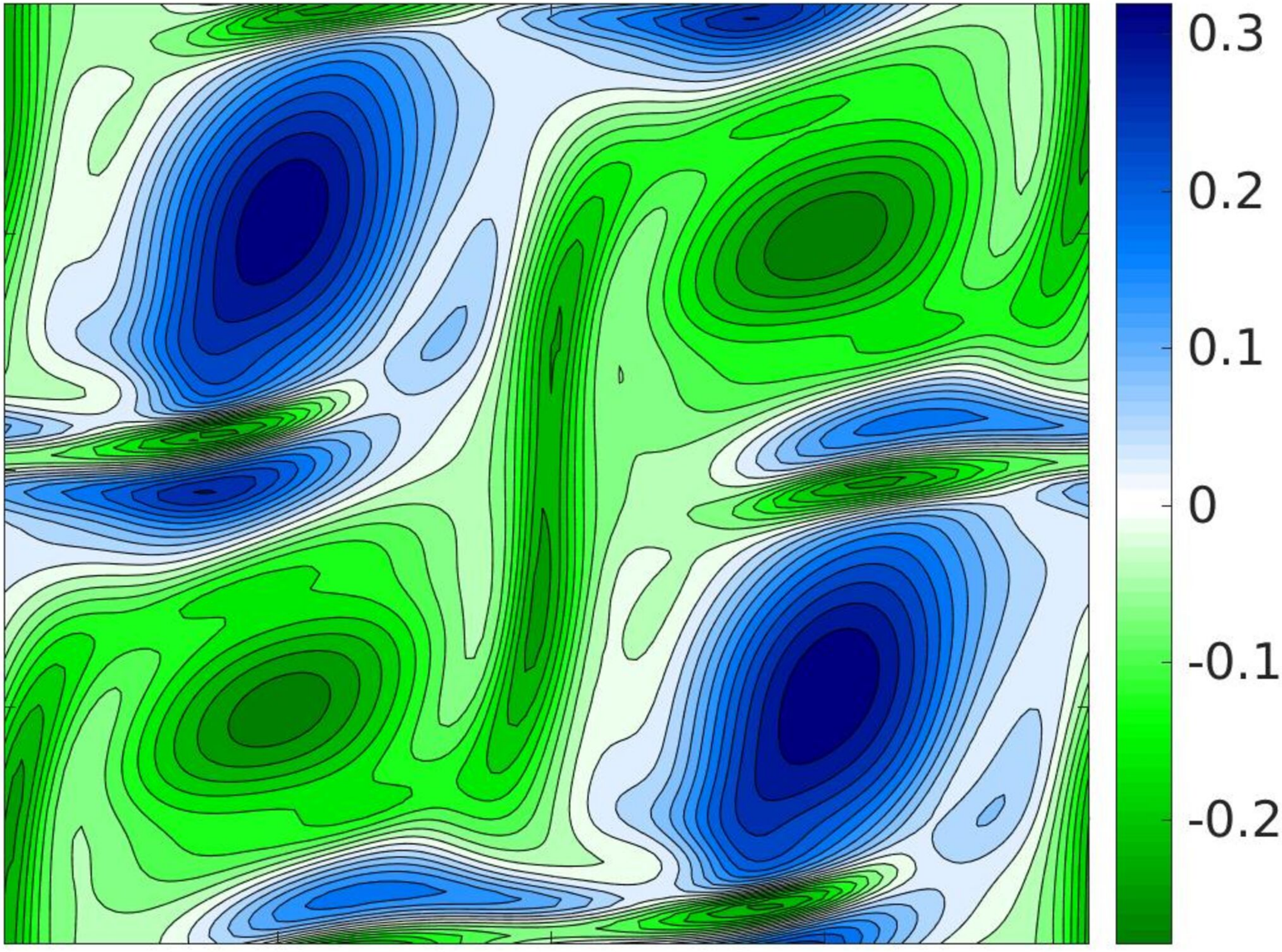

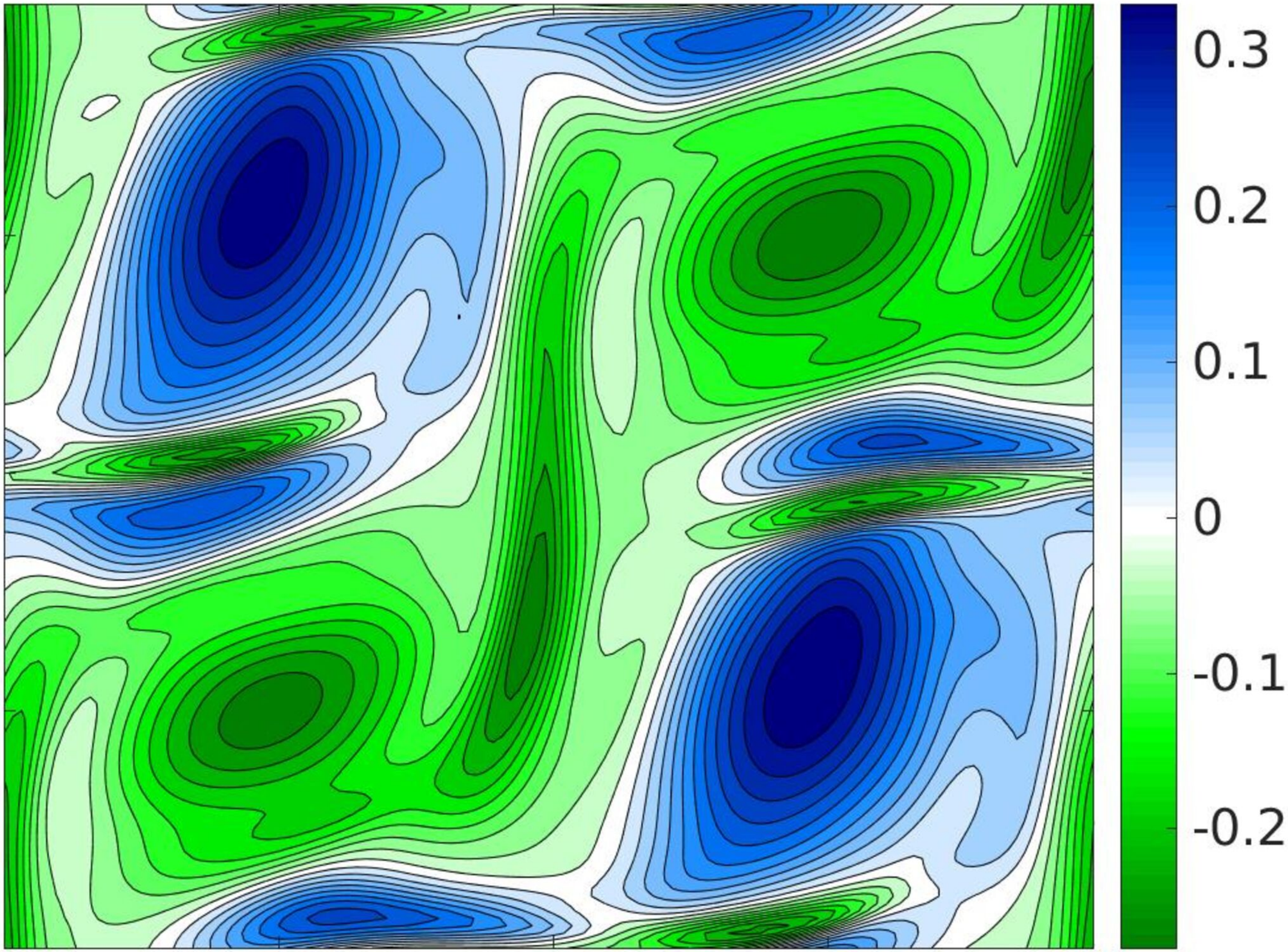

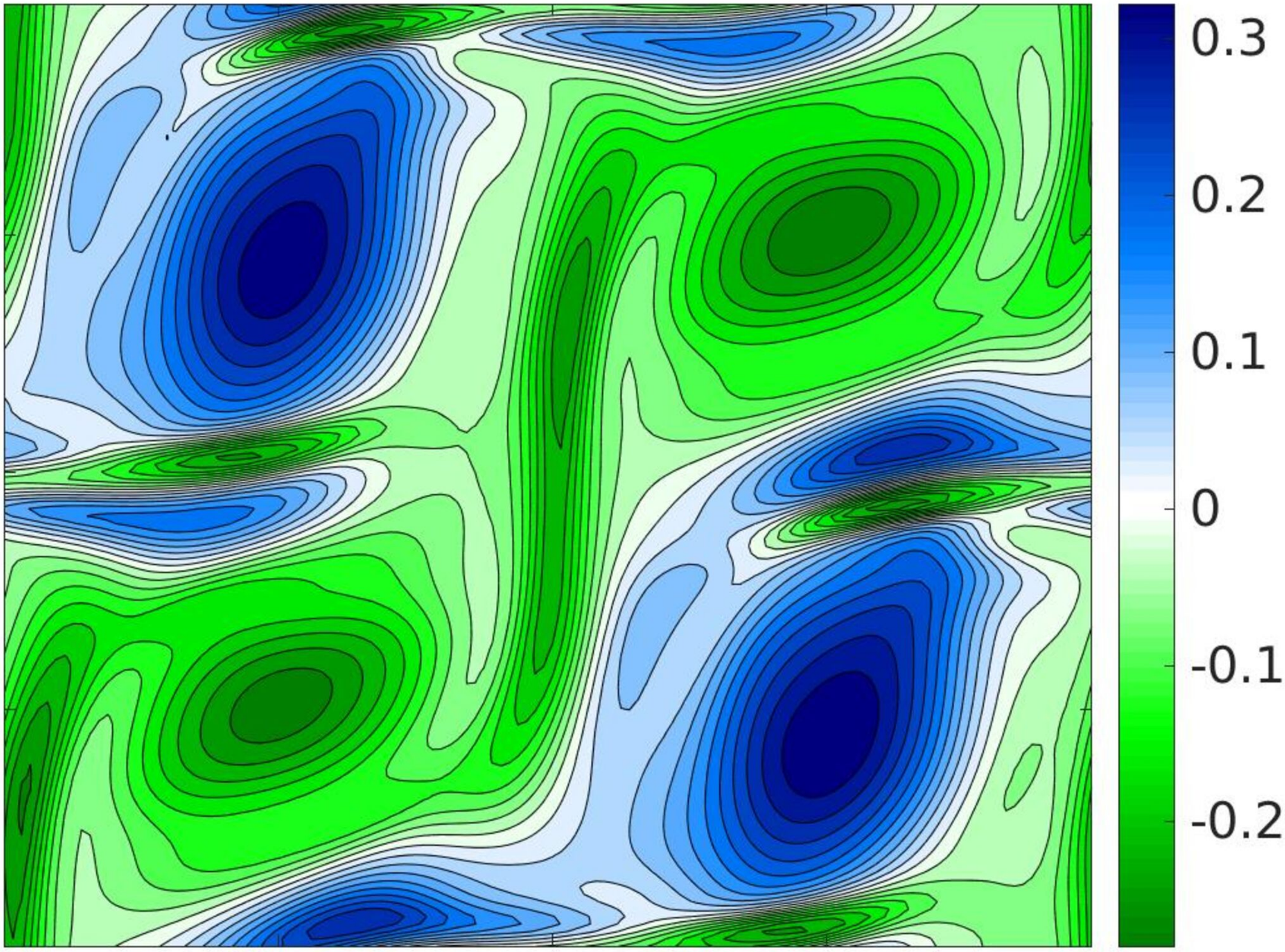

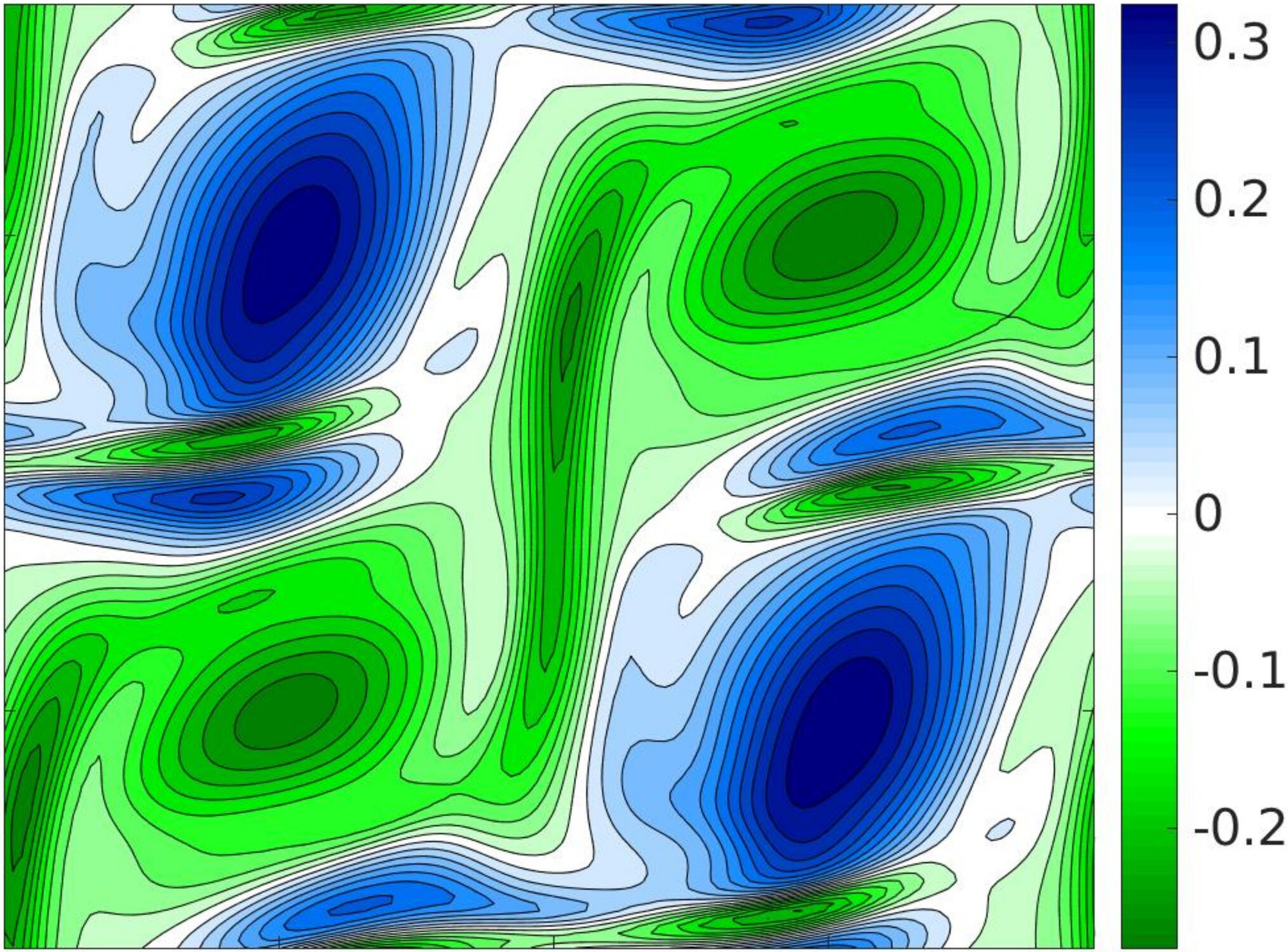

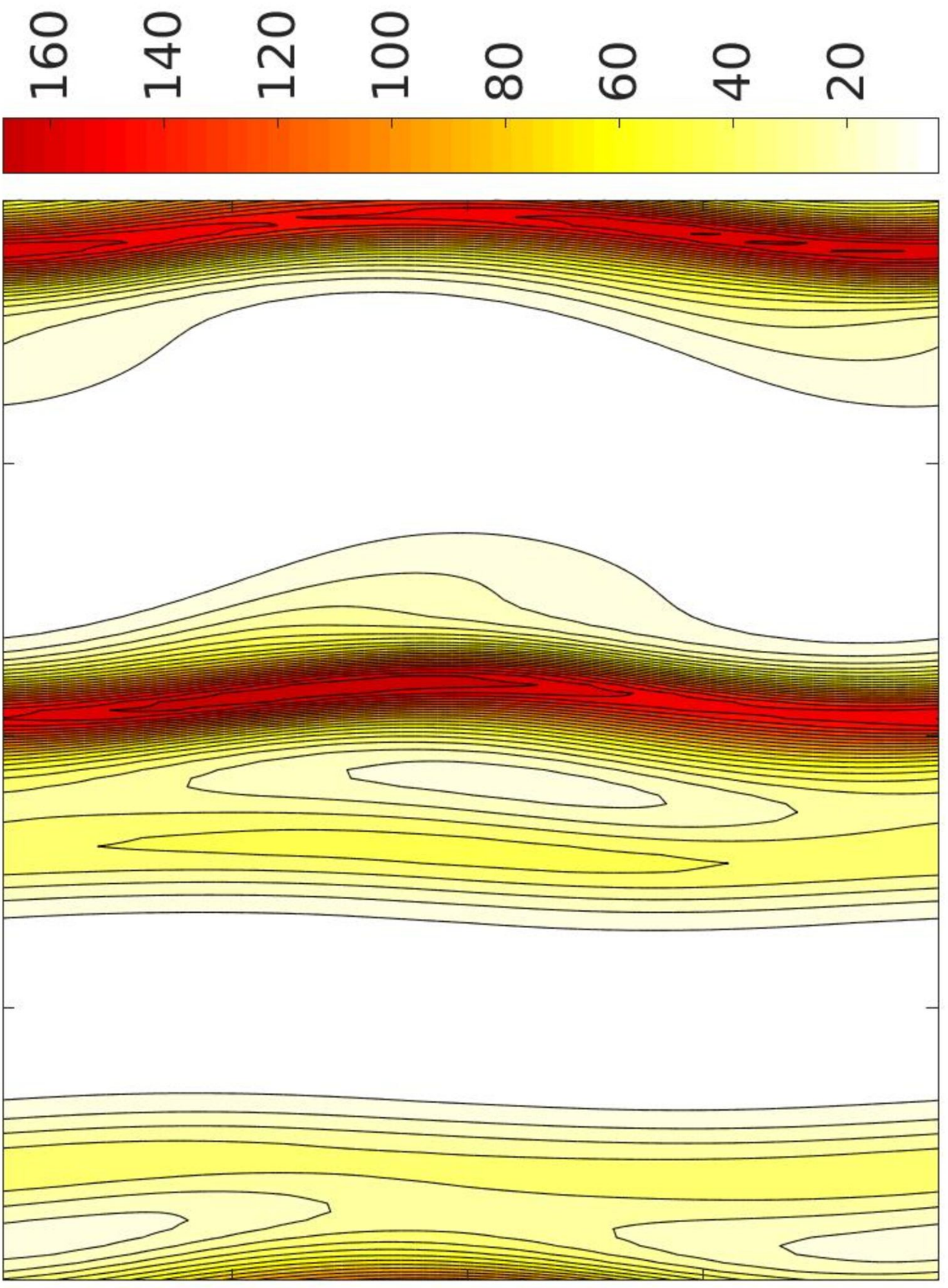
160
140
120
100
80
60
40
20

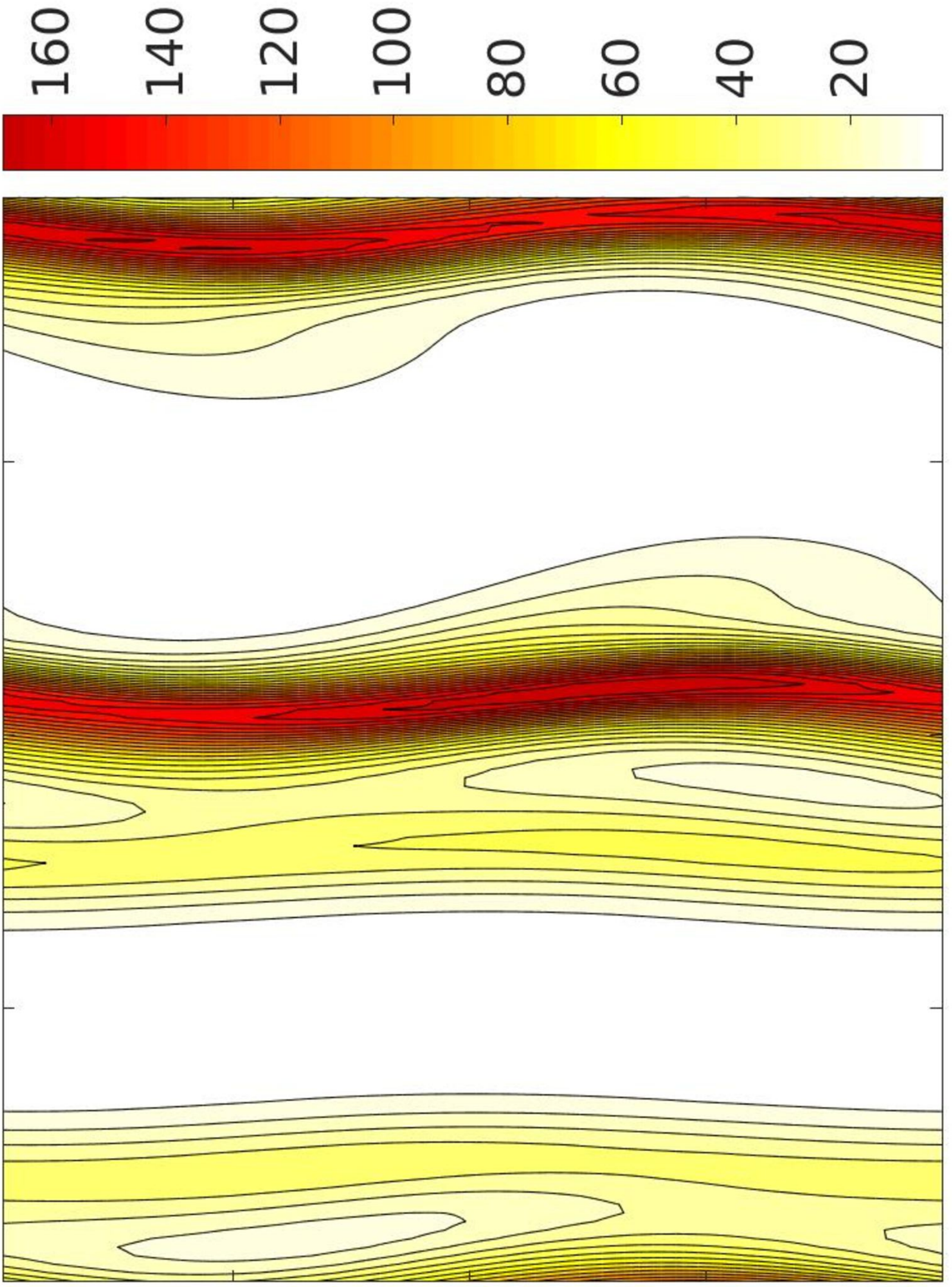
160
140
120
100
80
60
40
20

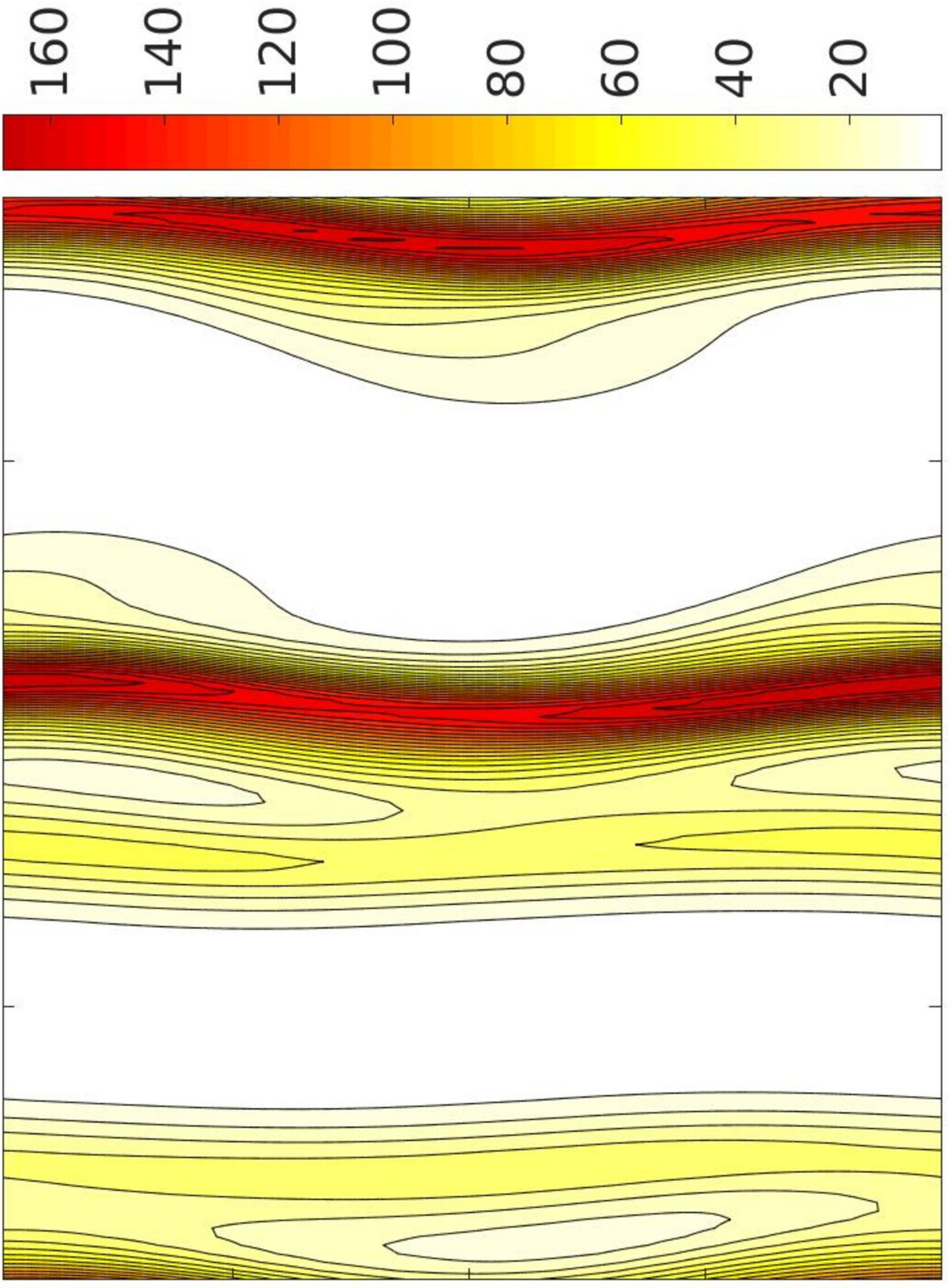
160
140
120
100
80
60
40
20

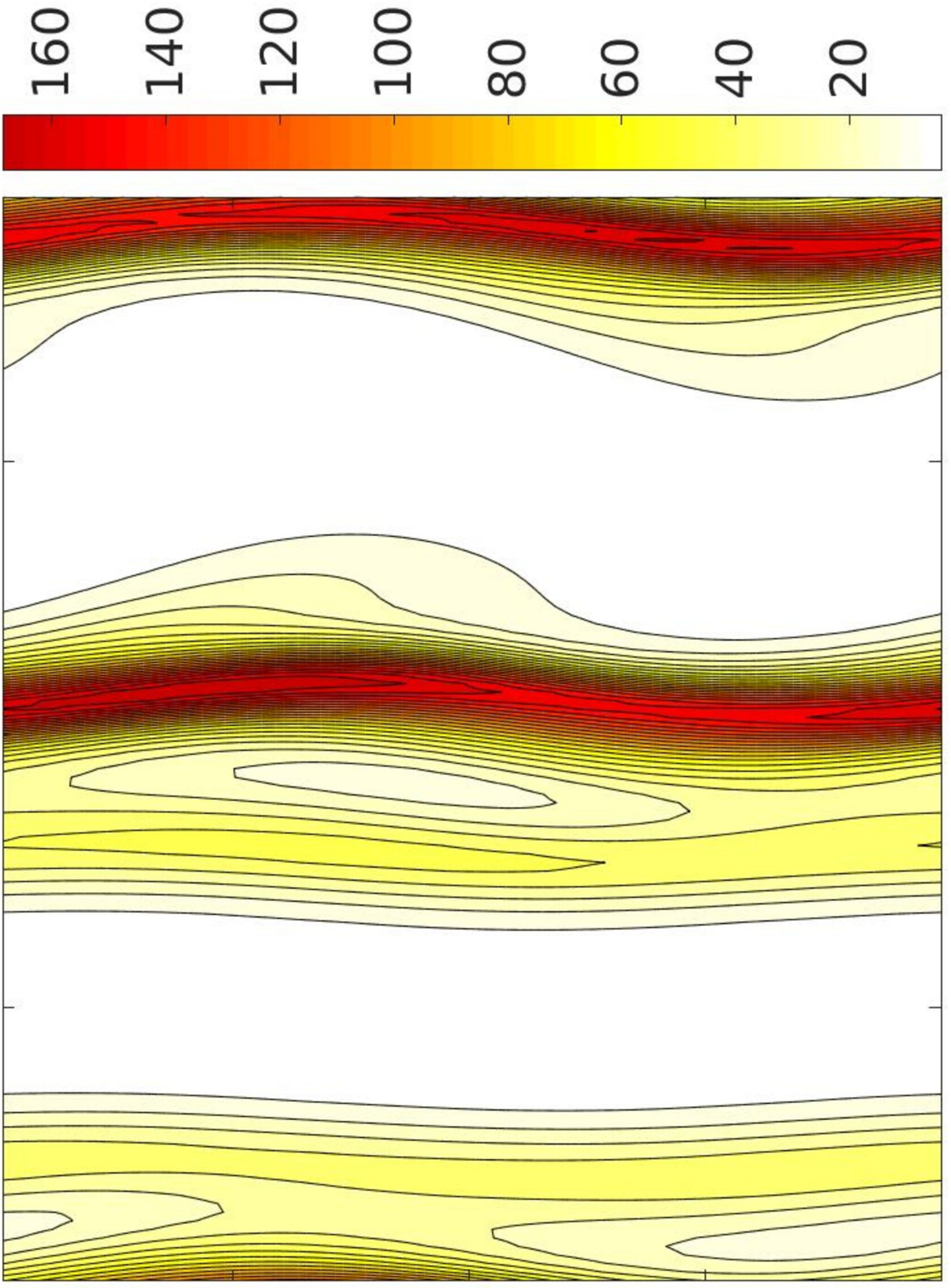
160
140
120
100
80
60
40
20

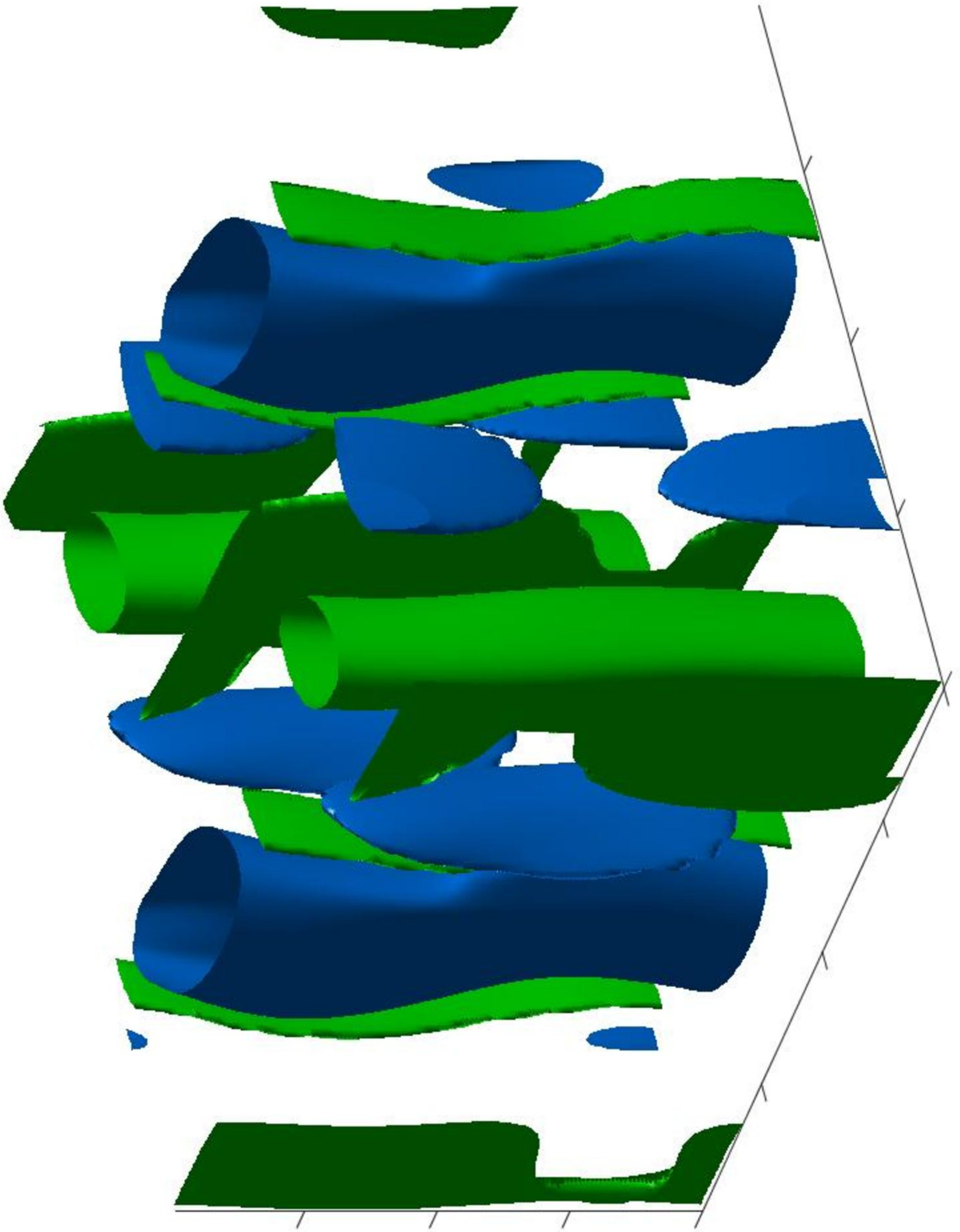

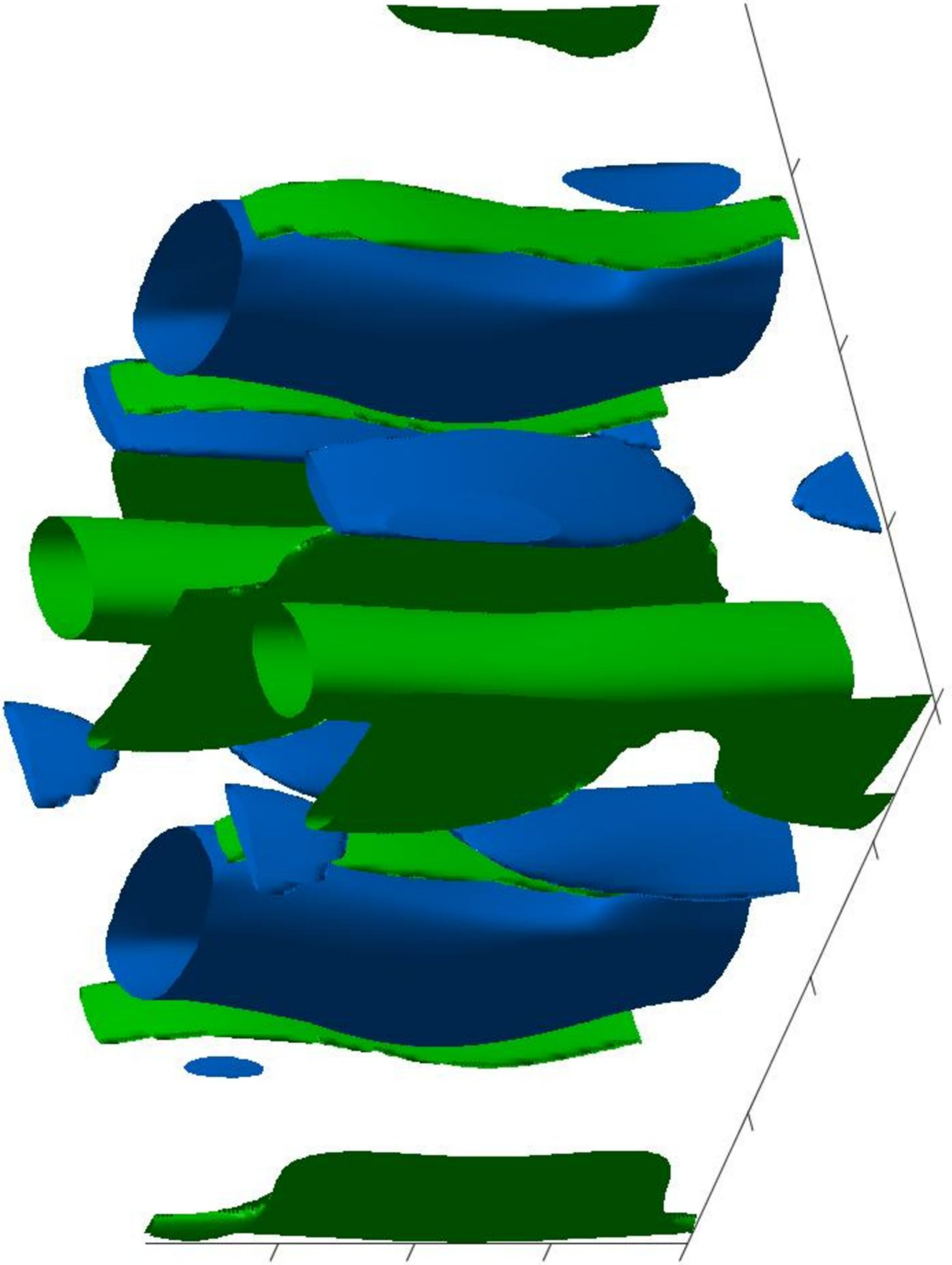

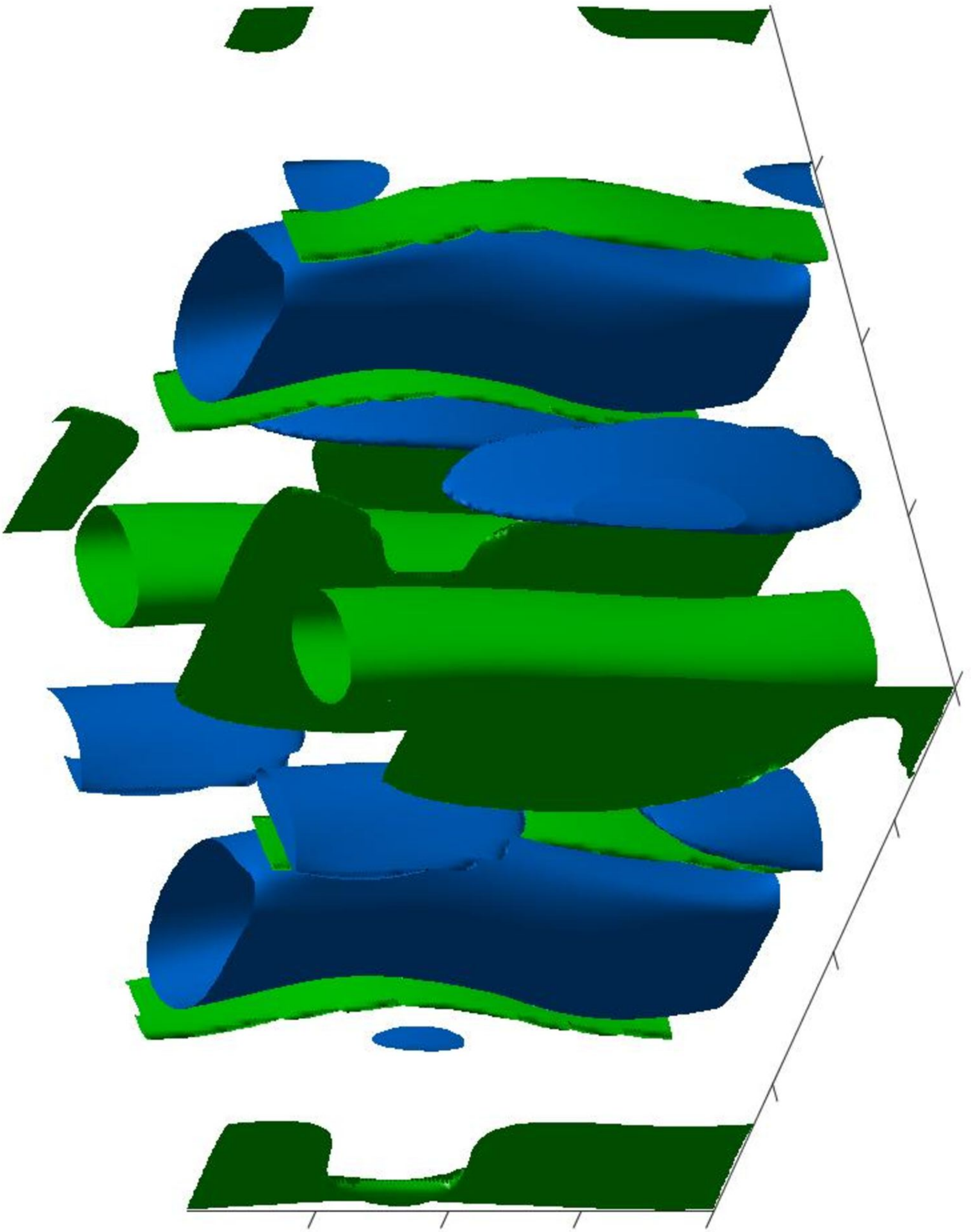

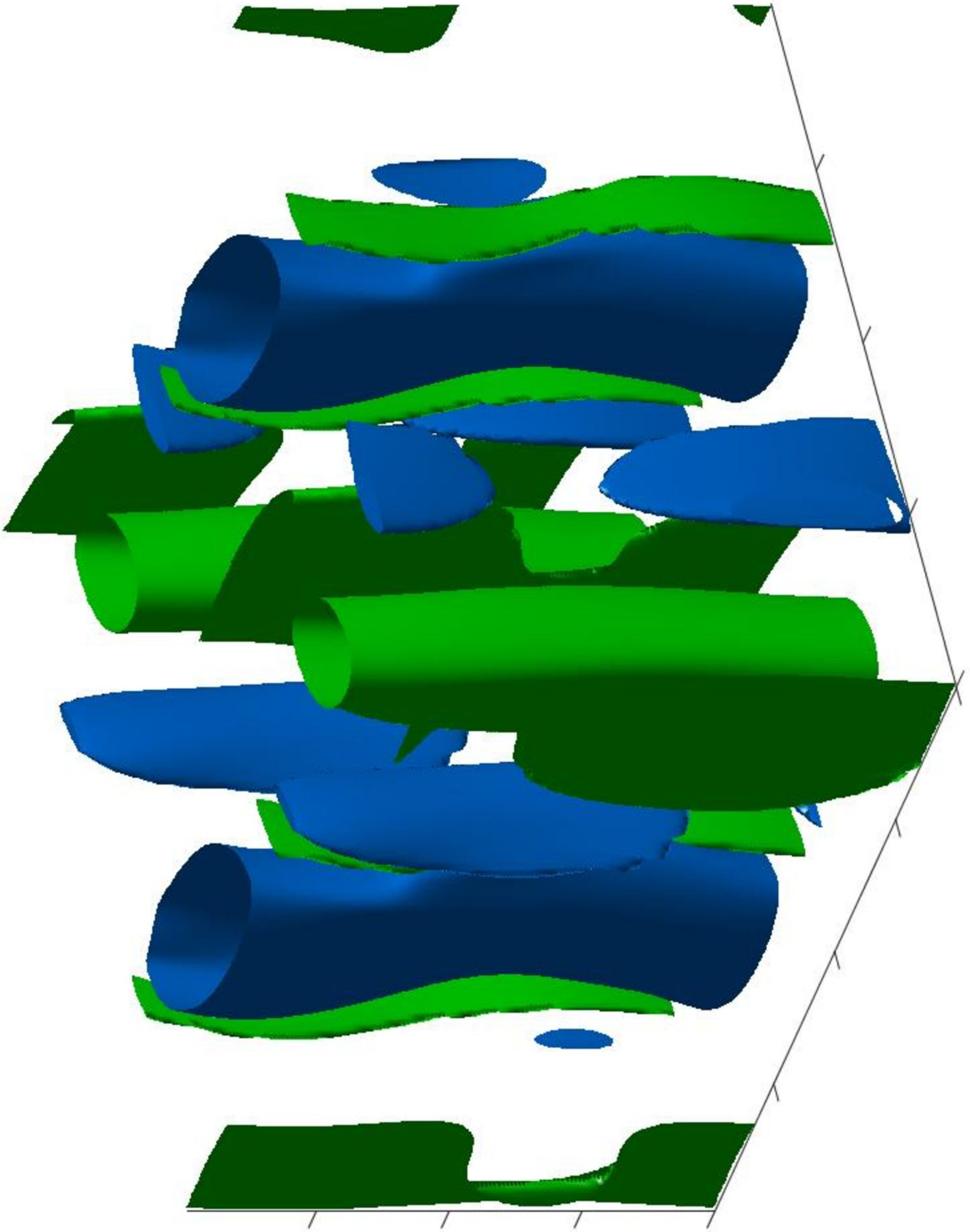

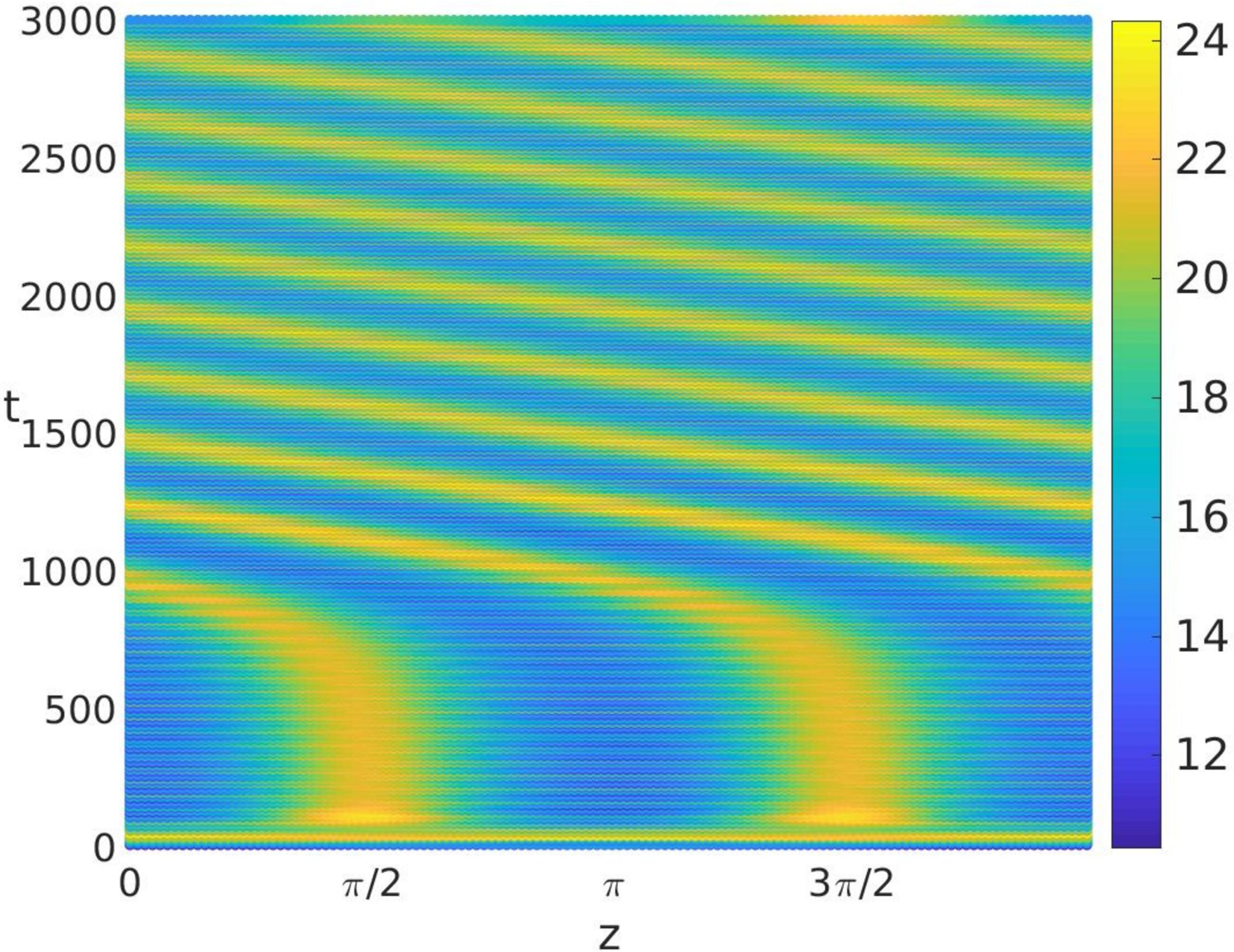

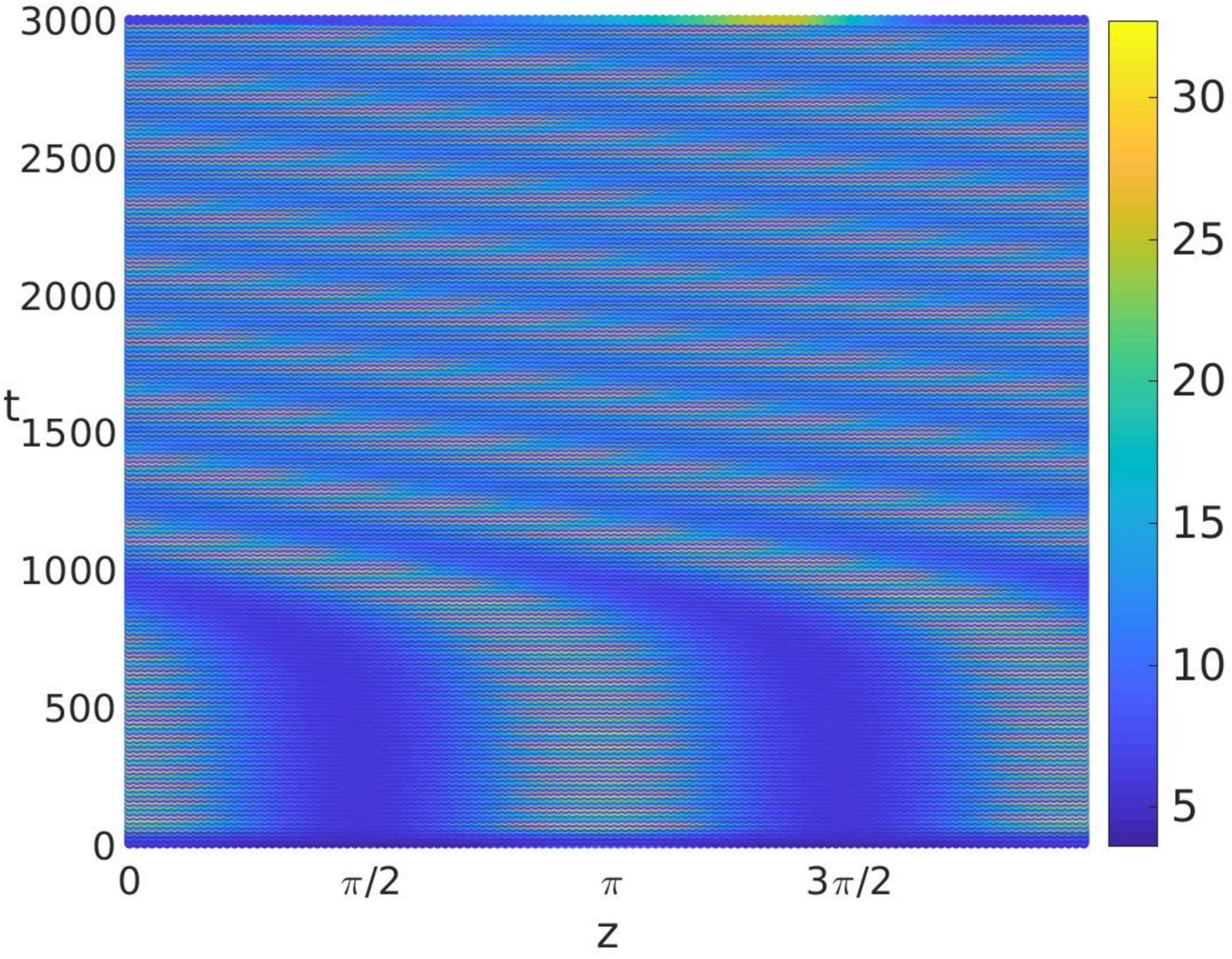

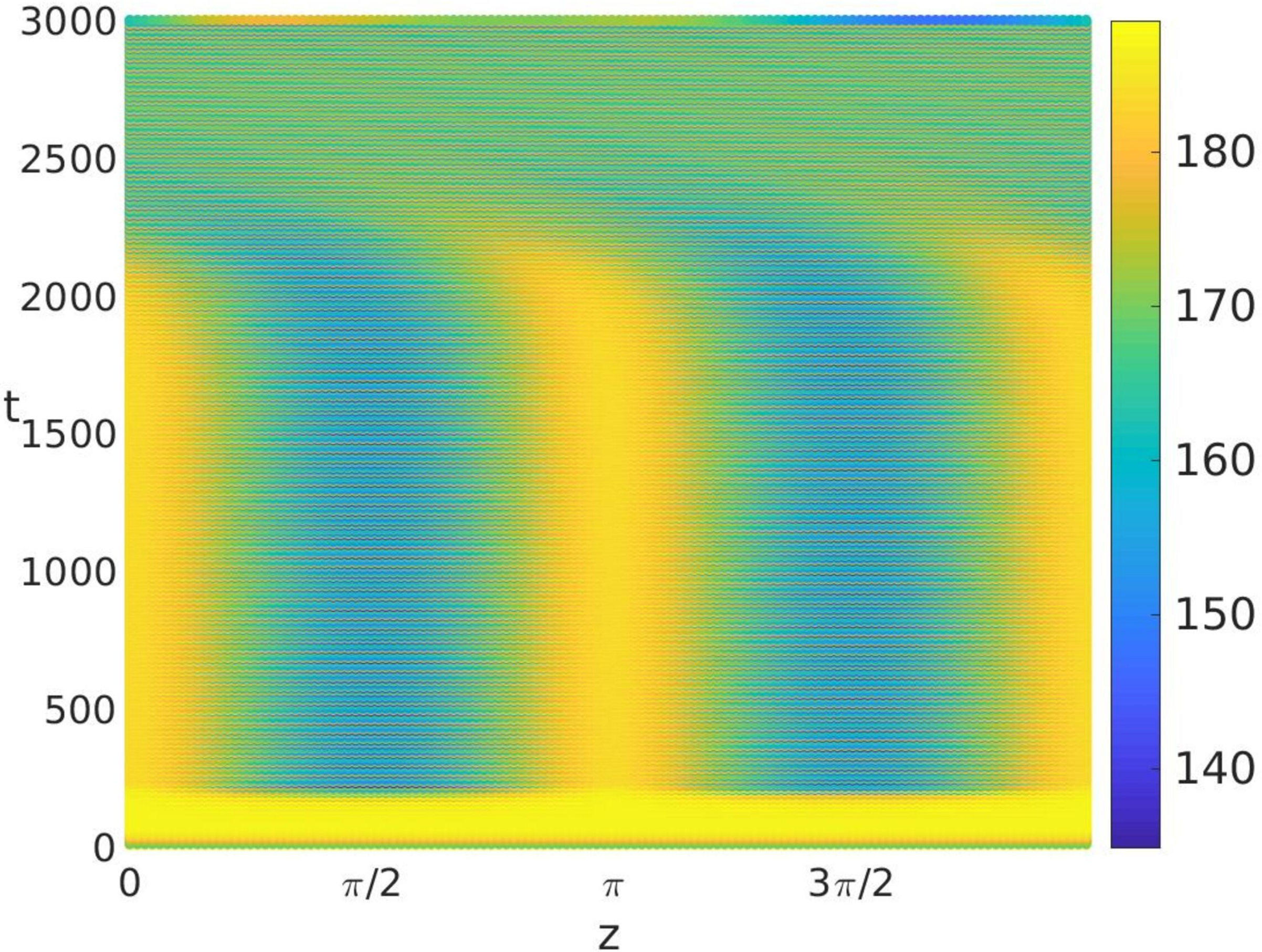

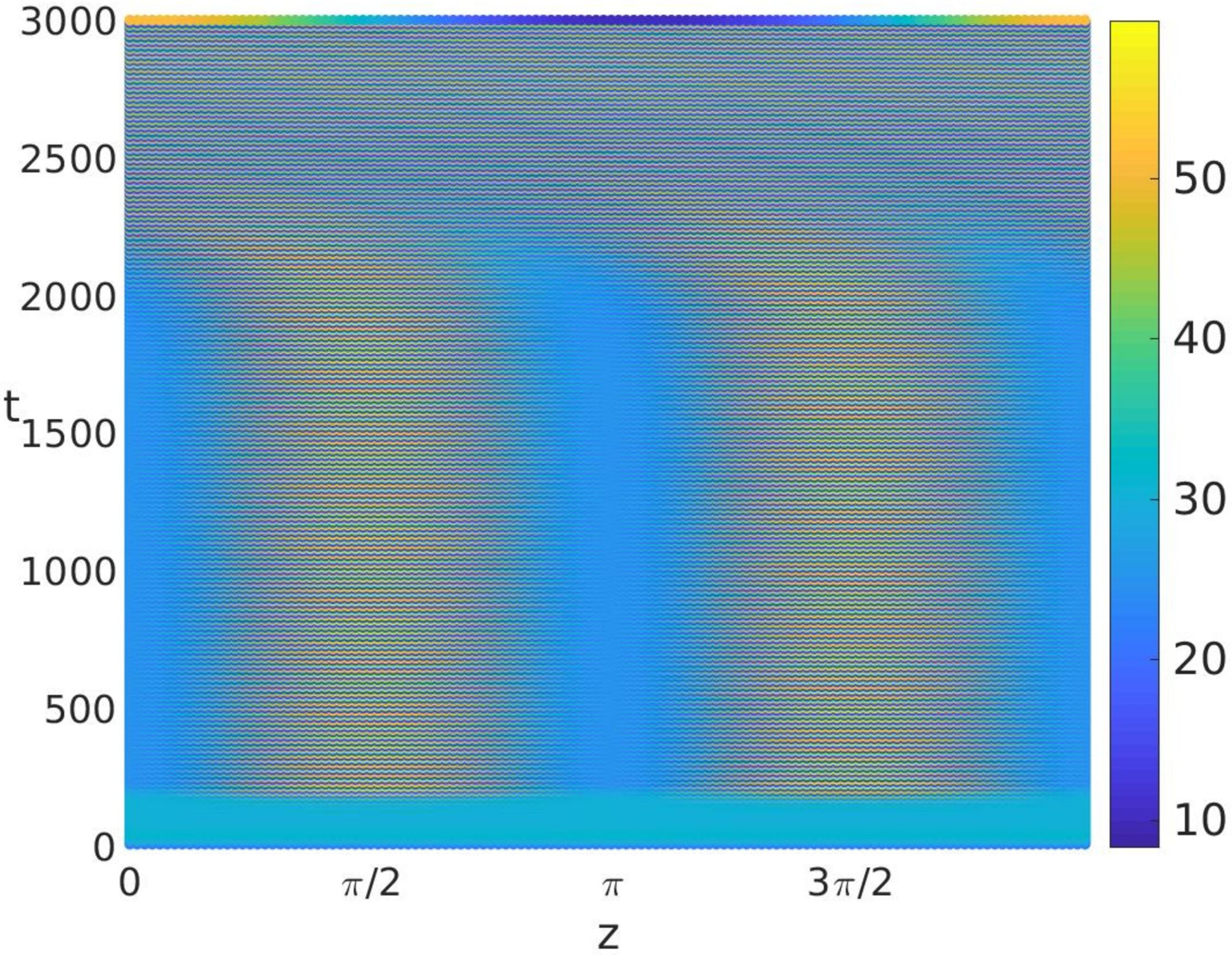

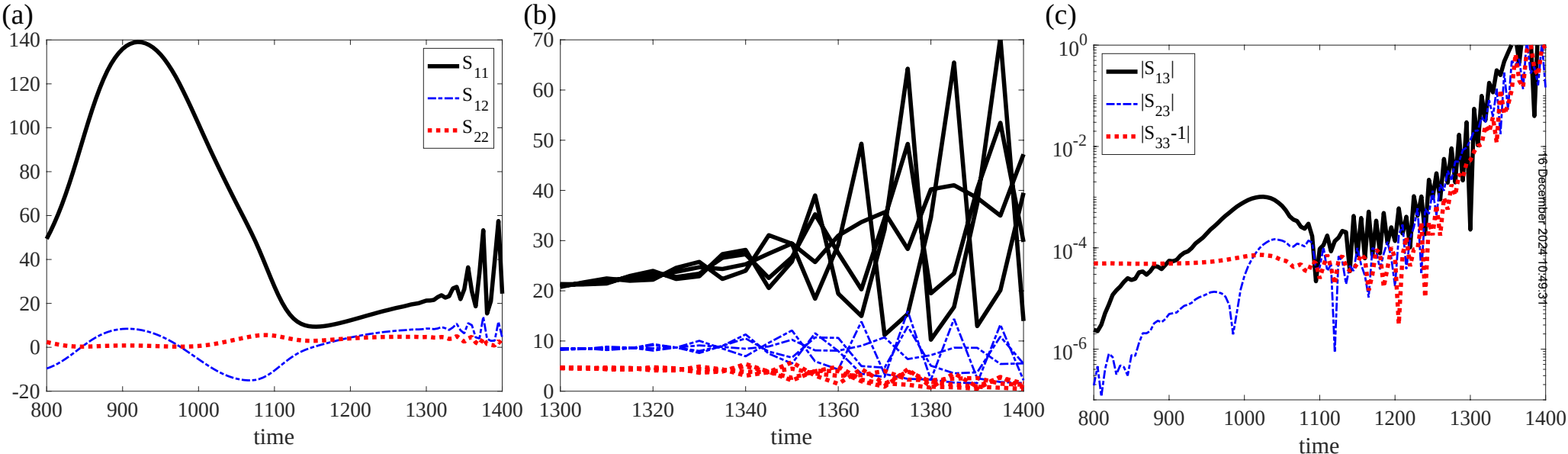
(a)
(b)
(c)
S11
S12
S22
|S13|
|S23|
|S33-1|
time
time
time
16 December 2024 10:49:31

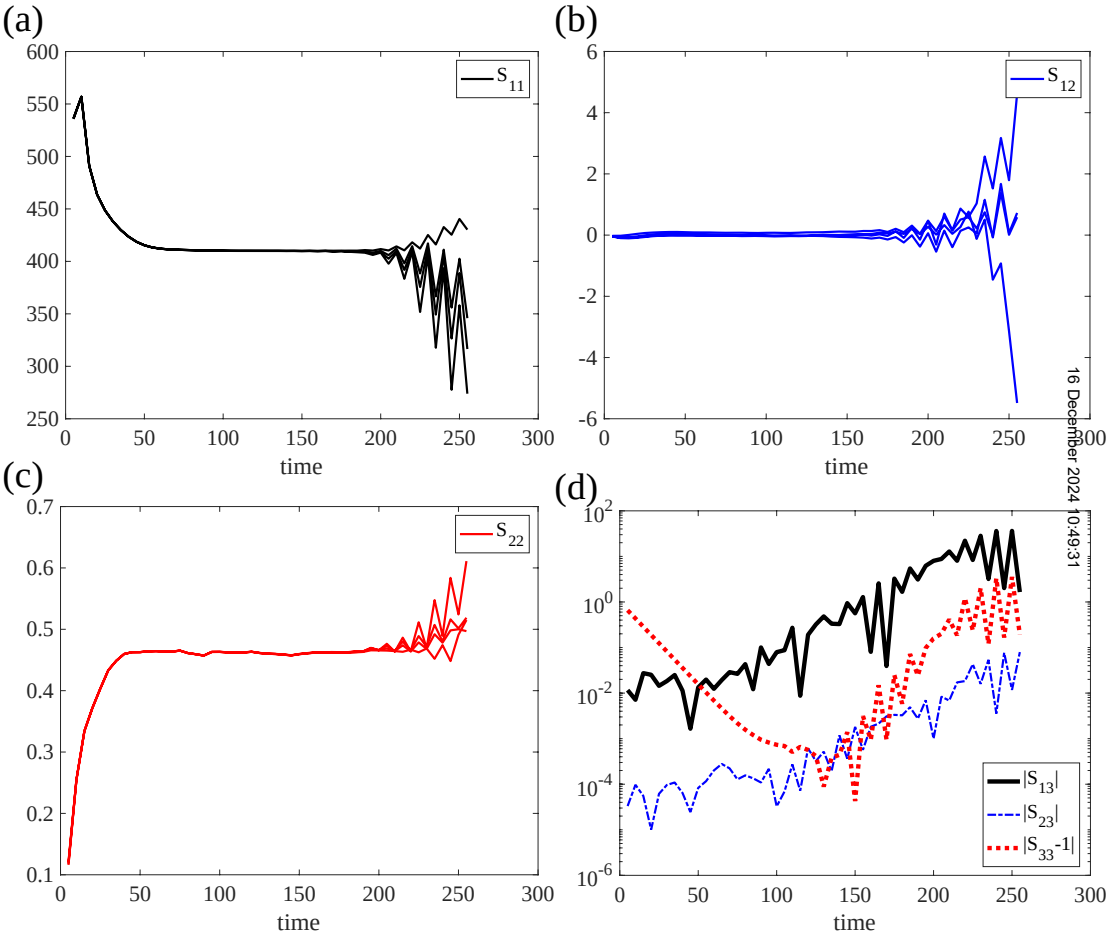
(a)
S11
time
(b)
S12
time
16 December 2024 10:49:31
(c)
S22
time
(d)
|S13|
|S23|
|S33-1|
time

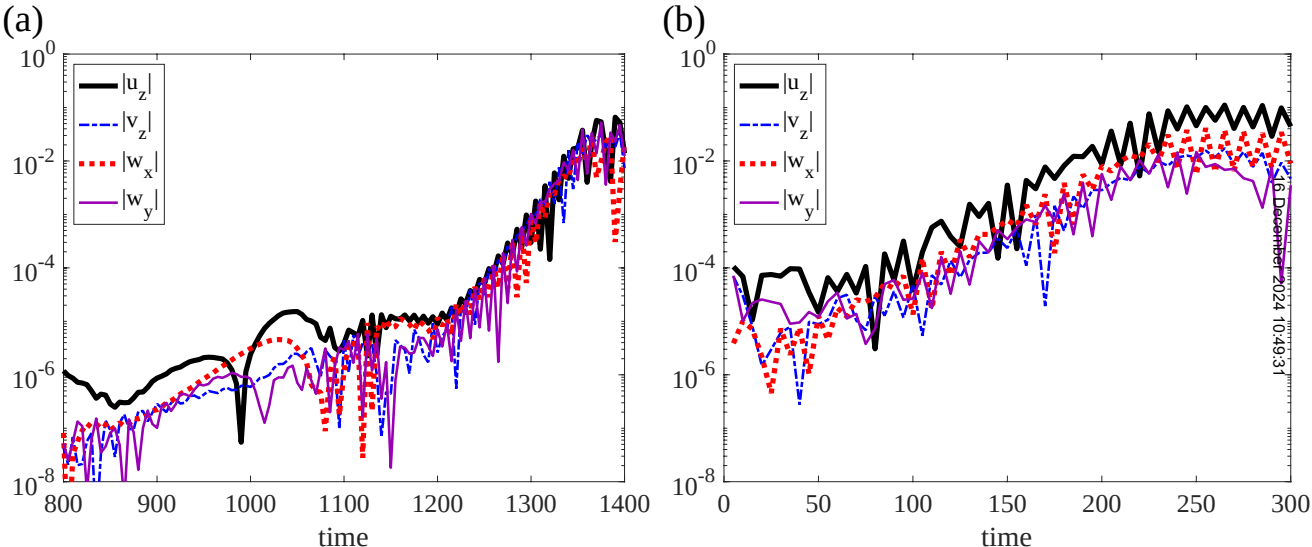
(a)
(b)
10^0
10^{-2}
10^{-4}
10^{-6}
10^{-8}
$|u_z|$
$|v_z|$
$|w_x|$
$|w_y|$
800
900
1000
1100
1200
1300
1400
0
50
100
150
200
250
300
time
16 December 2024 10:49:31

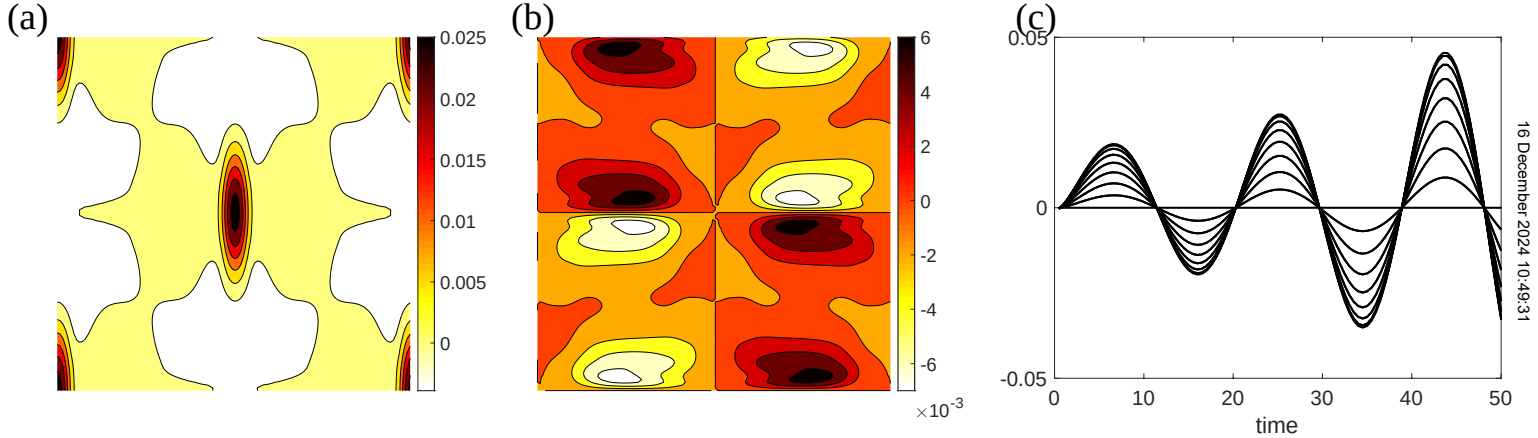
(a)
0.025
0.02
0.015
0.01
0.005
0
(b)
6
4
2
0
-2
-4
-6
×10^-3
(c)
0.05
0
-0.05
0
10
20
30
40
50
time
16 December 2024 10:49:31

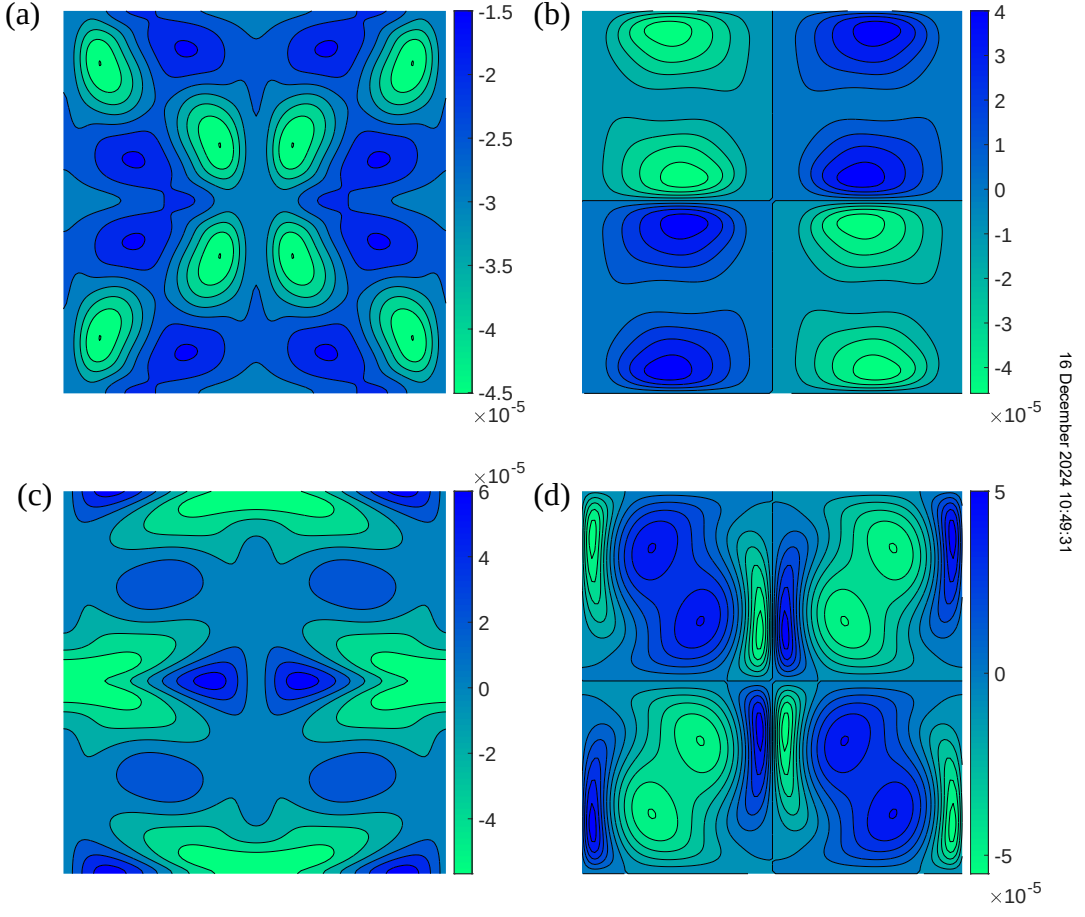
(a)
-1.5
-2
-2.5
-3
-3.5
-4
-4.5
×10-5
(b)
4
3
2
1
0
-1
-2
-3
-4
×10-5
(c)
×10-5
6
4
2
0
-2
-4
(d)
5
0
-5
×10-5
16 December 2024 10:49:31

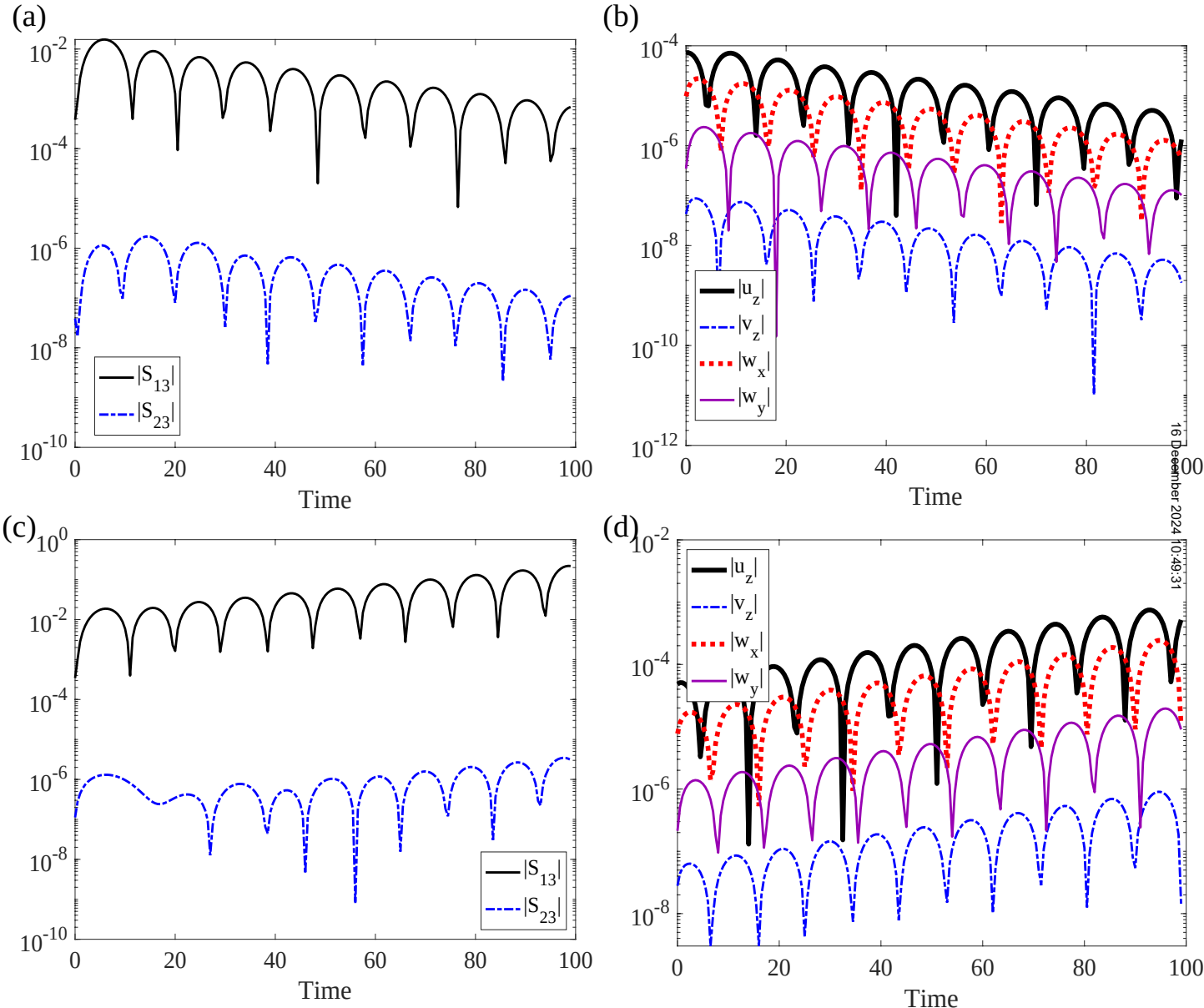
(a)
10^{-2}
10^{-4}
10^{-6}
10^{-8}
10^{-10}
$|S_{13}|$
$|S_{23}|$
0
20
40
60
80
100
Time
(b)
10^{-4}
10^{-6}
10^{-8}
10^{-10}
10^{-12}
$|u_z|$
$|v_z|$
$|w_x|$
$|w_y|$
0
20
40
60
80
100
Time
16 December 2024 10:49:31
(c)
10^{0}
10^{-2}
10^{-4}
10^{-6}
10^{-8}
10^{-10}
$|S_{13}|$
$|S_{23}|$
0
20
40
60
80
100
Time
(d)
10^{-2}
10^{-4}
10^{-6}
10^{-8}
$|u_z|$
$|v_z|$
$|w_x|$
$|w_y|$
0
20
40
60
80
100
Time

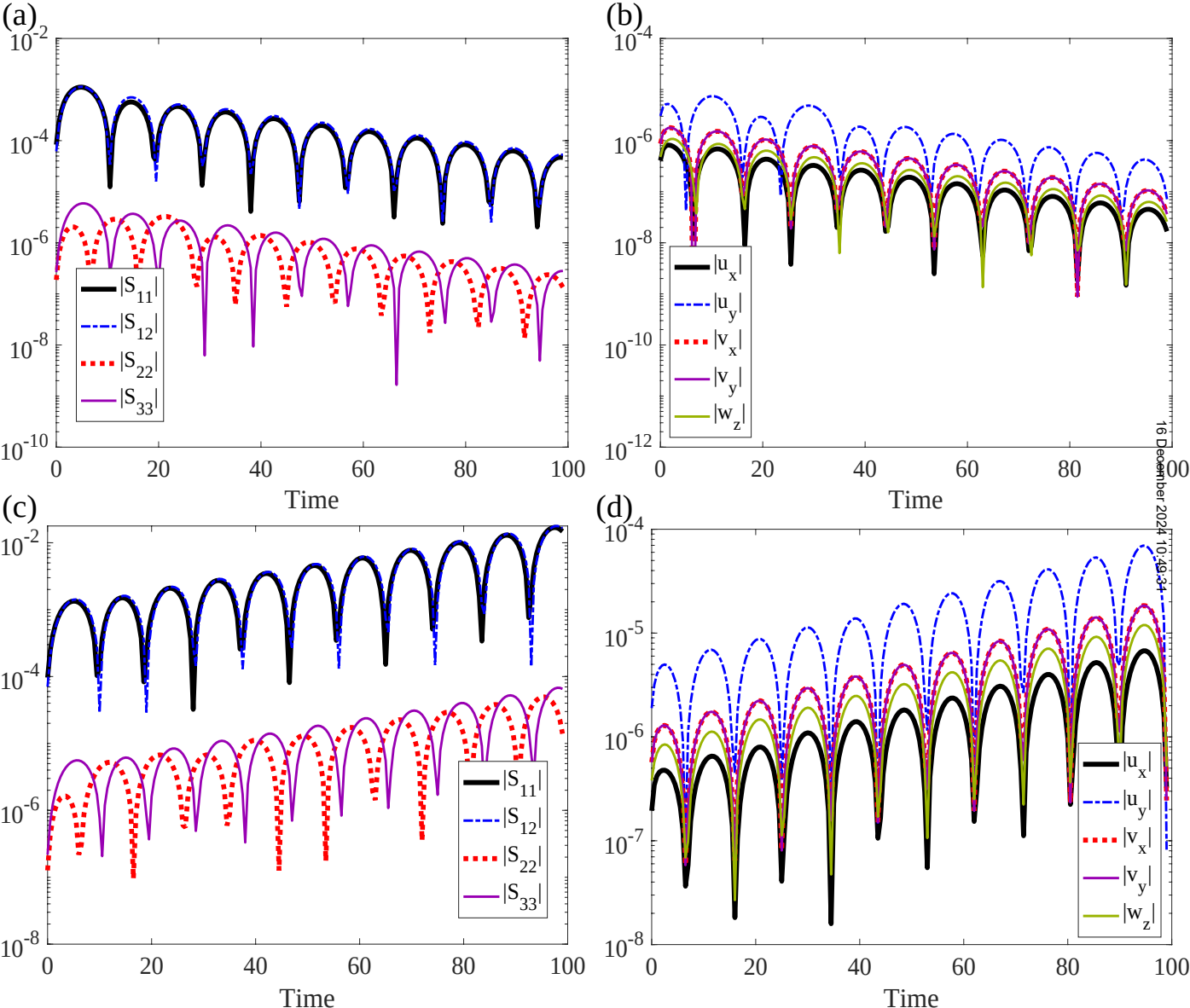
(a)
(b)
(c)
(d)
Time
|S11|
|S12|
|S22|
|S33|
|ux|
|uy|
|vx|
|vy|
|wz|
16 December 2024 10:49:34